

edited by Aleksander Gurlo

Xifan Wang

Photoinduced Thiol-Ene Click Chemistry Assisted Additive Manufacturing and Freeze Casting of Polymer-Derived Ceramics



Xifan Wang

**Photoinduced Thiol-Ene Click Chemistry Assisted
Additive Manufacturing and Freeze Casting of
Polymer-Derived Ceramics**

The scientific series *Advanced Ceramic Materials* is edited by
Prof. Dr. Aleksander Gurlo.

Xifan Wang

**Photoinduced Thiol-Ene Click Chemistry Assisted
Additive Manufacturing and Freeze Casting of
Polymer-Derived Ceramics**

Bibliographic information published by the Deutsche Nationalbibliothek

The Deutsche Nationalbibliothek lists this publication in the Deutsche Nationalbibliografie; detailed bibliographic data are available on the Internet at <http://dnb.dnb.de>.

Universitätsverlag der TU Berlin, 2019

<http://verlag.tu-berlin.de>

Fasanenstr. 88, 10623 Berlin

Tel.: +49 (0)30 314 76131 / Fax: -76133

E-Mail: publikationen@ub.tu-berlin.de

Zugl.: Berlin, Techn. Univ., Diss., 2019

Gutachter: Prof. Dr. Aleksander Gurlo

Gutachter: Prof. Ing. Paolo Colombo

Die Arbeit wurde am 26. Februar 2019 an der Fakultät III unter
Vorsitz von Prof. Dr. John Banhart erfolgreich verteidigt.

The manuscript is protected by copyright.

Cover image: David Karl | Segerkegel | 2017

Print: Pro Business

Layout/Typesetting: Xifan Wang

ISBN 978-3-7983-3088-7 (print)

ISBN 978-3-7983-3089-4 (online)

ISSN 2569-8303 (print)

ISSN 2569-8338 (online)

Published online on the institutional repository of the
Technische Universität Berlin:

DOI 10.14279/depositonce-8462

<http://dx.doi.org/10.14279/depositonce-8462>

Acknowledgements

This thesis is based on the research performed at the Fachgebiet Keramische Werkstoffe of the Faculty III, Werkstoffwissenschaften und -technologien, of the Technische Universität Berlin.

At first, I would like to express my profound gratitude to my PhD advisor Prof. Dr. Aleksander Gurlo, for his supervision, guidance throughout the work and kind offer to host my research at the TU Berlin. I was given much freedom to work independently and supported by him to develop new ideas no matter the feasibility. He is indeed a great mentor and I learned many aspects from him about how to become a scientist. I would also like to thank him for reading and improving the drafts, which are significantly improved based on his suggestions.

My sincere thanks also go to my supervisor Dr. Franziska Schmidt. I am very grateful for her guidance and help in the conception, development and finishing of this thesis. She has supported me from the initial to the final stages of this work.

Collective and individual acknowledgments are also owed to my colleagues at the Fachgebiet Keramische Werkstoffe group. Many thanks to Dr. Oliver Görke, Dr. Maged Bekheet, Dr. Dorian Hanaor, Dr. Ulla Simon, Amanmyrat Abdullayev, Hiba Bensalah, Mathias Czasny, Wuqi Guo, Laura Marie Henning, Onur Kaba, David Karl, Franz Kamutzki, Delf Kober, Lukas Schlicker, Albert Gili de Villasante, Jun Wang, Gaofeng Shao, Clemens Motzkus and everyone who helped me without hesitation. Without their valuable inputs, suggestions and insightful discussions, accomplishing this thesis would have been impossible. Special thanks to Anthony Wang for the comprehensive review over the style and grammar of this thesis. Special thanks also to the technicians Harald Link, Heinz Sap for conducting the FTIR, TG-MS, HF etching experiments, and to Kai-Jens Weisser, Peter Schnepfmüller for their unending assistance and technical wizardry.

In addition, there were many people outside of the Keramische Werkstoffe group who supported my work. I would like to express my sincerest gratitude to:

Dr.-Ing. Paul H. Kamm (Fachgebiet Struktur und Eigenschaften von Materialien, TU Berlin) for performing the radiography, tomography investigations and for the fruitful discussion regarding the in-situ experiments.

Dr. Jörg Bauer (Fraunhofer-Institut für Zuverlässigkeit und Mikrointegration, Berlin) for helping with Differential Scanning Calorimetry under UV exposure experiments and for insightful discussion in regards to the fundamentals of photopolymerization.

Dipl. Ing. (FH) Jörg Nissen for conducting the Field Emission-Electron Probe Microanalysis.

Dipl. Ing. (FH) Sören Selve for conducting the Transmission Electron Microscopy and Energy-Dispersive X-ray spectroscopy.

Shuang Li for the X-ray photoelectron spectroscopy investigations.

Christina Eichenauer for conducting the nitrogen physisorption measurements and Xiaojia Zhao for helping with the data evaluation.

Anke Märten for performing the nanoindentation experiments.

Furthermore, I want to thank my friends in Germany and my family in China, for their support and encouragements. Deepest gratitude to my mom, for her enormous love, support and faith in me, without whom I would not have become the person I am. And last but not least, this thesis is for my father, who teaches me to become an honest and upright man. I hope he will be proud in heaven.

Abstract

Polymer-derived ceramics possess great advantages in the view of cellular ceramic processing compared to traditional powder-based technologies, as the polymeric nature of ceramic precursors allows the utilization of various shaping approaches. Among them, additive manufacturing and freeze casting are two novel shaping methods, which are capable of producing three-dimensional complex architectures and foams with well-controlled pore morphology, respectively.

In this thesis, the energetic and kinetic aspects of the photoinduced thiol-ene polymerization of vinyl containing preceramic polymers with thiol monomers is systematically investigated. Subsequently, a novel stereolithographic approach is developed and applied to the additive manufacturing of complex-shaped polymer-derived ceramics. In addition, photopolymerization-assisted freeze casting is successfully developed to freeze cast liquid preceramic polymer and yields porous ceramics with well-controlled pore morphology.

By utilizing the photoinduced thiol-ene polymerization, the developed stereolithographic approach is applied for the additive manufacturing of three classes of preceramic polymers, i.e. polycarbosiloxanes, polycarbosilane and polycarbosilazane. In the subsequent polymer-to-ceramic transformation, the additively-manufactured cellular polycarbosiloxane SPR212 and polycarbosilazane Durazane 1800 are successfully converted to SiOC and SiCN ceramics without major cracks, while the polycarbosilane SMP10 exploded into small pieces under the same pyrolyzing conditions. The additively-manufactured polysiloxane-derived SiOC components are nearly fully dense, achieving 97 % of the theoretical density and demonstrating excellent compressive strength, surpassing the performance of comparable porous ceramics and stretching the boundaries of material property space in terms of strength-to-weight ratio under compression.

The freeze casting technique assisted with cryo thiol-ene photopolymerization is successfully developed for the production of macroporous PDCs, demonstrating that the free radical-initiated thiol-ene click reaction effectively cross-link the vinyl-containing liquid preceramic polymers into infusible thermosets even at low temperatures. The key factor of this approach relies on the complete photopolymerization of whole frozen samples. Therefore, a freezing liquid, preceramic polymers and fillers (e.g., SiO₂) with weak absorption for UV light is preferred to allow high penetration depth, thus leading to the production of filled, solid samples. By utilizing GO suspension as the freezing liquid and applying the same procedure, ceramic shells of open cylindrical (tubular) shape with an axial void were obtained. The post-pyrolysis treatment of produced SiOC monoliths with HF acid yield materials with hierarchical porosities, i.e. SiOC/SiO₂ nanocomposites after etching demonstrate the highest specific surface area of 494 m²/g and pore sizes across the macro-, meso- and micropores ranges.

Kurzfassung

Polymerabgeleitete Keramiken besitzen große Vorteile im Hinblick auf den Verarbeitungsprozess von zellularen Keramiken im Vergleich zu traditionellen pulverbasierten Technologien, da der polymere Ursprung der Ausgangsstoffe für die Keramik die Nutzung verschiedener Formgebungsmethoden ermöglicht. Additive Fertigung und Gefriergießen sind zwei neuartige Formgebungsverfahren, die jeweils in der Lage sind, komplexe dreidimensionale Geometrien sowie Schäume mit einer kontrollierten Porenmorphologie zu produzieren.

In dieser Arbeit wird die photoinduzierte Thiol-En-Polymerisation von prekeramischen Polymeren, die Vinyl und Thiol-Monomere enthalten, systematisch und sowohl aus energetischer als auch aus kinetischer Hinsicht untersucht. Im Folgenden wird ein neuartiger stereolithografischer Ansatz entwickelt und auf die additive Fertigung von polymerabgeleiteten Keramiken komplexer Gestalt angewendet. Zusätzlich wird photopolymerisierungsunterstütztes Gefriergießen erfolgreich entwickelt, um flüssige prekeramische Polymere gefrierzugießen und poröse Keramiken mit einer definierten Porenmorphologie zu erzeugen.

Mit der Nutzung von Thiol-En-Photopolymerisation wird der entwickelte stereolithografische Ansatz auf die additive Fertigung von drei Klassen prekeramischer Polymere angewendet, darunter Polycarbosiloxane, Polycarbosilane und Polycarbosilazane. In der folgenden Polymer-Keramik-Umwandlung wird das additive gefertigte zellulare Polycarbosiloxane SPR212 sowie das Polycarbosilazane Durazane 1800 erfolgreich in SiOC- und SiCN-Keramiken ohne große Risse umgewandelt, während das Polycarbosilan SMP10 aufgrund des hohen Grades an hydrierten Gruppen unter den gleichen Pyrolysebedingungen in kleine Stücke zersprang. Die additive gefertigten polysiloxan-abgeleiteten SiOC-Teile sind fast komplett dicht und erreichen 97 % der theoretischen Dichte. Sie weisen eine exzellente Druckfestigkeit auf, übertreffen die

Leistung vergleichbarer poröser Keramiken und erweitern die Grenzen der Materialeigenschaften in Hinblick auf das Verhältnis von Festigkeit zu Gewicht unter Druckbelastung.

Die durch kryogene Thiol-En-Photopolymerisation unterstützte Gefrierusstechnik wird erfolgreich entwickelt, um makroporöse PDCs zu produzieren. Dadurch wird gezeigt, dass auch bei niedrigen Temperaturen die Vinyl enthaltenden prekeramischen Polymere während der durch freie Radikale initiierten Thiol-En-Klickreaktion zu unschmelzbaren Duromeren vernetzt werden. Der wesentliche Bestandteil dieses Ansatzes liegt in der vollständigen Photopolymerisation der gesamten gefrorenen Proben. Daher werden eine Gefrierflüssigkeit, prekeramische Polymere und Füllstoffe (z. B. SiO_2) mit schwacher UV-Absorption bevorzugt, um eine hohe Eindringtiefe zu erlauben, sodass ausgefüllte, feste Proben entstehen. Mit der Nutzung von GO-Suspension als Gefrierflüssigkeit werden im gleichen Verfahren einzelne keramische Schalen mit hohlzylindrischer (rohrförmiger) Gestalt und axialem Loch erzeugt. Durch eine an die Pyrolyse anschließende Behandlung der produzierten SiOC-Monolithen mit HF-Säure ergeben sich hierarchische Porositäten. SiOC/ SiO_2 -Nanokomposite zeigen nach dem Ätzen die höchste spezifische Oberfläche mit $494 \text{ m}^2/\text{g}$ und Porengrößen im Bereich von Makro-, Meso- und Mikroporen.

Table of contents

Acknowledgements	v
Abstract	vii
Kurzfassung.....	ix
Motivation, Goals and Content.....	xv
1 Literature survey.....	1
1.1 Polymer derived ceramics (PDCs).....	1
1.1.1 Preceramic polymers and their cross-linking behavior.....	2
1.1.2 Photopolymerization of preceramic polymers	5
1.2 Additive manufacturing of ceramic materials.....	8
1.2.1 Introduction to additive manufacturing.....	8
1.2.2 Materials choice for additive manufacturing..	13
1.2.3 Additive manufacturing of ceramics.....	14
1.2.4 Ceramic stereolithography.....	19
1.2.5 Stereolithography of PDCs	25
1.3 Freeze casting of porous ceramics.....	28
1.3.1 Processing principles	29
1.3.2 Pore morphologies	32
1.3.3 Freeze casting of PDCs	33
2 Materials and Methods.....	39
2.1 Synthesis, fabrication and processing of materials.	39
2.1.1 Materials used in this work.....	39
2.1.2 Synthesis of graphene oxide.....	41
2.1.3 Preparation of preceramic polymer resins	42
2.1.4 Fabrication of thermosets	43

2.1.5	Thermal transformation from thermosets to ceramics	43
2.2	Characterization methods	47
2.2.1	Radiography and Tomography	47
2.2.2	Scanning Electron Microscopy (SEM) and Energy-Dispersive X-ray Spectroscopy (EDX)	47
2.2.3	Field Emission-Electron Probe Microanalysis (FE-EMPA)	48
2.2.4	Transmission Electron Microscopy (TEM) and Energy-Dispersive X-ray Spectroscopy (EDX) ...	48
2.2.5	Nuclear Magnetic Resonance (NMR) Spectroscopy	49
2.2.6	Rheology characterization	49
2.2.7	X-Ray Diffraction (XRD)	49
2.2.8	X-Ray Photoelectron Spectroscopy (XPS)	49
2.2.9	Fourier Transform Infrared (FTIR) Spectroscopy	50
2.2.10	Ultraviolet–Visible (UV-Vis) spectroscopy	50
2.2.11	Nitrogen physisorption	50
2.2.12	Simultaneous Thermal Analysis coupled with Mass Spectrometry (STA- MS)	51
2.2.13	Differential Scanning Calorimetry (DSC) under UV exposure	51
2.2.14	Nanoindentation	51
2.2.15	Compressive Strength measurements	52
3	Thiol-ene click chemistry with Si-containing preceramic polymers	53
3.1	Photocuring experiments	53
3.2	Photoinitiated cross-linking of preceramic polymers	55

3.3	Energetics and kinetics of thiol-ene click chemistry.....	62
3.4	Summary.....	69
4	Thiol-ene click chemistry assisted additive manufacturing	71
4.1	Overall approach.....	71
4.2	Process design.....	75
4.2.1	Selection of manufacturing equipment	75
4.2.2	Resin tank design	76
4.3	Resin formulations	80
4.3.1	Selection of preceramic polymers	80
4.3.2	Selection of thiols	82
4.3.3	Selection of photoinitiators.....	83
4.3.4	Curing depth measurements and selection of photoabsorbers.....	86
4.4	Additive manufacturing of preceramic polymers and their conversion to ceramics	92
4.4.1	Printing parameters	92
4.4.2	Fabricated thermosets.....	93
4.4.3	Thermal transformation of thermosets into ceramics	95
4.4.4	Mechanical properties of SiOC 2D honeycombs.....	103
4.5	Summary.....	110
5	Cryo thiol-ene click chemistry assisted freeze casting of preceramic polymers.....	113
5.1	Process design.....	113
5.1.1	Overall approach.....	113
5.1.2	Materials selection.....	114
5.1.3	Unidirectional freeze casting set up.....	116

5.2	SiOC/GO shells.....	117
5.2.1	Synthesis of samples.....	117
5.2.2	Composition and structure.....	122
5.2.3	Mechanism of axial hole formation in SiOC/GO shells	128
5.2.4	Summary	134
5.3	SiOC and SiOC/SiO ₂ foams with multiscale hierarchical porosity.....	136
5.3.1	Synthesis of samples.....	136
5.3.2	Pore morphology	140
5.3.3	Multiscale porosity in HF-etched foams.....	146
5.3.4	Summary	151
6	Conclusions and outlook.....	155
7	References	163
	Symbols and abbreviations.....	182
	List of figures.....	184
	List of tables	193

Motivation, Goals and Content

Ceramics are one of the most ancient materials that humans have used, dating back thousands of years: from the mysterious prehistoric figurines, to potteries used for food containers or arts, and clay-based ceramics for tiles and bricks. Around the mid-19th century, the first porcelain-based electric insulator was introduced, thus opening the era of technical ceramics. Since then, advanced technical ceramics have developed drastically and contribute to many technological fields, including electronics, optics, medical, energy, automobile and aerospace. These developments are attributed to ceramics materials' unique and exceptional electrical, thermal, mechanical and chemical resistant properties. The traditional method to prepare ceramics is powder-based, where inorganic particles are pressed or joined and later sintered to become dense.

Polymer-derived ceramics (PDCs) define a class of ceramic materials which are obtained through the pyrolysis of the so-called preceramic polymers (PCP) under inert atmosphere. During the pyrolysis process, organic species (mainly H_2 and CH_4) evolve out from the preceramic polymers and leave an inorganic glassy ceramic behind. The polymer precursors provide the ceramics with tailored compositions and microstructures through their molecular design. These polymer-derived ceramics have been proved to possess exceptional properties, such as stability towards oxidation and corrosion, crystallization and creep resistance. Compared with traditional ceramic powder processing, PDCs can be obtained at relative low sintering temperature (around $1100\text{ }^\circ\text{C}$) without additives, which provides a significant cost saving advantage. In addition, because the majority of preceramic polymers are either in liquid state at room temperature, or in solid state but possess low glass transition temperature, and can be dissolved in organic solvents, PDCs allow the utilization of processing routes that are applicable for polymers, including infiltration, injection molding and extrusion-based technologies. The use of preceramic polymers thus facilitates

the production of ceramic fibers, coatings, composites and cellular scaffolds, which are challenging to obtain through powder-based technologies.

PDCs route represents a great advantage compared to powder-based technologies in the view of cellular ceramic processing, especially in the newly-developed processing approaches, which are additive manufacturing (AM) and freeze casting techniques.

Comparing to polymers or metals, the additive manufacturing of ceramics is not easy, as the melting or sintering temperature of ceramic materials is significantly higher. Accordingly, AM of ceramics through selective laser melting/sintering or through fused deposition modelling is very challenging. Other techniques like powder bed 3D printing will yield ceramic components with a high amount of residual porosity, and direct ink writing or robocasting are not capable of producing dense monolithic structures. Nonetheless, the AM of ceramics is believed to have a great impact on the production of ceramic components and will open up new industrial areas and markets for ceramic materials. Among the AM technologies for ceramics, stereolithography (SLA), based on the layer-wised photopolymerization of liquid photopolymer filled with ceramic particles, is capable of providing porous or monolithic ceramic components with high relative density, highest resolution and optimal surface quality. Nonetheless, the dispersion of ceramic particles into liquid resin has brought up several significant challenges, including increased viscosity, reduced curing depth, degraded resolution and particle aggregation. In contrast, AM of ceramic materials through stereolithography of preceramic polymer does not have these challenges, due to the absence of ceramic particles. It allows the fabrication of ceramic three dimensional (3D) geometries with comparable resolution limit to polymer 3D printing, which is difficult to achieve via traditional powder-based technologies. Until now, the stereolithography of preceramic polymers is hampered by the absence of simple but effective photo-induced cross-linking mechanism, which is versatile and applicable with various PCPs.

The shaping of PCPs, namely the definition of their spatial geometry, shall be combined with cross-linking process to yield infusible thermosets. Otherwise, the fabricated geometry can easily collapse or deform during the subsequent thermal treatment step. Currently, stereolithography of PDCs is restricted by the limited choice of readily photocurable preceramic polymers, and thus the obtainable ceramic compositions are mostly limited to SiOC. Meanwhile, the freeze casting of PDCs is underdeveloped as well, due to limitations associated with insufficient mechanical stability of fabricated parts. This is despite the fact that they represent a convenient method to produce large dimension bulk polymer derived ceramics with fully dense cell walls.

Pores are generally considered as detrimental for technical ceramics, as they act as stress concentrators and can facilitate the crack propagation, which leads to mechanical failures. Nonetheless, porous ceramics are drawing considerably more attention, since they can be engineered to combine the inherent properties of ceramics with the merits provided by pores, namely light weight, high specific strength, improved materials and thermal transfer capability. Freeze casting is a promising approach to fabricate macroporous ceramics, as it allows the precise control over pore shape, pore size and overall pore morphology. Considerable amounts of work have been carried out in freeze casting colloidal suspensions of ceramic particles. However, the preparation of ceramic suspensions is generally complex and time-consuming, and in addition particle engulfment and sedimentation have to be considered as well. In contrast, the freeze casting of polymer solution, which is a homogeneous one phase system, has been rarely studied, especially for preceramic polymers. Despite the ease of preparing preceramic polymer solutions and the great potential that could be offered by macroporous PDCs in harsh environments, the challenge of freeze casting PDCs lies on the difficulty to retain the polymer's shapes after the drying process. This is a challenge due to the fact that the majority of preceramic polymers are in liquid state at room temperature, and

their cross-linking mechanism involves heat treatment, which fundamentally contradicts the freeze casting concept.

To address these research problems, or in other words, to expand the utilization of PDCs in stereolithography-based additive manufacturing and freeze casting routes, the key point relies on finding a simple, efficient and universal cross linking mechanism for different preceramic polymers under various conditions (temperature, solvent). Out of all the polymerization reaction mechanisms for preceramic polymers, thiol-ene click reaction seems to be the most suitable one, due to its simplicity, high reaction rate and versatility. Additionally, there are a very limited number of studies available for the study of producing PDCs assisted with thiol-ene polymerization.

The first goal of this thesis is therefore the examination of the versatility of thiol-ene click reactions with different classes of preceramic polymers under different conditions.

The second goal is then the utilization of photoinduced thiol-ene click chemistry with preceramic polymers in stereolithography-based additive manufacturing for fabrication of three-dimensional cellular PDCs of high complexity.

The third goal is the developing of freeze casting technique combined with cryo photopolymerization with thiol-ene click chemistry for the fabrication of PDCs with controlled pore morphology as well as multiscale hierarchical porosity.

The thesis is organized as follows:

Chapter 1 gives a short introduction to polymer derived ceramics, describing the different cross-linking mechanism of preceramic polymers, including photopolymerization. In addition, it reviews the stereolithography based additive manufacturing and freeze casting of PDCs, explaining the latest developments and potential restrictions, thus leading to the research problems and goals of this work.

Chapter 2 describes the materials applied in this work, gives an overview over samples produced as well as about characterization techniques used in this work. The details of experimental procedures for stereolithography based additive manufacturing and freeze casting of PDCs are given in the Chapters 4 and 5, respectively.

Chapter 3 extensively studies the applicability of photoinduced thiol-ene click reaction for cross-linking of different classes of preceramic Si-containing polymers. The latter include polysiloxanes SILRES® H62 C and Polyramic® SPR-212, polycarbosilazane Durazane® 1800 with side vinyl groups and polycarbosilane StarPCSTM SMP-10 with side allyl groups.

Chapter 4 covers the stereolithography of aforementioned preceramic polymers assisted with thiol-ene click chemistry photopolymerization and the subsequent thermal transformation of fabricated thermosets into ceramics. The resin formulations and resin tank are designed and optimized for the manufacturing process with preceramic polymers, thus allowing the high resolution fabrication of PCP-based thermosets with various geometry, from cellular lattices to bulk structures. The resultant printed parts are pyrolyzed with low ramping rates to allow the escaping of evolved gas species, thus leading to the formation of ceramic components with high relative density, smooth surface and excellent mechanical properties.

Chapter 5 represents the new approach based on combining conventional freeze casting with cryo-photopolymerization of polysiloxanes for the production of porous SiOC ceramics. The photopolymerization of frozen preceramic polymers is the key to this approach, and by controlling the spatial photopolymerization degree via altering the penetration of incident UV light, ceramic structures from complete cylinder to unique shell with axial hollow presented in the middle can be obtained. The developed approach is applied with solution- and suspension-based freeze casting. Adding silica nanopowder improved the mechanical integrity of polymer scaffolds

by reducing the shrinkage after vacuum drying, and gives an extra degree of pore formation through the latter pyrolysis HF treatment.

Chapter 6 summarizes the main findings of this work and provides guidelines and suggestions for further investigations.

1 Literature survey

1.1 Polymer derived ceramics (PDCs)

Polymer-derived ceramics were first synthesized in 1960 by direct thermolysis of organosilicon, which was utilized as ceramic precursor ¹. Compared to traditional powder technology, PDCs define a class of ceramic materials that are prepared, without any additives, by the thermal pyrolysis of appropriate preceramic polymers in inert or reactive atmosphere. PDCs generally exhibit exceptional thermal-mechanical properties, like stability against creep, oxidation, crystallization and phase separation up to 1500 °C ². For example, Riedel et al. ³ reported remarkable thermal stability of polymer derived Si-B-C-N ceramics that are able to withstand decomposition and creep even up to 2200 °C in argon atmosphere.

The PDCs are synthesized through the thermal decomposition of preceramic polymers, which is in contrast to the conventional solid or liquid ceramic powder sintering techniques, as their chemical compositions are directly dependent on the molecular design of the utilized preceramic polymers. The most known classes of PDCs are based on binary systems such as, Si₃N₄, SiO₂, SiC, BN, AlN, ternary systems such as SiCN, SiOC and quaternary systems such as SiOCN and SiBCN ^{1, 4, 5}. In recent years, pentanary systems of PDCs have been reported as well ⁶. The tailorable ability of the chemical composition of preceramic polymers also allows the incorporation of other elements into the PDCs systems, so that corresponding PDCs nanocomposites can be obtained. For example, metals of the 4th group - Ti, Zr, and Hf - have been chemically attached to the preceramic polymer network to become a single source precursor, which after pyrolysis led to the formation of nano-sized domains of M/MO_x/MSi_x embedded inside the glassy ceramic (SiCO, SiCN) matrix ^{5, 7-9}. In addition, PDCs nanocomposites enhanced with metals from groups 8-11 can be obtained through thermolysis of corresponding preceramic polymers reacted with suitable

1.1 *Polymer derived ceramics*

metallopolymers (e.g. ferrocene) or coordination compounds (e.g. Ni and Cu complex) ^{10–13}.

Conventional ceramic powder techniques require the presence of sinter additives and the utilization of molds or pressing devices to confine the fabricated geometry. As the synthesis of PDCs start with the shaping of the preceramic polymer, it facilitates the fabrication of fibers ¹⁴, coatings and membranes ^{15–17} and composites material ^{5, 10}. Since the polymeric ceramic precursors are either in a liquid state or they are dissolvable in various solvent. This allows the application of various polymer-forming techniques to process preceramic polymers. For example, polymer infiltration pyrolysis ¹⁸, injection molding ¹⁹, coating from solvent ¹⁵ and extrusion ²⁰ are possible. Once formed, fabricated objects from preceramic polymers can be directly converted to ceramics via pyrolysis.

Recently, extensive studies have been focused on applying preceramic polymers with novel processing routes including freeze casting (also known as ice templating) and 3D printing. PDCs are shown to possess great potentials in these fields. These topics will be discussed in detail in the following sections.

1.1.1 Preceramic polymers and their cross-linking behavior

The type of preceramic polymers and their molecular structures have a great influence not only on the composition but also the phase distribution and microstructure of the final ceramic materials. Thus, the chemical and physical properties of PDCs can be specifically adjusted to a great extent by choosing the appropriate precursors. The molecular structures of different organosilicon preceramic polymers are illustrated in Figure 1. There are two important parameters determining the structure and properties of preceramic polymers, first, the group X linking with Si atom repeatedly called as the backbone, and second, the organic groups (R_1 , R_2) attached to Si called as the side groups. The elements X linked to

Si on the backbone determine the class of preceramic polymer. In polysiloxanes for example, the Si is linked with O, in polycarbosilanes with CH_2 , in polysilazanes with NH and in polysilylcarbodiimides with $\text{N}=\text{C}=\text{N}$. The side groups mostly represent functionalities. Changing them allows fine-tuning of the solubility, rheological behavior, thermal stability and cross-linking mechanism of the selected preceramic polymers.

For preceramic polymers to be effective in the thermal decomposition process, e.g. to achieve a high ceramic yield, the preceramic polymer is required to possess a sufficiently high molecular weight in order to avoid the evaporation of oligomers (low molecular species) especially in the early stage of pyrolysis. Nonetheless, the molecular weight of generally used preceramic polymers is relatively low and they do not possess sufficient cross-linking degree, which results in a low glass transition temperature. Consequently, most preceramic polymers are in liquid state at room temperature, which is beneficial for the fabrication of coatings and fibers.

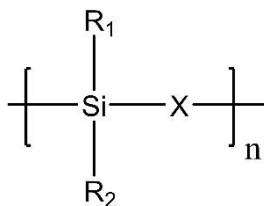


Figure 1. Simplified representation of organosilicon compounds as precursors for Si based ceramics.

The cross-linking process of preceramic polymers is a decisive step for the latter pyrolysis. By incorporating certain functional groups (e.g. Si-alkoxide, Si-OH, Si-H, Si-C=C), preceramic polymers can be cross-linked via condensation, addition reactions etc., which generally occurs around 200 °C. The addition of catalysts can lower the cross-linking temperature and enhance the curing efficiency, while some cross-linking reactions can be initiated by UV illumination with the presence of photoinitiators. Through cross-linking, preceramic

1.1 Polymer derived ceramics

polymers convert to infusible organic/inorganic polymers with sufficiently high molecular weight, which prevents massive oligomer volatilization and fragmentation. Additionally, infusibility means that the polymer will not experience melting or softening and the preceramic polymer is able to retain its shape during pyrolysis. Therefore, shaping of preceramic polymers is conducted regularly with or after the cross-linking step.

Polycarbosilanes can be cross-linked through oxidation curing^{21, 22} and electron-beam (e-beam) curing^{23, 24}. Oxidation curing of polycarbosilanes involves the cross-linking of Si-H and Si-CH₃ groups with oxygen to form Si-OH, Si-O-Si and C=O units in a radical mediated way. It leads to the presence of significant oxygen content in SiC based materials after pyrolysis. While silicon carbide with low oxygen content can be obtained via means of electron irradiation in oxygen free environment.

The cross-linking of polysiloxanes can be achieved via condensation, transition metal catalyzed addition and free radical initiated polymerization^{1, 25}. For polysiloxanes containing hydroxyl (-OH) and alkoxy groups (-OCH₃), a condensation reaction can occur between hydroxyl groups, which are partially formed through the hydrolysis of present alkoxy groups. The condensation reaction further leads to the formation of Si-O-Si bonding. In the case of polysiloxane with methyl or vinyl functionalities, the cross-linking reaction can be conducted thermally by reacting with peroxide.

The cross-linking mechanism of polysilazanes involves four major reactions, dehydrocoupling, transamination, vinyl polymerization and hydrosilylation²⁶. Dehydrocoupling involves the reaction of Si-H and N-H accompanied by the release of hydrogen gas, while vinyl polymerization (addition of carbon double bonds) occurs at higher temperatures without mass loss. Transamination comprises of rearrangements between Si and N atoms with an evolution of amines and ammonia. This process leads to a direct decrease in the nitrogen content in the final ceramic materials after pyrolysis.

Among the cross linking reactions, hydrosilylation is a versatile cross-linking reaction that occurs in all classes of preceramic polymers, which contains Si-H and Si-unsaturated carbon groups. It describes a simple addition of Si-H across the C-C unsaturated bonds as depicted in Figure 2. Advantages of this reaction include no gases are emitted as by-product compared to condensation and dehydrocoupling. Additionally, it can be conducted at room temperature by using platinum based catalysts or at higher temperatures (around 200 °C) or initiated with light illumination when mixed with photoinitiators ²⁷. Therefore, it represents one of the most important methods to prepare organosilicon compounds.

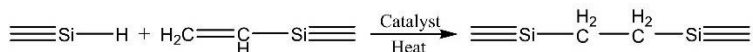


Figure 2. Hydrosilylation reaction between Si-H and Si-vinyl groups.

1.1.2 Photopolymerization of preceramic polymers

When mixing preceramic polymers with significant amounts of photoinitiators (PI), hydrosilylation and vinyl addition as described previously can be initiated by photoillumination, which excites the photoinitiators thus generating free radicals that attack the Si-H and Si-vinyl groups. With that liquid preceramic polymers transform under photoillumination into an infusible thermoset, which can retain its shape after thermal treatments. Due to this characteristic, there have been several studies in the past focusing on fabricating PDCs based micro-electro-mechanical systems (MEMS) ^{28–35} by shaping preceramic polymers (polysiloxane RD-684 and polysilazane Ceraset, ABSE) with photolithography followed with pyrolyzing in inert atmosphere. Nonetheless photoinitiated hydrosilylation and vinyl polymerization represent certain unappealing properties such as slow reaction rate, low conversion rate, low photo-curing depth and the requirement for high energy density illumination. Even with large amounts of photoinitiator, the photopolymerization rate of vinyl

1.1 Polymer derived ceramics

containing preceramic polymers is still low when compared to classic photopolymerization, e.g. those of acrylates and methacrylate ³⁶.

Thiol-ene polymerization ^{37, 38}, also called as thiol-ene click reactions, are polymerization reactions between multifunctional thiols and vinyl containing monomers that occurs in a step-growth manner. The reaction is initiated through the generation of free radical centers, which are most commonly created by illuminating the photoinitiators. Its reaction mechanism, first proposed by Kharasch et. al ³⁹ in 1938, involves three general steps: initiation, propagation and termination.

In the initiation step, the photoinitiator (e.g. benzophenone) is excited by the absorption of a photon and cleaved to form free radicals, whereupon they can easily abstract hydrogen from thiol compounds due to the weak S-H bonding. This creates a highly reactive thiyl radical (RS•) attacking the unstructured carbon double bonds (RCH=CH₂) and generating carbon-centered radicals (RC•-CH₂-SR), which could further abstract hydrogen atoms from the thiol monomers (RSH). This reaction mechanism is considered both radical, where a single thiyl radical can cause a waterfall chemical attack, and step-growth like since the propagation requires the transfer of free radicals between the thiyl and the carbon center. Any radical recombination (thiyl-thiyl, thiyl-carbon or carbon-carbon) will lead to the termination of the reaction, which is the fundamental difference in relation to acrylates and methacrylates. The simplicity, robustness, multi-step reaction mechanism has made light-mediated thiol-ene click reactions an ideal solution to produce homogenous polymer networks with low volume shrinkage and low stress development as well as being insensitive to oxygen.

The low polymerization rate of vinyl containing preceramic polymers can be overcome by the addition of multifunctional thiol monomers, thereby changing the reaction mechanism to the step-growth wise thiol-ene click reaction. Bowman et. al ³⁶ reported the fabrication of SiCN MEMS through the thermal pyrolysis of thiol-ene polymerized polysilazanes (Ceraset and VL20). The photopolymerization rate of vinyl containing polysilazane was increased by several orders of magnitude with the utilization of multifunctional

thiol monomers. Ultra-low concentrations (0.2 wt%) of 2,2-dimethoxy-2-phenyl acetophenone (DMPA) as photoinitiator were sufficient to trigger the reaction, which facilitated the fabrication of high aspect ratio structures. Because the penetration depth of incident photons is inversely proportional to the photoinitiator concentration. The warping of the produced photopolymer caused by internal stress was avoided as well due to the homogeneous polymer network. Alves and Nischang ⁴⁰ prepared organic-inorganic monolithic materials employing vinyl polyhedral oligomeric silsesquioxanes (POSS) with multi-thiols by thiol-ene click polymerization. By conducting the polymerization in a porogenic solvent system, macroporous properties can be obtained. The monolith also demonstrated different morphology in relation to the condition whether the thiol-ene reaction was initiated by heat or X-ray illumination. However, they did not study the hybrid polymer to ceramic transformation through further pyrolysis. As we can see, producing polymer-derived ceramics with thiol-ene click reaction remains underdeveloped despite its great potential in the photopolymerization field.

1.2 Additive manufacturing of ceramic materials

1.2.1 Introduction to additive manufacturing

Additive manufacturing is defined as ‘a process of joining materials to make objects from 3D model data, usually layer upon layer, as opposed to subtractive manufacturing methodologies’ according to the American Society of the International Association for Testing and Materials (ASTM F2792-12a) ⁴¹. Ever since its introduction in the mid-1980s, AM has dramatically developed and grown into diverse processes, including stereolithography (SLA), fused deposition modeling (FDM), selective laser sintering (SLS), selective laser melting (SLM), laminated object manufacturing (LOM), inkjet printing, and others. Nonetheless, the general foundation of the various AM technologies is similar. First the three-dimensional model is generated with a computer-aided design (CAD) and sliced into finite numbers of two-dimensional (2D) layers. Then by building these 2D layers one by one, a three-dimensional object can be obtained. Theoretically, any object with complex 3D geometry can be fabricated in this manner.

Additive manufacturing is distinctly different when compared to traditional manufacturing processes, such as machining, casting and forming, as it provides a cost-effective way to build complex shaped parts. The advantages of AM include:

1. The easy realization of customized and personalized designs, where changing the final product geometry only requires the modification of the uploaded CAD file.
2. The material waste is significantly reduced compared to subtractive manufacturing methods like CNC machining.

3. Casting molds as well as shaping/cutting tools are not required during the fabrication process.
4. Most importantly, the AM technology liberates the geometry restriction during fabrication and allows engineers and designers to create novel ideas and structures.

Additive manufacturing has been known for more than 30 years, but has never before been as popular as it is now both for industry and public. The critical point came in 2008 when the last major patent about fused deposition modelling expired ⁴², and FDM printers could be fabricated without violating the intellectual property. Ever since, interest has grown and large investments have been attracted into the field of AM. According to the report by Wohlers⁴³, the global additive manufacturing revenue is expected to grow at a rate of 15.0 % (compound annual growth rate, CAGR, 2015-2025) and is expected to reach more than 21 billion \$ by 2020. The robust growth is mainly due to the expansion in metal 3D printing and AM service providers.

There are multiple technologies developed for additive manufacturing, differences among them lie in the physical or chemical approaches to fabricate each 2D layers. Depending on the working principles of each technology, they are divided into seven basic categories according to the ISO (the International Organization for Standardization) ⁴⁴. Table 1 shows the seven basic categories and their representative technologies.

In the following sections the working principles of different additive manufacturing methods will be briefly described on the basis of refs. ⁴⁴⁻⁴⁶.

Vat Photopolymerization “*is an AM process in which liquid photopolymer in a vat is selectively cured by light-activated polymerization*” ^{44?}.

The basic principle of this process is the photopolymerization of liquid monomers into a highly cross-linked polymer. The photosensitive monomer can be selectively hardened by either a scanning laser (known as stereolithography) or a digital projector which exposes the entire building platform (known as DLP 3D

1.2 Additive manufacturing of ceramic materials

printing). DLP can achieve a higher printing speed compared to stereolithography as each layer is exposed and thereby cross-linked at once. However, the resolution of DLP 3D printing depends on the resolution of projectors. The latter determines how many pixel/voxel are available within certain projection area, thus deciding the size of each pixel. Increasing the projected area will lead to the enlargement of each pixel, thus large structures can only be printed in a coarser resolution. While the resolution of SLA is independent from the printing model size, as it only depends on the laser spot size as well as its energy distribution.

Table 1. AM process categories and representative examples according to the ISO/ASTM 52900 ⁴¹.

Category	Examples
Vat photopolymerization	Stereolithography (SLA), Digital Light Processing (DLP)
Material jetting	Polyjet, XJET
Binder jetting	3D Printing, Metal jet
Powder bed fusion	Selective laser sintering (SLS), selective laser melting (SLM), Electron beam melting (EBM)
Material extrusion	Fused deposition modeling (FDM), Robocasting
Directed energy deposition	Electron beam additive manufacturing (EBAM)
Sheet lamination	Laminated object manufacturing (LOM), ultrasonic additive manufacturing (UAM)

Material jetting (MJ) “*is an additive manufacturing process in which droplets of build material are selectively deposited*”⁴⁹. Here a print head (very similar to the print head used in an inkjet printer) is used to dispense droplets of photosensitive polymers followed with UV hardening. The solidifying principle (photopolymerization) as well as the feedstock used are very similar to SLA and DLP 3D printing. However, one of the distinct advantages of material jetting is the

possibility of operating multiple print heads in parallel that can dispense different materials. This allows multi-material printing or multi-color printing, which are very challenging to achieve in VAT photopolymerization based techniques. Examples of material jetting are the PolyJet Technology owned by 3D Systems and direct inkjet printing (DIP).

Binder jetting “*is an additive manufacturing process in which a liquid bonding agent is selectively deposited to join powder materials* ⁴⁴”. In deviation to MJ, the feedstock used in binder jetting is powder, which can be polymer, metal or ceramics. There are different bonding agents available (water, glue, organic solvent) depending on the powder material. Despite the wide choice of feedstock material and low operating cost, parts 3D printed with binder jetting generally suffer from issues like low mechanical properties, high porosity and rough surfaces. Hence, post treatment like sintering of metal/ceramic powders or infiltration with epoxy resin is frequently required.

Powder bed fusion “*is an additive manufacturing process in which thermal energy selectively fuses regions of a powder bed* ⁴⁴”. A laser (most of the cases) or occasionally an electron beam (only in EBM based techniques) is applied to melt, fuse or sinter the particles together. Since polymer and metal have relatively lower melting points than ceramics, they are more suitable for this process than ceramic powders. Since the printed structure is embedded inside the unconsolidated powder bed, supporting structures are not necessary, so structures with extreme complexity can be obtained. Some of the popular techniques belonging to powder bed fusion are selective laser sintering (SLS), selective laser melting and electron beam melting (EBM). Until recently these processes have mostly been utilized in the industry due to the expensive machines and high operation costs (laser, vacuum).

Material extrusion “*is an additive manufacturing process in which material is selectively dispensed through a nozzle or orifice* ⁴⁴”. One of the most common material extrusion techniques is fused deposition modelling (FDM), in which a thermoplastic material is melted and extruded through a heated nozzle and then deposited on a cooler substrate

1.2 Additive manufacturing of ceramic materials

layer by layer. The most common thermoplastic materials used in this process are Polylactic acid (PLA), acrylonitrile butadiene styrene (ABS) and Polyethylene terephthalate (PETG). FDM is by far the most common and inexpensive technique available on the market, as its working principle is simple and the feedstock material is cheap. Additional post treatment is not necessary. Its major disadvantage is that the resolution in Z-axis compared to other AM techniques is rather low (generally 0.25 mm), thus a finishing step is necessary if a smooth printing surface is required.

Directed energy deposition (DED) *“is an additive manufacturing process in which focused thermal energy is used to fuse material by melting as they are being deposited”*⁴⁴. DED is in principle similar to the material extrusion process as a material is melted and deposited onto a substrate where it cools down and solidifies. Both polymer and ceramic materials can be used with this technique, though metals are most frequently applied (in the form of powder or wire) in this process. Therefore, the whole procedure has to be operated in a high-vacuum environment to avoid oxidation. An advantage of this technique is that the deposition of material is done through 4-5 axis machines. Thereby 3D printing on uneven or curved substrates is possible. Hence directed energy deposition is frequently used for repairing or adding new materials to an existing component.

Sheet lamination *“is an additive manufacturing process in which sheets of material are bonded to form an object”*⁴⁴. There are two techniques that are included in the sheet lamination terminology, laminated object manufacturing (LOM) and ultrasonic additive manufacturing (UAM). LOM is one of the earliest additive manufacturing technologies, where 3D objects are built with layers of paper or plastic sheets that are joined together through heat, pressure or adhesives. It is a low cost 3D printing process. Whereas UAM utilizes ultrasonic welding to join sheets of metals to build 3D metal parts. This process however requires further machining steps to cut and remove the unjoined metal parts, hence making it an additive and subtractive combined manufacturing technology.

1.2.2 Materials choice for additive manufacturing

All material classes can be additively manufactured, however each technology has its best fitting material and each materials class fits best one of the existing technologies. Table 2 lists three classes of materials, including polymers, metals, and ceramics and representative technologies that are capable to AM these material classes.

Table 2. Material choice for AM technologies.

Material	AM technologies
Polymers	Stereolithography (SLA)/Digital light processing (DLP), Polyjet, 3D Printing (3DP), Selective laser sintering/melting (SLS/SLM), Fused deposition modelling (FDM), Laminated object manufacturing (LOM), Direct ink writing (DIW)
Metals	3D Printing (3DP), Direct ink jet printing (DIP), Fused deposition modelling (FDM), Selective laser sintering/melting (SLS/SLM), Electron beam melting (EBM), Electron beam additive manufacturing (EBAM), Direct ink writing (DIW)
Ceramics	Stereolithography (SLA)/Digital light processing (DLP), Direct ink jet printing (DIP), 3D Printing (3DP), Selective laser sintering (SLS), Direct ink writing (DIW)

In the past, AM technologies have been mostly developed for the production of polymers and metals. The techniques that are capable of fabricating 3D ceramic components all have limitations and are less developed, due to the challenges of feedstock supplier and the post sintering process. In addition, the common AM technologies including SLA, FDM, SLS and SLM, which are suitable for the production of polymer and metal materials, are difficult to be directly applied with ceramics as well. This is because, the traditional advantages of utilizing ceramic materials including chemical inertness, thermal stability (high melting point) and insulating to electric conduction can become the obstacle to apply ceramics in AM processes. Inorganic ceramic powders cannot be joined through chemical reactions due to their chemical inertness and it is far more

1.2 Additive manufacturing of ceramic materials

challenging to fuse ceramic powders - as compared with polymer and metal - through sintering or melting due to higher melting temperatures. In addition, additive manufacturing of ceramics always requires post processing after the printing process. Similar to traditional ceramic processing techniques, the 3D printed parts coming off the 3D printer (called “greenbody”) are generally mechanically unstable and cannot be utilized directly. Post processing, e.g. debinding (removing of organic additives), sintering (fusing of the ceramic powders) and glazing (surface finishing, not always required), is essential to bring back ceramic’s exceptional mechanical properties, which are related to the composition and microstructure of the ceramics. Existing ceramic AM technologies only complete the shaping part of the entire processing steps towards ceramic object, leaving ceramic powder fabrication before the AM process and firing of the green body after the AM process.

1.2.3 Additive manufacturing of ceramics

Ceramics possess exceptional mechanical properties, such as high hardness and strength, high temperature resistance (refractory), and chemical resistance (inertness). Therefore they have found diverse applications in multiple fields. They are traditionally formed by slip casting, injection molding or various pressure-assisted techniques. As all of these methods rely on the usage of molds, the shape of the ceramic parts is restricted to relatively simple geometries. The machining of complex shapes is furthermore hindered by the high hardness and brittleness of ceramic materials. Additive manufacturing (AM) heralds a new era in fabrication of ceramics. As AM technologies are based on the layer by layer joining of materials, they neither require molds nor are limited by the hardness and brittleness of ceramics. This in turn allows for the fabrication of complex parts that utilize the exceptional properties of ceramics as mentioned above. Hence, to process ceramic materials through additive manufacturing has gathered a lot of interest. It is believed that some of the industrial applications of ceramics AM will soon become

economically profitable ⁴⁷. However, achieving additive manufacturing of ceramics has been a complicated endeavor, as the prior feedstock fabrication and post sintering steps are full of challenges just like in any ceramic fabrication process.

There are several AM technologies suitable for shaping ceramic components, and there are several review papers have discussed them intensively ⁴⁷⁻⁵⁰. According to Zocca et al. ⁴⁸, AM technologies can be divided into two categories, direct and indirect manufacturing, depending on the way the feedstock material is deposited.

- Direct: The feedstock (ceramic in this case) is directly deposited in the position according to the 2D slices of the 3D geometry of final ceramic components. The ceramic AM technologies included in this category are: direct inkjet printing and Robocasting (also known as direct ink writing)
- Indirect: A complete layer of feedstock material is deposited first, subsequently the material is selectively joined to form 2D slices. These two steps are repeated until the final 3D shape is complete. The ceramic AM technologies included in this category are: powder based 3DP/SLS, slurry based 3DP/SLS and SLA.

In the following section a detailed introduction of ceramic AM technologies will be discussed to give an overview of the principles of each technique and evaluate them with respect to the properties of the final ceramic components.

Direct AM technologies for ceramics

(A) Direct Inkjet Printing (DIP) utilizes ceramic powders dispersed in a liquid carrier as ink and selectively deposits ink droplets through a print head onto the building platform. Upon deposition, droplets will be solidified by either drying or UV curing to provide sufficient mechanical stability and accumulate the 3D structures by

1.2 Additive manufacturing of ceramic materials

repeating the process. Liquid carriers usually are water, organic solvents or photopolymers, with additives to enhance the stability. Solid loading of the ceramic powder (typically < 30 vol%), viscosity of the suspension and its surface tension directly influence the formation of a stable droplet and its spreading into an equilibrium shape upon impact. DIP allows fabrication of relatively dense ceramic components after the debinding and sintering process, as ceramic particles used are generally in the submicrometer range, as they avoid blocking of the deposition nozzle of the print head and provide excellent sintering activity. Furthermore, relatively good surface quality and precision control can be achieved due to the ultra-small volume (picoliter) of each single ink droplet.

DIP has been utilized to produce oxide and non-oxide ceramic components. Cappi et al.⁵¹ studied the potential of DIP to manufacture ceramic layers as well as 3D-components based on an aqueous ink of silicon nitride (LPS-Si₃N₄) suspension with organic additives. Fabricated and sintered Si₃N₄ specimen were found to possess promising mechanical properties, with HV 0.2 hardness of 17 and fracture toughness of 4.4 MPa·m^{0.5}. The study demonstrates high potential of additive manufacturing of non-oxide high performance ceramics with DIP. A special approach based on DIP by utilizing preceramic polymers dissolved in organic solvents as ink was reported by Mott and Evans⁵². They used polycarbosilane as the SiC based ceramic precursor and SiC powders as inert fillers to print a simple geometry, the addition of SiC powders reduced the risk of cracking upon pyrolysis.

(B) Direct Ink Writing (DIW, Robocasting) for ceramic fabrication assembles 3D complex geometries through extruding an ink consisting of a ceramic paste or slurry by controlling a nozzle. Direct deposition of ceramic slurries in a defined pattern is one of the most accessible and popular AM technologies and it is very suitable for fabricating porous lattice structures. In contrast to the DIP technique, the ceramic slurry after deposition in DIW or robocasting does not require an additional curing or drying process, as it exploits the shear-thinning behavior of the prepared ink. Ceramic slurries or

pastes with high solid loading behave like a high viscous gel when loaded inside the extruder. Upon extrusion through the nozzle the induced shear stress will break down the gel structure of the ink and significantly decrease its viscosity, which allows the ink to be deposited smoothly. Immediately after extrusion, the ceramic ink is back to static state and recovers its high viscosity, which will preserve the printed pattern and avoid undesired deformation. Different parameters such as pH value, ionic strength, addition of polyelectrolytes and utilization of polymeric binder and plasticizer can lead to the shear-thinning behavior^{53, 54}. The nozzle typically has a size of 100 – 1000 μm , which restricts the printing resolution and surface quality. Hence DIW has been frequently used to produce scaffolds and lattice like structures. Cai showcased SiC scaffold produced by robocasting aqueous colloidal ink consisting of SiC, Al_2O_3 and Y_2O_3 particles in a polymer solution⁵⁵. By utilizing low pressure spark plasma sintering technique, the SiC based structure achieved 97 % of theoretical density and displayed ~ 22.8 % linear shrinkage. Pre-ceramic polymer can be utilized in this approach as well. Pierin et al.⁵⁶ reported the production of micro-sized SiOC scaffold with good compressive strength of 2.5 MPa by DIW a silicon pre-ceramic polymer mixed with cross-linked silicone powders. The addition of small amounts of GO flakes was further proved to reduce the overall shrinkage and retain the printed structure.

Indirect AM technologies for ceramics

(A) Powder based 3D Printing (P-3DP) can be categorized as a binder jetting technique according to the material joining principle based on the ISO 17296-2 standards⁴⁴. The general printing process is as follows: first, the flowable ceramic powder is uniformly deposited over a complete layer; subsequently an inkjet printing head ejects liquid binder to selectively join particles. These two processes are repeated until the final structure is achieved. Since the printed parts are constantly immersed inside the powder bed, supporting structures are not required in this process. When integrating multiple

1.2 Additive manufacturing of ceramic materials

print heads (up to a few hundreds) simultaneously, huge ceramic objects up to $6 \times 6 \times 6 \text{ m}^3$ can be fabricated. P-3DP is very well suited for fabricating porous structures because of the low packing density ($< 25 \% \text{ TD}$) of the powder bed and the large particle size for good flowability, thus majority of research work is devoted to biomedical scaffolds. Nonetheless, SiSiC lattice structures have been fabricated by 3D printing from Si/SiC/dextrin powder bed, followed with preceramic polymer infiltration and Si melt infiltration ⁵⁷. The resultant SiSiC with optimized starting composition was dense with porosity less than 1 %, and the mechanical properties were found to be scaled linearly with the volume fraction of Si. An alternative approach based on 3D printing preceramic polymer powder bed has been developed by Zocca et al. ⁵⁸ by mixing the cross-linking catalysts with the preceramic polymer or with the printing liquid solvent. Both approaches were proved successful, and SiOC ceramics with ordered porosity can be obtained.

(B) Powder-Based Selective Laser Sintering (P-SLS): This process is similar to the P-3DP technique, as it starts with the deposition of a complete layer of powder. A laser beam is then used to inscribe the cross section information into the powder by locally melting or sintering the particles. Direct laser sintering of ceramic powders is very challenging due to their poor thermal shock resistance, therefor cracks are unavoidable after cooling. Wilkes et al.⁵⁹ reported that by preheating the powder bed to $1600 \text{ }^\circ\text{C}$, the thermal shock will be less intense. An alternative approach is mixing the ceramic powder with a binder phase (organic or inorganic), which can be easily melted or sintered by the laser beam to join the ceramic powder. Ceramic parts produced via this approach are highly porous and similar in quality to the parts produced with P-3DP. In addition, preceramic polymers can again provide an interesting alternative with the powder-bed SLS. Friedel et al. ⁶⁰ reported utilizing SiC powder filled with solid polysiloxane resin. The CO_2 laser beam induces the local curing reaction of the silicone which acted as binder for SiC. SiOC/SiC/Si dense composites can be obtained after the pyrolysis

and post-infiltration with Si melt. The resultant bending strength can be significantly increased to 220 MPa.

(C) Slurry based 3DP (S-3DP) and Slurry based SLS (S-SLS): Slurry based 3DP and SLS techniques ⁶¹ are different from powder bed based as they utilize a ceramic slurry instead of dry powder, exploiting the merits of high powder packing density and the usage of fine particles. This concept was introduced early on in the significant patent “Three-dimensional printing techniques” by Sachs et al. ⁶². They stated that dispersing powders in a liquid vehicle is beneficial for required rates and densities. The slurry deposition is similar to tape casting where a thin layer of ceramic slurry is deposited, which will immediately form a cast when in contact with the previously deposited and subsequently dried layer. This process applies the principle of slip casting assisted by capillary gravitational force. One of the major advantages of utilizing slurry deposition is that high powder bed green densities (60 % of TD) are achievable, which enables obtaining fully dense parts after sintering. Therefore, it is believed slurry based 3DP or SLS has the potential to manufacture parts comparable to those manufactured by traditional ceramic processing routes.

(D) Stereolithography (SLA): Ceramic stereolithography will be discussed in detail in the following section.

1.2.4 Ceramic stereolithography

Stereolithography is one of the first AM technologies, invented by Charles W. Hull in the mid-1980s. It is based on photopolymerization of a liquid resin, therefore it belongs to the AM category of VAT photopolymerization. The working principle is as follows. First a tank (vat) is filled with a photopolymerizable resin. The building platform will then be immersed in the resin and placed at one-layer thickness below the resin surface. The cross section information of the 3D model is inscribed through a scanning laser or image projection, e.g. a Digital Micro-Mirror Device (DMD). After

1.2 Additive manufacturing of ceramic materials

one layer is complete, the platform will further dive down for one-layer thickness by a Z-axis motor and repeat the photocuring. These steps will be repeated until the final 3D object is achieved.

SLA has been modified to 3D printing ceramic materials by utilizing resins based on dispersing ceramic particles in liquid photopolymer. Upon photocuring, the liquid polymer solidifies and bonds ceramic particles together as glue. A typical ceramic slurry for stereolithography will include low viscous photopolymer (mostly acrylate based), photoinitiator, solvent (optional, aqueous or organic) to reduce the viscosity, dispersant for the particle dispersion, and ceramic particles with a concentration of 40 – 60 vol %^{63–68}. The obtained ceramic/polymer composites will be fired in air to remove the organic contents and the ceramic powder will be sintered at higher temperature. Due to the high volume fraction of ceramics and the utilization of fine particles, the production of dense monolith components and cellular structures with dense struts are possible.

In Figure 3, one example of ceramic components fabricated by SLA are shown, a highly transparent glass structure (after sintering) fabricated from a photopolymer filled with a high volume fraction of fused silica powder by Kotz et al.⁶⁹.



Figure 3. Printed and sintered SiO₂ glass structure (pretzel) with high optical transparency manufactured by SLA⁶⁹. Reprinted by permission from F. Kotz et al.: ‘Three-dimensional printing of transparent fused silica glass’, *Nature*, 2017, 544(7650), 337-339. Copyright 2017 Springer Nature.

As stated in the previous section, ceramic AM technologies only accomplish the shaping process inside a complete ceramic fabrication procedure. Ceramic stereolithography is the same, as the printed ceramic/polymer composite is only the green body of the desired ceramic component. Post treatments like debinding and sintering are required to achieve the ceramic's valuable properties, which are directly related to the composition and microstructure after sintering. In order to obtain adequate sintering activity, a high volume fraction of ceramic powders (generally > 50 %) and small particle sizes are required. The fabrication characteristics of such high solid loading resins are significantly changed and become more challenging when compared to the handling of pure photopolymers. In the following sections, we will closely discuss the problems and challenges of ceramic stereolithography.

(i) Rheological behavior: of ceramic filled resin is one of the key factors influencing the deposition of a fresh layer. After photocuring of one layer, the platform will move down a certain depth (layer thickness), and a new layer of resin has to be applied on top of the first one. This process is known as recoating. Resins with low viscosity can recoat themselves quickly and efficiently with high surface quality, while voids and air bubbles are absent. Therefore resins applied in SLA are generally required to possess a viscosity lower than 3000 mPa·s⁷⁰.

However, ceramic resins applied in stereolithography are generally highly loaded. Consequently, the viscosity of the resin dramatically increases and self-recoating in a reasonable time is almost impossible. Figure. 4 shows the rheological behavior of a photopolymer filled with different amounts of ceramic powder hydroxyapatite (HAp). The photopolymer's dynamic viscosity at a shear rate of 25 s⁻¹ increased from 45 mPa·s to 390 and 3300 mPa·s (almost 100 times of the original viscosity) when loaded with 10 wt % and 25 wt % HAp, respectively. When self-recoating is not possible, doctor blades are frequently used in stereolithography to enable the recoating of thick ceramic resins. An alternative solution is to add diluents, which should possess low viscosity, good

1.2 Additive manufacturing of ceramic materials

miscibility with the photopolymer and low evaporation temperature to facilitate the post drying process. Figure. 4 (red line) also demonstrate that by adding certain amount of diluent, viscosity of ceramic powder filled resin can be reduced to a degree where self-recoating is possible again.

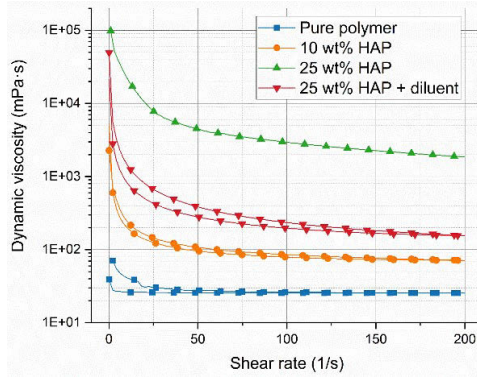


Figure. 4 Viscosity of hydroxyapatite filled photopolymer resin with different solid loading and diluent ⁷¹.

(ii) Curing characteristics: Ceramic particles suspended in the photopolymer can have strong interaction with the incident light in the fashion of absorbing and scattering (reflecting), which significantly alters the curing behavior of the photopolymer. When the ceramic resin is exposed to a laser beam, a solid cure track is created. There are two characteristics related to the curing profile, curing depth (C_d) and curing width (ω_{cure}). The curing depth can be described with the following Equation 1 derived by Jacobs ⁷²,

$$C_d = D_p \cdot \ln\left(\frac{E}{E_c}\right) \quad \text{Equation 1}$$

where D_p is the attenuation length, E the energy reached at the surface of the resin, E_c the critical energy of photopolymerization, which is the minimum energy required to the gel point. The introduction of ceramic powders has direct influence on the

attenuation length of the incident light ⁴⁹, that D_p largely depends on the average particle size (d_{50}), wavelength of incident light (λ), refractive index of the photopolymer (n_0), volume fraction of ceramic powder (Φ) and refractive index (RI) contrast Δn , which is given by $\Delta n = n_c - n_0$ (refractive index difference between ceramic powder and photopolymer).

$$D_p \propto \frac{2}{3} \cdot \frac{d_{50} \cdot \lambda \cdot n_0}{\Phi \cdot \Delta n^2} \quad \text{Equation 2}$$

As seen in Equation 2 with Δn being the only term squared, it shows refractive index contrast has a dominant role on determining the attenuation length so on the curing depth. Figure 5 shows that the curing depth of a ceramic (SiO_2) filled resin is inversely proportional to the square of the refractive index contrast between ceramic powder and photopolymer solution.

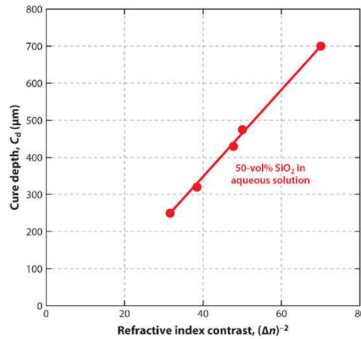


Figure 5. Measured curing depth (C_d) of 50 vol % suspension of SiO_2 powder ($d_{50} = 4.64 \mu\text{m}$) in acrylamide solutions with respect to the refractive index contrast using a 365 nm collimated light source ^{73, 74}. Reprinted by permission from J. W. Halloran: ‘Ceramic Stereolithography: Additive Manufacturing for Ceramics by Photopolymerization’, Annual review of materials research, 2016, 46(1), 19-40. Copyright 2001 Annual Reviews, Inc.

Not only is the curing depth of the ceramic filled resin largely reduced, moreover it creates a broadening effect, the curing profile is

1.2 Additive manufacturing of ceramic materials

wider than the laser beam. In the absence of scattering, the width of curing (ω_{cure}) should simply reflect the intensity distribution of a laser beam, which is a Gaussian distribution (bullet shape). Nonetheless, the real curing profile of a ceramic filled resin is notably altered as can be seen in Figure 6. The cured line of a ceramic resin with low refractive index contrast and under low energy exposure has almost the same width as the laser beam, while the width of curing is significantly widened under high-energy exposure. Moreover, ceramic resins with high refractive index contrast had already demonstrated sizable broadening phenomenon even under low energy exposure. The smallest feature detail (resolution) obtainable in SLA cannot be finer than the resolution of the light source. Ceramic resins suffer from a severe broadening effect, consequently the resolution of ceramic SLA will be further degraded compared to pure polymer SLA.

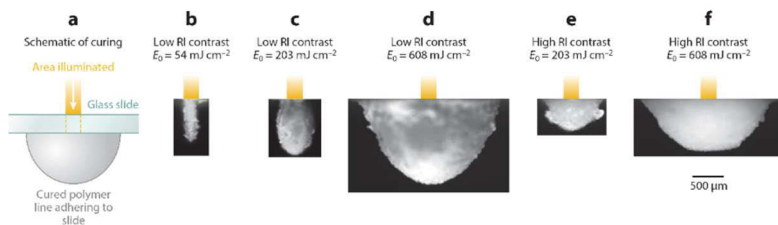


Figure 6. Shape of the curing profile in SiO_2 suspension with photopolymer varying its refractive index. Significant broadening of curing width is observed in the case of high energy exposure and in the resin with high RI contrast⁷⁴. Reprinted by permission from J. W. Halloran: ‘Ceramic Stereolithography: Additive Manufacturing for Ceramics by Photopolymerization’, Annual review of materials research, 2016, 46(1), 19-40. Copyright 2001 Annual Reviews, Inc.

In summary, the ceramic powder’s absorption and scattering of incident light dramatically changed the photopolymers curing behavior. The higher the refractive index contrast, the more light will be scattered and absorbed. Likewise, some ceramic materials are opaque under UV light, as they demonstrate strong absorption coefficients. Hence, many ceramic SLA technologies are focused on

the fabrication of UV transparent and low RI ceramics (SiO_2 , Al_2O_3), while utilizing SiC , Si_3N_4 and ZrO_2 in SLA is far more challenging.

1.2.5 Stereolithography of PDCs

SLA of ceramic-photopolymer suspensions has been frequently employed for 3D printing of ceramics. This procedure however requires the homogeneous dispersion of particles to ensure good surface quality and resolution. Additionally, the scattering of incident light with particles is a major problem encountered when the refractive index mismatch is significant, thereby degrading the printing resolution. Meanwhile, utilizing preceramic polymers in SLA is a promising approach to combine the surface smoothness and high resolution of polymer SLA with ceramic's intrinsic properties. The main challenge of this approach however lies in the fact that preceramic polymers requires sufficient and efficient photocuring ability to allow the utilization in stereolithography based technologies. Several strategies have been provided to solve this issue, including chemical functionalization of preceramic polymers with acrylate or methacrylate groups, physical blending preceramic polymers with sacrificial photopolymers and the utilization of two reacting oligomer precursors.

Table 3 gives an overview of SLA of preceramic polymers using different strategies and specifications regarding the pyrolyzed ceramics.

1.2 Additive manufacturing of ceramic materials

Table 3. Main strategies used for the stereolithography of polymer derived ceramics.

Photocurability	Preceramic polymer Commercial name	Method	Size	Pyrolysis T and atmosphere	Dense	Yield [%]	Shrinkage [%]	Composition	Ref.
Acrylate functionalization via condensation	Vinylsilazane K6ON VL-20	TPP	micro	600 °C, N ₂	yes	72	41	SiOCN	75
	Silsesquioxane SILRES MK	SLA	macro	1000 °C, N ₂	yes	55	25	SiOC	76
	Silsesquioxane SILRES MK	SLA	macro	1200 °C, N ₂	no	45	unknown	SiOC-Zr-Ti	77
Blending with photopolymer (acrylate resin for ^{79, 80} , acrylate silicone RC.711 for ⁸¹)	acrylate siloxane TEGO RC.711	TPP	micro	1000 °C, N ₂	yes	7.4	42	SiOC	78
	Allylcarbosiilane SMP10, SMP877	SLA	macro	1300 °C, Ar	no	20	35-50	SiC	79
	Polysiloxane SILRES MK, H62C, Siles 610	SLA	macro	1000 °C, N ₂	yes	60	40-50	SiOC	81
	Borosilazane PBSN	SLA	macro	900 °C, N ₂	no	58	30	SiBCNO	80
Two oligomeric precursors (thiol-ene chemistry)	(mercaptopropyl) methylsiloxane, vinylmethoxysiloxane from GLEEST	SLA	macro	1000 °C, Ar	yes	58	30	SiOC	82
	Allylcarbosiilane SMP 10	μSLA	micro	1000 °C, Ar	yes	58	30	SiOC	83
Photohydroxylation catalyst (CpPnMc ₃)	Allylcarbosiilane SMP 10	TPP	micro	600 °C, N ₂	yes	94	0	SiC	84
Impregnation of 3D printed photopolymer lattice with PCIP	Vinylsilazane Durazane 1800	SLA	macro	1000 °C, Ar	no	41	unknown	SiCNO	85

As early as 2006, it was reported that via the functionalization of polyvinylsilazane with 2-isocyanatoethyl methacrylate, the resultant polysilazane can be 3D printed with nano-stereolithography to achieve complex three dimensional SiCN microstructures ⁷⁵. Zanchetta and Colombo et.al reported in 2016 the real first successful 3D printing of macro-sized methyl- silsesquioxane (MK), that was modified with methacrylates into a photocurable preceramic polymer ⁷⁶. The modification was achieved through hydrolysis and condensation reactions between MK and 3-(trimethoxysilyl)propyl methacrylate (TMSPM). They demonstrated the 3D fabrication of a cellular lattice with strut sizes down to 200 μm . With subsequent pyrolysis, the printed structure was successfully converted into a SiOC ceramic with exceptional surface quality.

Later in the same year, researchers in the HRL laboratories developed a photocurable preceramic resin system by mixing vinylmethoxysiloxane with (mercaptopropyl) methylsiloxane ⁸². The photopolymerization is based on the classic thiol-ene click reaction, which was discussed previously (section 1.1.2). They used two different additive manufacturing technologies; conventional SLA, which requires the addition of photoabsorbers to confine the curing area, and one that is based on self-propagating photopolymer waveguide technology (SPPW), which relies on the self-focusing effect that light is tunneled towards the tip of a photopolymer and causes the polymerization to keep propagating. Ceramic parts fabricated via SPPW showed very smooth surfaces along the printing direction, whereas conventional SLA printed parts showed typical step-like surfaces due to the layer by layer fabrication, which could negatively affect the mechanical performances. Consequently, SiOC micro lattices fabricated via SPPW exhibited strength 10 times as high as commercially available ceramic foams with similar density. Despite the potential of the thiol-ene click reaction as a convenient photopolymerization mechanism for preceramic polymers, further studies regarding SLA of other classes of preceramic polymers have not been demonstrated.

1.2 Additive manufacturing of ceramic materials

Apart from chemically modifying the preceramic polymers or building the polymer structure with two oligomeric precursors, which can allow photopolymerization, there is a third approach to process preceramic polymers by SLA/DLP technique: physically blending the non-photocurable preceramic polymer with a sacrificial photopolymer or photocurable preceramic polymer. Hazan and Penner prepared blended polycarbosilane (AHPCS and AMHPCS) with multifunctional acrylate monomers as photocurable resin and successfully 3D printed complex structures by using a benchtop SLA printer⁷⁹. Nonetheless, the ceramic yield after pyrolysis was extremely low (20 % and 37%) and the ceramic components obtained were highly porous. Alternatively, Schmidt and Colombo⁸¹ utilized a commercial photosensitive acrylic preceramic polymer (RC 711) and mixed it with preceramic polymers with high ceramic yield. By optimizing the resin system, in terms of blends composition, concentration of photoinitiators/photoabsorbers and exposure time, they produced delicate kelvin cell structures and dense SiCO components through pyrolysis. A maximum ceramic yield of 60.2 % was obtained. However, the blending approach cannot resolve the issue regarding oxygen contamination coming from the acrylates.

1.3 Freeze casting of porous ceramics

Engineering ceramic materials are generally sintered to be fully dense without porosity, as pores can act as stress concentrators that lead to fracture defects, and largely degrades the mechanical reliability. On the other hand, porous structures are found frequently in nature, e.g. in bones and nacre⁸⁶, due to their optimized strength to density ratios. Pores can be considered an advantage in applications where high transport capabilities, controlled permeability, low density and high specific strength are desired. There are numerous industrial applications, including catalysts, catalyst support, filtration, absorption and thermal insulation, where porous ceramic structures are utilized as core components. Such strategy combines the

advantages of dispersing pores into a matrix with the merits of ceramics, e.g. their exceptional mechanical properties, good resistance against high temperature and corrosive environment.

Traditional processing techniques towards porous ceramics include partial sintering, sacrificial fugitives, replica templates and direct foaming. Each of these methods have their own restrictions and can only control the pore parameters, e.g. pore size, pore shape, pore distribution and porosity, to a narrow extent. Among them, freeze casting, also called ice templating, is one of the novel methods to fabricate porous ceramic components with well controlled microstructures.

The ceramic freeze casting method relies on freezing a ceramic colloidal suspension (water or organic solvent based), followed by low pressure sublimation of the solidified phase directly into gas phase and subsequent sintering to densify the ceramic walls. The obtained porous structure is a replication of the solidified solvent crystals, therefore pore morphology can be well controlled by adjusting the freezing conditions (freezing rate, freezing direction and freezing temperature), the solvent and additives. Unidirectional pore channels can be obtained if unidirectional freezing is utilized. Until now, water, camphene, tert-butanol, cyclohexane and other solvents with relatively high melting points and fast and easy evaporation have been successfully utilized as freezing liquids in the freeze casting process. The obtained unique, complex and controllable pore morphology is a demonstration of its distinct advantage. Freeze casting is a versatile approach that is applicable to various materials, including polymers, metals and ceramics. Furthermore, it is a cost-effective production method with simple equipment requirements and in most cases water is used as a solvent, which also provides an ecological advantage.

1.3.1 Processing principles

Figure 7 demonstrates the processing steps of freeze casting with regard to the physical properties of the utilized solvent; in this case water and a dispersed ceramic powder. The freeze casting

1.3 Freeze casting of porous ceramics

method relies on freezing a ceramic colloidal suspension (water or organic solvent based), followed by low pressure sublimation of the solidified phase directly into the gas phase and subsequent sintering to densify the ceramic wall.

(a) Ceramic slurry preparation: The ceramic slurry preparation is very similar to the processing steps in slip casting, in which suitable ceramic powders are dispersed uniformly in a liquid medium. Moderate solid loading, generally less than 40 vol %, is utilized to fabricate highly porous structures. The stability of the slurry must be carefully established, so that sedimentation OR agglomeration of the ceramic particles do not occur during the second step, thus dispersants or plasticizers are often utilized to ensure a stable slurry. Additionally, binders have to be incorporated to provide sufficient green strength after freeze drying. Otherwise the green body would collapse due to the absence or weak joining force between the ceramic powders. Polyvinyl alcohol (PVA) is a widely used binder for water based freeze casting slurries.

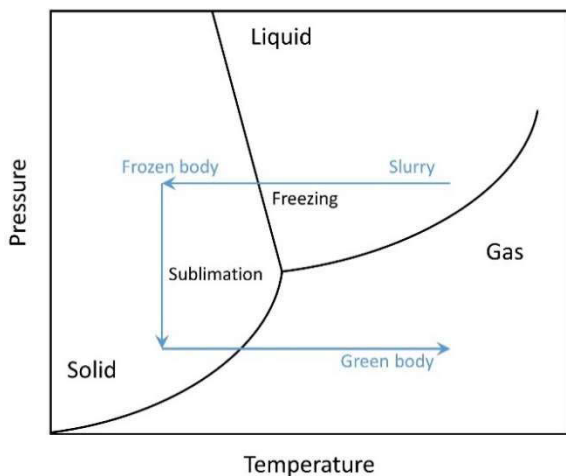


Figure 7. Fundamental processing steps of freeze casting technique. Each processing steps is explained in detail in the text. The figure is redraw from ⁸⁷.

(b) Controlled freezing of ceramic slurry: This is the critical step of freeze casting in which the microstructure is determined and pore characteristics are decided. When the ceramic slurry is being frozen, solvent crystals start to grow along the temperature gradient (cooling direction), consequently expelling, concentrating and trapping the ceramic particles in between the growing solvent crystals. This natural segregation is frequently seen in the case of freezing brine, where salt channels are observed after water is dried out⁸⁸. In order to control the freezing conditions, the ceramic slurry is generally casted inside a mold and encountered with a cooling front. Anisotropic solidification is induced when under unidirectional freezing, isotropic solidification is induced under shock freezing.

(c) Freeze drying / sublimation: Once the slurry is completely frozen, the sample is transferred to an environment with low pressure and low temperature, depending on the physical properties of the solvent used. The drying condition has to be tailored below the triple point (critical point) of the solvent, so that direct liquid to gas phase transformation is avoided. The porous structures are created when solidified solvent crystals sublimate out of the sample. The remaining pore channels represent the morphology of the solidified solvent crystal, which is determined by the solvent type and freezing conditions.

(d) Sintering: After the solvent has been completely removed, the ceramic green body will be sintered to achieve its exceptional mechanical properties with conventional sintering techniques. The green strength provided by the organic binder is insufficient in many applications where the ceramic components are under load. Therefore, the sintering process includes both the removal of the organic binder and the consolidation of the ceramic powder. The low amount of organic binder used as well as the presence of interconnected pore channels facilitate the debinding process of freeze casted samples, whereas it is more problematic in other ceramic processing techniques (gelcasting, 3D printing).

1.3 Freeze casting of porous ceramics

1.3.2 Pore morphologies

The solidification process of a liquid solvent has a dominant influence on the produced pore morphology, as different solvent solidify into different microstructures based on the crystal growth. The crystals of both camphene and cyclohexane have a dendritic morphology while tert-butanol displays a prismatic and needle like crystal growth. Ice shows unique behavior when utilized in freeze casting, as it undergoes volumetric expansion while freezing and creates a lamellar microstructure due to the anisotropic growth of the solidifying crystals. As a result, various solidification behaviors of liquid carrier are reflected in the final freeze casted ceramic microstructure.

Homogeneous pore morphology requires homogeneous freezing conditions. That means cooling at a constant rate starting from room temperature. Nonetheless, freeze casted samples often demonstrate anisotropic pore morphology along the freezing direction that can be separated into several zones. Deville et al.⁸⁹ investigated the directional solidification behavior of alumina suspensions through X-Ray radiography and tomography. He observed a pore structure transition from bottom to top. Near the cold surface (copper at the bottom) homogeneous nucleation occurs due to high supercooling. Under higher supercooling degree, nucleation rate is higher than crystal growth rate, thus nucleation dominates the solidification process. Therefore, a more densely packed structure is seen. Then, ice crystals start to grow both parallel to the freezing direction and vertical to the freezing direction due to diminishing ice front velocity. In this area, crystal growth is more dominate than nucleation, hence the appearance of large ice crystals. When the solidification further proceeds, obvious phase morphology occurs as the ice crystals become more homogeneous and parallel aligned to the freezing direction. This is due to the more significant and clearer temperature gradient. Meanwhile additives have been utilized to modify the freezing parameters, as they bind with the solvent and hinder random crystal growth. For example, adding

glycerol to aqueous suspension is reported to have the effect of improved ice crystal uniformity and results in more homogeneous microstructures⁹⁰.

1.3.3 Freeze casting of PDCs

The polymer to ceramic conversion in PDCs is accompanied with volume shrinkage, gas release and porosity formation. Pyrolyzing preceramic polymers typically leads to large crack and defects formation, sometimes even explosion due to gas evolving inside the ceramic body. This makes the direct fabrication of dense ceramics from preceramic polymers extremely challenging. The exception being one or more of the PDC parts dimensions are less than several hundred micrometers. Nonetheless, porous ceramics are an alternative to utilize polymer derived ceramics in a large bulk form, since thin cell walls are in the thickness of hundreds of micrometers and the presence of porosity facilitates the gas release. There are several processing methods for the production of porous ceramic from preceramic polymers. These include replica technique by coating a solid template with preceramic polymer followed by pyrolysis, self-foaming by in situ forming gases species during the cross-linking reaction, adding solid blowing agent to the silicone melt, blowing of CO₂ gas and using sacrificial polymeric templates (mostly beads). There are several review articles regarding the production of porous polymer derived ceramics^{91, 92}. Recently, freeze casting has attracted more and more attention as an emerging processing technique to fabricate highly aligned and hierarchical porous polymer derived ceramics⁹³.

Yoon et al. give one of the earliest report regarding freeze casting preceramic polymer in 2007. They produced highly aligned porous SiC ceramics by directionally freezing a polycarbosilane/Camphene solution^{94, 95}. The preceramic polymer solution (5 to 20 wt % of polymer in camphene) was first heated to 60 °C to allow a uniform dissolution. It was subsequently casted into a PE mold, which allowed the directional freezing using cold ethanol

1.3 Freeze casting of porous ceramics

or liquid nitrogen from the wall to the center of solution. The frozen camphene was sublimated in a freeze dryer. The obtained green body was then cross linked in air (250 °C) and pyrolyzed in Ar to 1400 °C to form SiC based ceramics. The resultant pore structure is well defined by the growth of camphene crystal. They found the pore size decreases with reduced cooling temperature and increased polymer concentration. It is noteworthy that the polymer was not cross linked nor binders were utilized, the mechanism for the mechanical integrity of freeze casted polycarbosilane green body is inexplicable. Commercially available polymethylsiloxane (PMS) was used as well in solution based freeze casting as preceramic polymer ⁹⁶. The PMS polymer was initially cross linked to a certain extent by the addition of cross-linking agent, then under controlled freezing condition phase transformation (dissolution of polymer from solvent) was induced. They claim that the initial cross-linking is an essential step to ensure the mechanical integrity after solvent removal and avoid melting or collapsing during pyrolysis. Three organic solvents were utilized to demonstrate the potential of freeze casting of PDCs (see Figure 8). The preceramic polymer PMS processed with tert-butanol (tBa) showed prismatic pore morphology, as tBa is a highly faceted solvent. In contrast, cyclohexane and camphene produce dendritic structures. This interfacial solidification anisotropy is correlated with the Jackson α -factor ⁹⁷, that means solvents with low α -factor value (e.g. cyclooctane) lead to the formation of very isotropic microstructures. The increased α -factor of a solvent (e.g. cyclohexane) produces more dendritic structures, eventually causing a lamellar structure of highly faceted crystal growth (e.g. water, dimethyl carbonate).

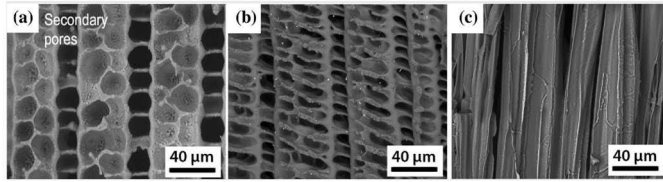


Figure 8. SEM images of porous PDCs produced by freeze casting PMS using different solvents, which determines the pore morphology (a) cyclohexane (b) camphene (c) TBA ⁹⁶. Reprinted by permission from M. Naviroj et al.: 'Directionally aligned macroporous SiOC via freeze casting of preceramic polymers', *Journal of the European Ceramic Society*, 2015, 35(8), 2225-2232. Copyright 2015 Elsevier.

The same group later compared between suspension- and solution based freeze casting for the preparation of porous ceramics⁹³. Alumina powder and PMS as preceramic polymer were each suspended or dissolved in various solvents (cyclooctane, cyclohexane, dioxane, or dimethyl carbonate) and freeze casted to produce porous ceramic components with roughly 70 % porosity. Differences were observed in systems using cyclohexane and dioxane as solvents, clear dendritic characteristics were generated in the solution based freeze casting but not in suspension based. Disturbances caused by presence of particles are believed to be the cause. Overall, solution based freeze casting does not distinguish significantly from suspension based freeze casting in pore morphology. Nonetheless, the solution processing provides several advantages including simpler preparation of the solution, long stability and clear solution which allows direct observation of the ice front.

Our group has developed an interesting approach towards macroporous SiOC/SiO₂ ceramic nanocomposites from preceramic polymers H62C and amorphous silica derived from rice husk using both tert butanol and water as freezing liquid ⁹⁸. In this work, dextrin and polyvinylbutyral were utilized as organic binder to enhance the mechanical stability, and various dispersants were employed to achieve stable suspension. Most importantly, water based freeze casting of liquid H62C with SiO₂ particles was successfully developed

1.3 Freeze casting of porous ceramics

by employing suitable dispersant, emulsifier and binders to achieve stable emulsion/suspension, which demonstrates an environmentally friendly process to produce macroporous polymer derived ceramics.

Hierarchical porous polymer derived ceramics with micro-meso-macro porosity are obtained as well through freeze casting. Zhang et al. used pre-pyrolyzed polysiloxane as ceramic precursor and silica sol as a binder and template source to apply water based freeze casting⁹⁹. After pyrolysis, SiOC ceramic monoliths with hierarchical porosity and a surface area of 74 m²/g were preserved even up to 1000 °C pyrolysis temperature. They believe the microporosity resulted from the decomposition of preceramic polymer, and mesopores were generated through particle packing. They further developed an approach to alter the hydrophobicity of polysiloxane to become hydrophilic through chemical modification¹⁰⁰. The surface of hydrophobic PMS MK was modified with a hydrophilic agent (3-aminopropyl)triethoxysilane (APTES) and the subsequent pyrolysis resulted in the formation of a negatively charged surface, which is ideal for water based freeze casting. This approach can be applied to other polysiloxane as well. During the preparation of this doctoral thesis in the end of 2018, a novel approach, which combines the solution based freeze casting of a liquid polysilazane with photo-induced thiol-ene click reactions, was reported by Obmann and Konegger for the fabrication of highly porous silazane derived ceramics¹⁰¹. Camphene was utilized as pore forming solvent, and quaternary thiol with photoinitiator was added to the preceramic polymer solution to induce the photopolymerization at -10 °C. The reported approach is extremely similar to the method I have developed for the freeze casting of polymer derived ceramics in this work as can be seen in chapter 5. An overview of freeze casting of polymer-derived ceramics is given in Table 4.

As a summary, there are few reports regarding the fabrication of macroporous polymer derived ceramics with freeze casting technique. The challenge of freeze casting of PDCs lies in the difficulty to retain the polymer's shapes after the drying process. Because the majority of preceramic polymers are in liquid state at

room temperature, and their cross-linking mechanism involves heat treatment, which is fundamentally against the freeze casting concept. With the reported processing routes, they either require complex and time consuming suspension preparation or precise control over the cross linking degree of preceramic polymers. And each proposed method can only be applied with certain types of preceramic polymers, which further restrict their applications.

1.3 Freeze casting of porous ceramics

Table 4. Overview of freeze cast polymer-derived ceramics.

Pre-ceramic polymers Commercial name	Solvent	Cooling conditions	Pore size	Pore morphology	Cross-linking/binding mechanism	Compositions	Ref.
Carbosilane PCS Nippon	camphene	20 ~ - 40 °C	23 – 11 µm	dendritic	oxidation curing	SiC	95
Polysiloxane SILRES MK	cyclohexane camphene tert-butanol	- 35 °C	10 – 50 µm	dendritic dendritic prismatic	partially cross linking prior freeze casting	SiOC	93,96
Polysiloxane SILRES H44 silica sol	water	- 20 ~ - 150 °C	1 – 10 µm 2 – 12 nm	lamellar	silica sol as binder, pre-cross-linking PCP to powder form	SiOC/SiO ₂	99, 100
Polysiloxane SILRES H62 C Rice husk derived SiO ₂	tert-butanol water	2 – 6 °C/min	1 – 50 µm	prismatic lamellar	Organic binders TVB for TBA Dextrin for Water Silica as fillers	SiOC/SiO ₂	98
Polysilazane Durazane1800	camphene	2 – 8 °C/min	10 – 20 µm	dendritic	frozen state photopolymerization	SiCN	101

2 Materials and Methods

2.1 Synthesis, fabrication and processing of materials

2.1.1 Materials used in this work

An overview about the materials used for the synthesis, processing and fabrication of samples is given in Table 5.

The polysiloxanes SPR212 and Silres H62C, polycarbosilane StarPCS SMP-10 and polycarbosilazane Durazane 1800 are utilized as the representative preceramic polymers. Their pyrolysis under an inert atmosphere yield SiOC, SiC and SiCN-based ceramic compositions, respectively.

For the thiol-ene click reactions, two thiols are employed, 1,6-hexanedithiol, containing two thiol groups (S-H) and pentaerythritol tetrakis(3-mercaptopropionate), containing four thiol groups per molecule. DMPA and BAPO are utilized as Norish type I photoinitiators for the generation of free radicals under exposure to UV light. Sudan Orange G is utilized as photoabsorbing agent to confine the resolution of the photopolymerization. Hydroquinone is selected as free radical scavenger to avoid premature thiol-ene polymerization and to prolong the shelf life of preceramic resins. Acetone, tert-butanol, cyclohexane and tetrahydrofuran are employed to dissolve the preceramic resins. Isopropyl alcohol and cyclohexane are employed to wash the polymerized preceramic thermosets.

For the freeze-casting process, tert-butyl alcohol (TBA) with melting point of 25-26 °C and camphene with melting point of 51-52 °C at normal pressure are utilized for dissolving preceramic polymers and to act as freezing vehicles. Graphene oxide (GO) and silica are used as fillers in the freeze-casting process. GO powder is synthesized according to an improved Hummers method as described in section 2.1.2. The hydrophilic fumed silica AEROSIL® OX 50

2.1 Synthesis, fabrication and processing of materials

nanopowder is obtained from Evonik, and the nanosized SA-SiO₂ powder is supplied by Sigma Aldrich. Their specifications are listed in Table 6.

Table 5. Materials applied in this work.

Materials	Commercial name	Chemical structure	Abbreviation	Supplier
Preceramic polymers				
Polycarbosiloxane	SILRES® H62C	Methylphenylvinylhydrogen polysiloxane	H62C	Wacker Chemie
Polycarbosiloxane	Polyramic® SPR-212	Methylvinylhydrogen polysiloxane	SPR212	Starfire Systems
Polycarbosilane	StarPCS™ SMP-10	Allylhydrido polycarbosilane	SMP10	Starfire Systems
Polycarbosilazane	Durazane® 1800	Poly(vinyl)silazane	Dura1800	Merck
Thiols				
1,6-Hexanedithiol		HS(CH ₂) ₆ SH	2T / dithiol	Sigma-Aldrich
Pentaerythritol tetrakis(3-mercaptopropionate)		(HSCH ₂ CH ₂ COOCH ₂) ₄ C	4T / tetrathiol	Sigma-Aldrich
Photoinitiators				
2,2-Dimethoxy-2-phenylacetophenone	IRGACURE® 651	C ₆ H ₅ COC(OCH ₃) ₂ C ₆ H ₅	DMPA	Sigma-Aldrich
Phenylbis(2,4,6-trimethylbenzoyl)phosphine oxide	IRGACURE® 819	[(CH ₃) ₃ C ₆ H ₂ CO] ₂ P(O)C ₆ H ₅	BAPO	Sigma-Aldrich
Photoabsorber				
2,4-Dihydroxyazobenzene	Sudan Orange G	C ₆ H ₅ N=NC ₆ H ₃ -1,3-(OH) ₂	Sudan G / G	Sigma-Aldrich
Free radical scavenger				
Benzene-1,4-diol	Hydroquinone	C ₆ H ₄ -1,4-(OH) ₂	HQ	Sigma-Aldrich
Solvents				
Acetone		CH ₃ COCH ₃	AC	AppliChem

Tetrahydrofuran		C ₄ H ₈ O	THF	Sigma-Aldrich
tert-Butyl Alcohol		(CH ₃) ₃ COH	TBA	Sigma-Aldrich
Isopropyl alcohol		CH ₃ CHOHCH ₃	IPA	Carl-Roth
Ethanol		CH ₃ CH ₂ OH	EtOH	Carl-Roth
Cyclohexane		C ₆ H ₁₂	CH	Sigma-Aldrich
Camphene		C ₁₀ H ₁₆	Cam	Sigma-Aldrich
Fillers				
Silicon dioxide	AEROSIL® OX 50	SiO ₂	OX-40	Evonik
Silicon dioxide	SA-SiO ₂	SiO ₂	SA-15	Sigma-Aldrich
Graphene oxide			GO	Home made
Chemicals for GO synthesis				
Graphite		C		LONZA
Potassium permanganate		KMnO ₄		Sigma-Aldrich
Sulfuric acid		H ₂ SO ₄		Carl-Roth
Phosphoric acid		H ₃ PO ₄		CHEMSOLUT E
Hydrogen peroxide		H ₂ O ₂		Carl-Roth
Hydrochloric acid		HCl		Carl-Roth
Hydrofluoric acid		HF		Carl-Roth

Table 6 Specifications of silica powders.

	Specific surface area [m ² /g]	Primary particle size, [nm]	Purity
AEROSIL® OX 50	50	40	≥ 99.8 %
SA-SiO ₂	200	5-15	≥ 99.5 %

2.1.2 Synthesis of graphene oxide

GO powder is synthesized according to an improved Hummers method reported by Marcano et al.¹⁰². First, a mixture of 360 ml concentrated H₂SO₄ and 40 ml concentrated HNO₃ (ratio 9:1) is prepared, followed with adding 3.0 g graphite flakes and mild mixing by magnetic stirring. 18.0 g KMNO₄ is subsequently slowly added into the reaction to avoid overheating. The reaction mixture is heated

2.1 *Synthesis, fabrication and processing of materials*

to 50 °C with a water bath and refluxed for 12 hours, followed by cooling to room temperature and dilution by slowly pouring the reaction mixture onto 600 ml ice. 5 ml H₂O₂ is added to convert residual KMnO₄ into soluble MnSO₄. The yellow color of the suspension clearly proves the oxidation of the graphite.

The suspension is then centrifuged at 6000 rpm for 3 hours, and the supernatant is neutralized and decanted away. The remaining yellow paste in the centrifuge tubes is dispersed in water by vigorous shaking, followed with centrifuging at 6000 rpm for 3 hours and decanting the supernatant. After that the material obtained is separated into a coarse soil-like part which has gathered at the bottom of the tubes and a fine gel-like surface layer on top. The fine surface layer is removed by using a spatula and dispersed in a 15 vol % aqueous HCl solution followed with centrifuging washing. Meanwhile, in order to obtain a high yield, the coarse portion (unexfoliated and partially exfoliated graphite oxide) is further washed via the aforementioned steps. The resulting HCl supernatant has to be entirely clear, otherwise GO is being washed away. After having decanted the HCl aqueous solution, ethanol is filled into the centrifuging tubes. By gently shaking the tube, GO is released and leaves the graphite oxide attached to the tube, which is decanted away. The GO-containing ethanol suspension is centrifuged (6000 rpm for 3h) for two times and the supernatant has to be clear and colorless. Finally, the GO pastes obtained after this multiple-wash process are dispersed in ethanol and vacuum dried at 55 °C, yielding 0.89 g GO powder from the initial 3.0 g graphite (yield 29.6 %).

2.1.3 Preparation of preceramic polymer resins

Preceramic polymers are mixed with other components (photoinitiator, photoabsorber, free radical scavenger) as listed in the Table 5 by magnetic stirring and ultra-sonication treatment for 2 hours. Resultant solution (free from insoluble compounds) is degassed using a vacuum pump and mixed with thiol followed by stirring to obtain a homogeneous mixture. In case organic solvents

are utilized, all components are added into the solvent and dissolved by magnetic stirring for 1 hour. For the preparation of mixed suspension and solution based freeze casting, fillers (GO or SiO₂) are first introduced to the solvent followed with ultra-sonication treatments to break down the agglomerations. Pre-ceramic polymer and other components are subsequently dissolved in the prepared suspension. An overview of pre-ceramic polymer resins prepared in this work is given in Table 7. Figure 9 displays processing routes applied in the Chapters 3-5; the detailed description of the preparation of the specific samples is given in the corresponding chapters.

2.1.4 Fabrication of thermosets

Assisted with thiol-ene click chemistry, the pre-ceramic polymers are processed into thermosets via developed stereolithographic and freeze casting approaches, which is described in detail in Chapter 4 and Chapter 5, respectively.

2.1.5 Thermal transformation from thermosets to ceramics

The ceramic samples are synthesized by the pyrolysis of the corresponding thermosets.

The fabricated thermosets are placed on an alumina plate which is covered with a thin graphite sheet and transferred to home-build furnace (incornel tube inserted inside an NABER oven) for the pyrolysis. The furnace is evacuated then flushed with pure nitrogen gas for 3 times. For the parts produced with stereolithography, heating profile A is utilized, while heating profile B is employed for freeze cast parts.

Heating profile A: from room temperature (r.t.) to 250 °C with a ramp rate of 60 °C/hour, holding for 2 hours at 250 °C, from 250 °C to 1100 °C with a ramp rate of 40 °C /hour, holding for 2

2.1 Synthesis, fabrication and processing of materials

hours at 1100 °C, cooling from 1100 °C to r.t. with a ramp rate of 36 °C/hour.

Heating profile B: from room temperature (r.t.) to 250 °C with a ramp rate of 60 °C /hour, holding for 2 hours at 250 °C, from 250 °C to 1100 °C with a ramp rate of 60 °C /hour, holding for 2 hours at 1100 °C, cooling from 1100 °C to r.t. with a ramp rate of 180 °C /hour.

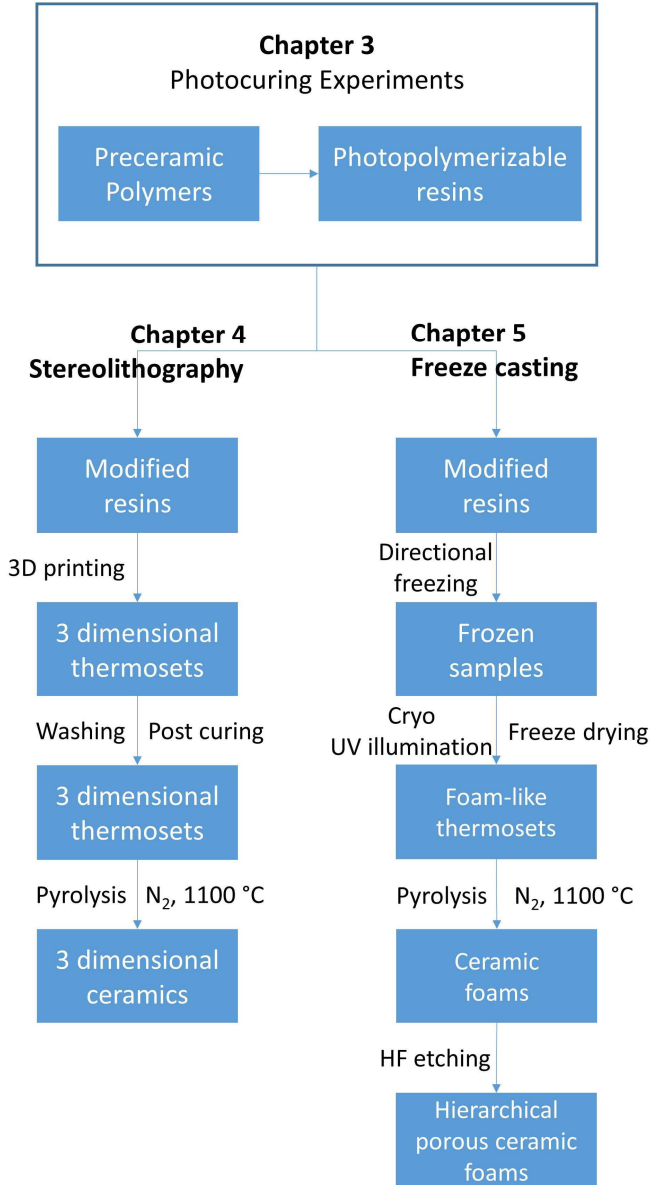


Figure 9. General processing routes applied in this thesis, including photocuring experiments (chapter 3), stereolithography (chapter 4) and freeze casting (chapter 5).

2.1 Synthesis, fabrication and processing of materials

Table 7. Formulations overview of preceramic polymer based resins. For the preparation of organogels 1-3, S1 are acetone, TBA, THF and cyclohexane, while S2 are THF, cyclohexane. Numbers in the table represent weight ratios of the components. For example, thermoset 1 resin is prepared by mixing H62C, 2T, DMPA in a weight ratio of 100:10:1.

Sample	Preceramic polymers				Additives for thiol-ene click chemistry					Solvents		Fillers	
	H62C	SPR212	Dura18	SMP10	2T	4T	BAPO	DMPA	Sudan G	Type	amount	type	amount
Curing													
Thermoset1	100				10			1					
Thermoset2		100			15			1					
Thermoset3			100		15			1					
Thermoset4				100	8			1					
Thermoset5	100					16		1					
Organogel1,	33				3.3			0.33		S1	67		
Organogel2		33			5			0.33		S1	67		
Organogel3			33		5			0.33		S2	67		
	Preceramic polymers				Additives for thiol-ene click chemistry					Solvents		Fillers	
Stereolithography	H62C	SPR212	Dura18	SMP10	2T	4T	BAPO	DMPA	Sudan G	Type	amount	type	amount
Ptest1		100			20		1						
Ptest2		100			20		1.5						
Catest1		100			20		1.5		0.1				
Catest2		100			20		1.5		0.05				
Catest3				100	8		1						
Printing 1		100			20		1.5		0.05				
Printing 2			100		20		1.5		0.05				
Printing 3				100	8		1						
Freeze casting													
HG0	20				2			0.2		TBA	80		
HG1	20				2			0.2		TBA	80	GO	0.05
HG2	20				2			0.2		TBA	80	GO	0.1
TBA30	15	15			4.5			0.3		TBA	70		
TBA20	15	15			4.5			0.3		TBA	120		
Cam30	15	15			4.5			0.3		Cam	70		
TBA30-40	15	15			4.5			0.3		TBA	70	OX-40	7.5
TBA30-15	15	15			4.5			0.3		TBA	70	SA-15	7.5

2.2 Characterization methods

2.2.1 Radiography and Tomography

X-ray imaging (radiography) is performed using a microfocus X-ray source and a flat panel detector (Hamamatsu, Japan) with an area of $\sim 120 \times 120 \text{ mm}^2$ and a pixel size of $50 \mu\text{m}$ as reported in ¹⁰³. Sample magnification is set between 6 and 10, depending on the size of the sample, resulting in an acquired projection with a pixel size between 5 and $10 \mu\text{m}$. For the tomographic acquisition 1000 projections are taken over a sample rotation of 360° .

For the in-situ radiography investigations of the drying of freeze cast samples, samples in frozen state are placed in an aluminum chamber, which is sealed and connected with a vacuum pump, thus allowing the sublimation of frozen TBA crystals. During the drying process, radiography images are taken every 5 seconds with an acquisition time of 2 seconds until the sublimation is complete.

2.2.2 Scanning Electron Microscopy (SEM) and Energy-Dispersive X-ray Spectroscopy (EDX)

SEM micrographs and element mapping are obtained using ZEISS Gemini SEM500 NanoVP and ZEISS Gemini LEO 1530 FEG-SEM with EDX system by Thermo Fisher Scientific. The additively manufactured samples are coated with a conductive gold or carbon layer prior to investigation. For cross sectional observation, the freeze cast samples are cut with a diamond blade followed by polishing. An acceleration voltage of 10 kV is applied.

2.2 Characterization methods

2.2.3 Field Emission-Electron Probe Microanalysis (FE-EMPA)

Electron Probe Microanalyzer (JEOL JXA-8530F) is utilized to determine the chemical compositions. First, backscattered electron images are made from the cross-section surface, showing the atomic number contrast. Then, element mappings are made, showing the distribution of carbon, silicon, sulfur and oxygen, with scanned area being 15×11.25 microns, measured with a resolution of 600×450 points (step size: 25 nm) and a dwell time of 150 ms for each point. An acceleration voltage of 15 kV and a beam current of 10 nA are used.

The freeze cast samples are manually cut, followed with embedding in resin, grinding and final polishing with $0.05 \mu\text{m}$ alumina suspension. Subsequently a conductive carbon layer (thickness: ~ 10 nm) is deposited on the cross-section surface.

2.2.4 Transmission Electron Microscopy (TEM) and Energy-Dispersive X-ray Spectroscopy (EDX)

TEM characterizations are performed on a TECNAI G220 S-TWIN (FEI, Oregon, USA) with LaB₆ electron gun, operated at 200 kV. A Gatan MS794 P CCD camera and Digital Micrograph software package are used for image recording and evaluation. An EDX (EDAX) r-TEM SUTW detector is coupled to the TEM for the element mapping investigation. Samples for TEM characterization are prepared as follows, the powders are crushed and dispersed in ethanol, then applied on a holey carbon film, supported on a 300 mesh Cu-TEM-grid, followed with drying in air at 40 °C.

2.2.5 Nuclear Magnetic Resonance (NMR) Spectroscopy

Solid-state ^{29}Si NMR spectra are recorded with a Avance 400 MHz spectrometer (Bruker, Germany) operating at 79.44 MHz to characterize the chemical environment of silicon in polysiloxane derived SiOC ceramics. Samples are prepared by grinding the SiOC monolith into fine powders.

2.2.6 Rheology characterization

The dynamic rheological properties of the preceramic polymers are studied with an Anton Paar MCR 301 viscometer (Anton Paar GmbH, Graz, Austria) with plate-plate measurement system at a shear-rate ramp increasing linearly from 5 s^{-1} to 100 s^{-1} and then back to 5 s^{-1} at $25\text{ }^{\circ}\text{C}$.

2.2.7 X-Ray Diffraction (XRD)

X-ray powder diffraction patterns are collected on ground powders in a D8 (Bruker Corporation, USA) with $\text{CoK}\alpha$ radiation (wavelength 0.178 nm) in Bragg-Brentano geometry with maximum stepsize of 0.02° from 10 to 90° 2 Theta . Diffraction patterns are analyzed with the Diffrac-Plus/EVA software from Bruker AXS.

2.2.8 X-Ray Photoelectron Spectroscopy (XPS)

The XPS measurements are measured on K-Alpha TM + X-ray Photoelectron Spectrometer (XPS) System (Thermo Scientific), with Hemispheric 180° dual-focus analyzer with 128-channel detector. The X-ray monochromator is Micro focused $\text{Al-K}\alpha$ radiation. For the measurement, the PDCs monoliths are ground into fine powders and are directly loaded on the sample holder. The data is collected with

2.2 Characterization methods

X-ray spot size of 400 μm , 20 scans for survey, and 50 scans for regions in vacuum (10⁻⁷ mbar).

2.2.9 Fourier Transform Infrared (FTIR) Spectroscopy

FTIR spectra are measured in Attenuated Total Reflection (ATR) mode carried out in an Equinox 55 (Bruker, Germany) in the range of 4000 – 500 cm^{-1} to characterize the free radical initiated thiol-ene polymerization as well as the polymer to ceramic transformation. The thermosets are crushed into fine powders and directly loaded onto the ATR module, while pyrolyzed ceramics are ground into fine powders and loaded into the ATR module.

2.2.10 Ultraviolet–Visible (UV-Vis) spectroscopy

UV-vis spectra are measured and recorded using Perkin Elmer Lambda 900 UV-visible spectrometer from 800 nm to 250 nm in transmittance mode. Measuring samples are prepared by dissolving in organic solvents (isopropyl alcohol and THF) as dilution agent.

2.2.11 Nitrogen physisorption

The nitrogen sorption measurements are carried out on a Quantachrome Quadrasorb SI instrument. The as prepared ceramic cylinders are directly degassed at 150 °C for 12 h before actual measurement. The specific surface area is calculated by using Brunauer-Emmett-Teller (BET) calculations¹⁰⁴ in P/P_0 from 0.003 to 0.05 and the pore sized distribution plot is obtained from the adsorption branch of isotherms by the QSDFT model. Total pore volumes are calculated based on the volume adsorbed at P/P_0 of ~ 0.995 . The micropore surface areas are evaluated through the t-plot method.

2.2.12 Simultaneous Thermal Analysis coupled with Mass Spectrometry (STA- MS)

The polymer to ceramic conversion is investigated by using thermal gravimetry/differential thermal analysis (TG/DTA) performed on a STA 409 PC LUXX (Netzsch, Germany) coupled with a mass spectrometer OMNi Star GSD 320 (Pfeiffer Vacuum, Germany) with a heating rate of 10 °C/min under nitrogen atmosphere.

2.2.13 Differential Scanning Calorimetry (DSC) under UV exposure

The UV-DSC measurements are conducted by a DSC Q2000 (TA instruments) coupled with high pressure 200 W mercury vapor lamp, equipped with a 320-500 nm bandpass filter. The preceramic polymer resins are freshly prepared according to compositions of thermoset 1-5 as seen in Table 7 and stored in brown glass vials, and subsequently deposited in open Al pan and exposed to UV light with an intensity of 100 mW/cm² for 5 minutes. The heat flow during curing at defined radiation intensity is measured and recorded.

2.2.14 Nanoindentation

The nanoindentation characterization is conducted in TI 950 TriboIndenter (Hysitron Inc., USA). For that, as-prepared SiOC honeycomb is embedded in epoxy resin and polished to a 1 μm finish, and indented with a tetrahedral Berkovich diamond tip at a load of 10 mN and a load rate of 50 μN/s. The elastic modulus and hardness are calculated by evaluating the slope of the curve dP/dh upon the elastic unloading with 200 indents.

2.2 Characterization methods

2.2.15 Compressive Strength measurements

The compressive strength of the SiOC honeycombs is determined using a universal test machine RetroLine (Zwick/Roell, Germany) with a cross-head speed of 0.1 mm/min. For this test, SiOC honeycombs are first grounded to achieve relatively parallel surfaces and a thickness of 2.78 mm. Then they are sandwiched between two steel face sheets with epoxy glue to prevent horizontal movement and to avoid damaging the pressing anvil.

3 Thiol-ene click chemistry with Si-containing preceramic polymers

3.1 Photocuring experiments

The thiol-ene click reaction is a reaction between the –SH group of a thiol and the carbon double bond (C=C) in an alkene. This reaction is one of the most widely-investigated photoinduced cross-linking reactions of organic materials towards polymer network formation. The thiol-ene click reaction is characterized by high reaction rate, high conversion, excellent tolerance to solvent environment, low susceptibility to oxygen inhibition and less volume shrinkage compared to acrylate or methacrylate systems. One of the biggest advantages of the thiol-ene click reaction is the abundance of thiol-containing monomers and its universal applicability for all alkenes, especially electron-rich ones¹⁰⁵. The reaction rate of thiol-ene click reaction decreases in this order: norbornene \geq vinyl silanedi-amine $>$ allyl ether \geq vinyl ether $>$ fumarate $>$ propene $>$ maleimide $>$ methacrylate $>$ crotonate $>$ styrene $>$ acrylonitrile $>$ butadiene; it is noticeable that vinyl-silanedi-amine ($\text{CH}_2=\text{CH}-\text{Si}(\text{NH}_2)_2$) displays the second highest reaction rate¹⁰⁶. Therefore, it is reasonable to expect that the thiol-ene click reaction can be an efficient tool to photopolymerize Si-containing preceramic polymers with side groups containing carbon double bonds.

To demonstrate the applicability of the photoinduced thiol-ene reactions with different classes of preceramic polymers, several initial photocuring experiments are conducted. The resins are prepared according to Section 2.2. To initiate the thiol-ene polymerization the resultant preceramic resins are placed into transparent glass vials and are exposed to UV light using a UV illuminator (UV-Belichtungsgerät 1, isel, proMA Technologie

3.1 Photocuring experiments

GmbH) for 5 min. Table 8 lists the specifications of utilized UV illuminator.

Table 8. Specifications of UV illuminator.

Power	4×8 W
Mounting area	160×250 mm ²
Energy density	80 mW/cm ²
UV wavelength	350 – 400 nm

Photoinitiators act as free radical generators under light illumination and when in the vicinity of photopolymers initiate the thiol-ene click reactions. To select suitable photoinitiators for the light source applied, UV-Vis is performed on polysiloxane H62C as a case material, both pure and mixed with BAPA and DMPA (Figure 10).

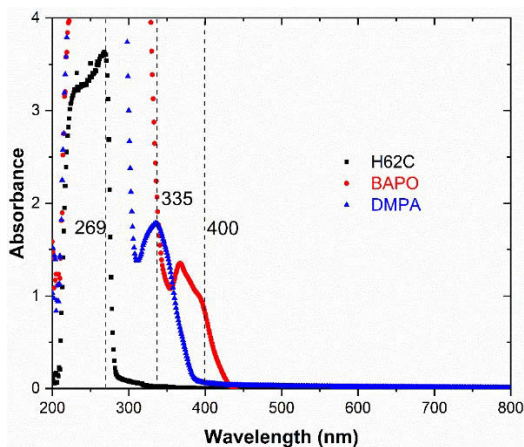


Figure 10. UV-Vis absorption spectra of H62C (black), H62C blended with DMPA (blue) and H62C mixed with BAPO (red).

Pure H62C does not demonstrate any noticeable absorption above 300 nm. Its absorption maximum is located around 269 nm. H62C mixed with DMPA in a 1:100 weight ratio begins to absorb below 400 nm and demonstrate a first absorption peak around 335 nm. The utilization of BAPO further expands the absorption

spectrum above 400 nm, which is in the violet-blue region of visible light. Therefore, the application of two different photoinitiators allows for employing light sources with different wavelength emissions, from near-UV to visible light. For instance, for our purpose conventional UV lamps emitting ultraviolet A light within 350 – 400 nm and commercial projector emitting in the near UV range can be used to cure the polymer system mixed with DMPA and BAPO, respectively.

3.2 Photoinitiated cross-linking of preceramic polymers

In this work four commercially-available preceramic polymers are investigated (see Chapter 2). The structural formulas of Durazane 1800 and SMP 10 are well-known and presented in Figure 11. As for polysiloxane Silres H62C, whose composition provided by the producer ¹⁰⁷ is known to be $\text{RSiO}_{1.5}$, in which $\text{R} = [(\text{C}_6\text{H}_5)_{2.8}(\text{CH}_3)_{1.5}(\text{CH}_2=\text{CH})(\text{H})]$. However, there is not enough information to reveal the exact chemical structure of the polysiloxanes SPR212. Nonetheless, Fourier-Transform Infrared Spectroscopy (FTIR) is utilized to characterize the preceramic polymers employed in this work. The results of this investigation are presented in Table 9.

Table 9. Typical vibration frequencies of preceramic polymer utilized in this thesis.

Group	Absorption band, cm^{-1}			
	SPR212	Silres H62C	SMP10	Dura 1800
Si-O-Si	1020, 1076	1025, 1131	~	~
Si-CH ₂ -Si	~	~	1038	~
Si-C	~	~	833	~
Si-CH ₃	1260	1252	750	1252
Si-N-Si	~	~	~	876
SiN-H	~	~	~	1160
Si-vinyl	1407, 1600	1407, 1594	~	1402, 1592
Si-phenyl	~	1429, 1594	~	~

3.2 Photoinitiated cross-linking of preceramic polymers

Si-allyl	~	~	1629	~
Si-H	2161	2170	2121	2118
N-H	~	~	~	3380
C-H	2964	2957	2921	2956

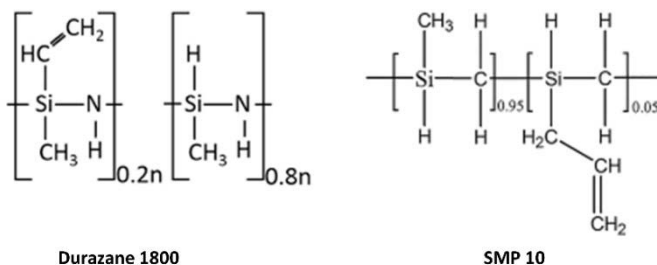


Figure 11. Structural formulae of Durazane 1800 and SMP10.

Figure 12 shows the FTIR spectra of utilized preceramic polymers, in which the absorption bands (which determine the class of preceramic polymer) are marked red, while the alkene side groups (which are responsible for reacting with thiol monomers) are marked in blue. The utilized materials represent three classes of Si-containing preceramic polymers, namely polysiloxanes, polycarbosilanes and polycarbosilazanes, and they all possess vinyl or allyl side groups. Upon pyrolysis, these preceramic polymers transform into polymer-derived silicon oxycarbide, silicon carbide and silicon carbonitride ceramics, respectively. A possible incorporation of oxygen and sulfur in polymer-derived ceramics cannot be excluded due to the intended click-reaction with thiols. Dithiol possesses two terminated thiol (-SH) groups and does not contain oxygen and nitrogen. Tertathiol contains four terminal thiol groups (4T) and a significant amount of oxygen.

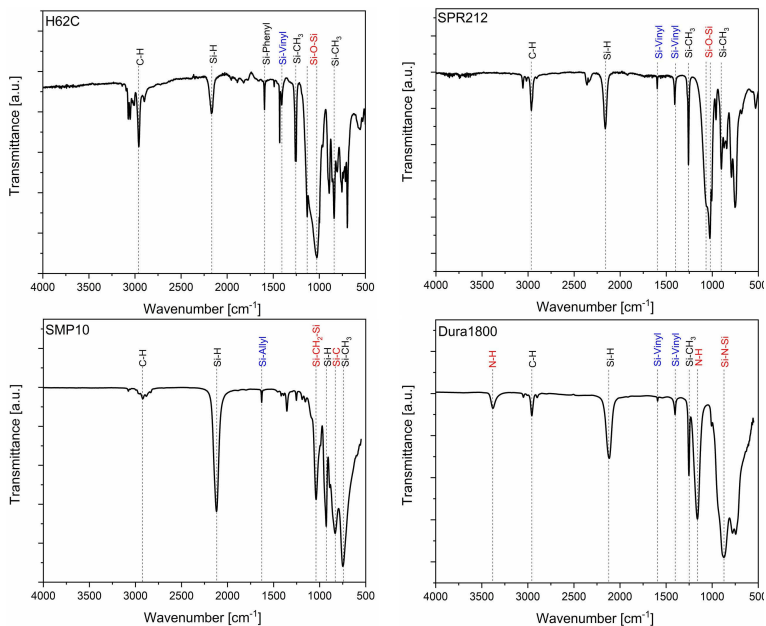


Figure 12. ATR-FTIR spectra of polysiloxanes H62C and SPR212, polycarbosilane SMP10 and polycarbosilazane Durazane 1800 employed in this work. Absorption bands, which determine the class of preceramic polymers, are marked as red, while the alkene side groups are marked in blue.

Preceramic polymers H62C, SPR212, SMP10 and Durazane1800 with vinyl side groups are photopolymerized with dithiol using DMPA as photoinitiator. The compositions of preceramic resins are stated in chapter 2 Table 7 as thermosets 1-4. The photopolymerization of these preceramic polymers based on thiol-ene click chemistry are all successful. They demonstrate significantly improved efficiency; as liquid preceramic polymers are converted into rubber-like gels within one minute under low-intensity UV irradiation conditions. FTIR investigations of these systems are conducted before and after UV irradiation to evaluate the degree of photopolymerization by monitoring the intensity of the bands associated with vinyl groups at 1407 cm^{-1} ($=\text{CH}_2$ scissoring) and 1597 cm^{-1} ($\text{C}=\text{C}$ stretch) and with thiol groups at 2570 cm^{-1} . Figure 13

3.2 Photoinitiated cross-linking of preceramic polymers

displays the ATR-F^TIR spectra of the investigated resins before and after the thiol-ene assisted photopolymerization. Because of the low concentration of thiols and relatively weak absorption associated with the S-H groups, the thiol peaks are not observed in the FTIR spectra even before the UV irradiation. Nonetheless, the significant decrease of the intensity of the vinyl absorption bands in the FTIR spectra as well as the elimination of the strong thiol odor indicate a successful thiol-ene click reaction in all polymers, as both vinyl and thiol groups are consumed during the photopolymerization.

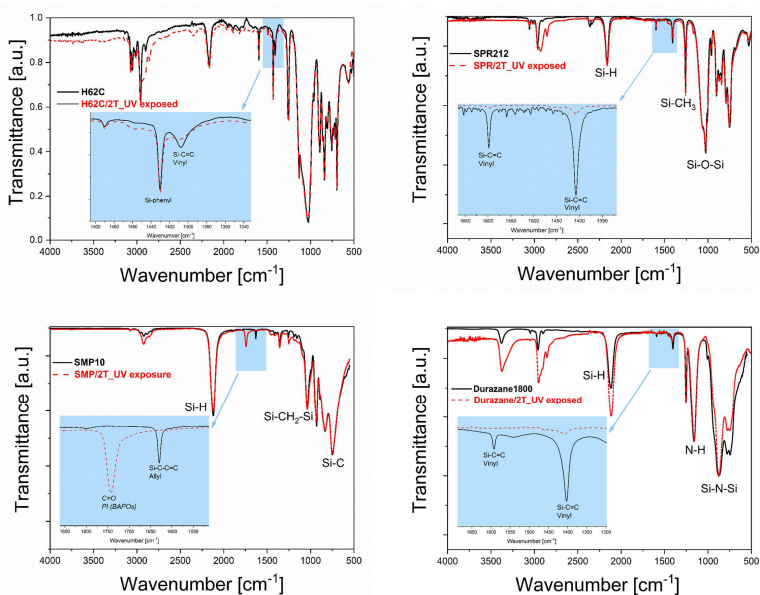


Figure 13. ATR-F^TIR spectra of preceramic resins before curing (black) and after curing (red): (A) polysiloxane H62C, (B) polysiloxane SPR212, (C) polycarbosiiane SMP10 and (D) polycarbosiilazane Dura18. The thiol-ene click polymerization is confirmed by the strong reduction of the absorption bands of the vinyl groups that are displayed in the inset.

During the photopolymerization process of preceramic resins, incident light is primarily absorbed by the photoinitiator molecules, except with polycarbosiiane SMP10, which itself absorbs photons as

well (Figure 14). Higher penetration depth of incident light into the liquid resin and the fabrication of large (thicker) structures are facilitated by low amount of photoinitiators. As the photoinduced thiol-ene click reaction is triggered by low amount of photoinitiators (even less than 0.1 wt. %) and the preceramic resins with H62C, SPR212, and Dura1800 are transparent (Figure 14), the fabrication of bulk thermoset structures with high aspect ratios and thick walls can be achieved in the thiol-ene click reaction supported systems. In contrast, the conventional photolithography of preceramic polymers is achieved through free radical initiated hydrosilylation, which requires high amount of photoinitiators (up to 5 wt.%) and deep UV exposure, leading to resultant curing depths of generally less than 1 mm, and thus only allowing for the fabrication of 2D structures.

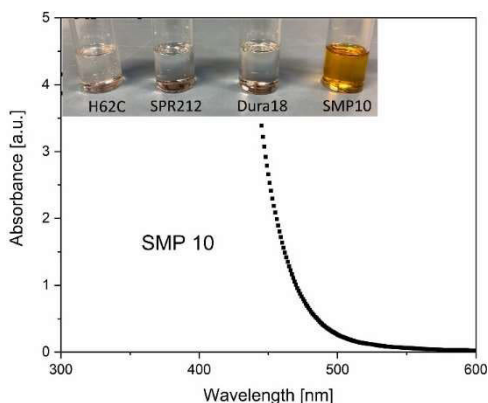


Figure 14. UV-vis absorption spectrum of SMP10 displaying the absorption starting below 550 nm. Inset shows the optical images of employed preceramic polymers.

In this work, substantial improvements of the curing depth are achieved as shown in Figure 15, i.e., 10 mm-thick thermoset samples are fabricated from H62C, SPR212 and Dura 18 –resins with DMPA as photoinitiator in a 1:100 weight ratio to the PCP under low intensity UVA illumination for only 1 minute. Even higher curing depth could be obtainable by further decreasing the photoinitiator content and prolonging the UV illumination time. In contrast, the

3.2 Photoinitiated cross-linking of preceramic polymers

photopolymerization of SMP10 resin allows only for a fabrication of a thin layer of cross-linked polymer under same conditions, further increase in the illumination time does not result in significantly increased curing depth. Because the SMP 10 preceramic polymer has an intrinsic yellowish color, it acts as a strong photoabsorber (as observed in the UV-Vis spectrum in Figure 14), and thereby impedes the penetration of incident UV light. As a result, the photopolymerization is restricted to only the surface layer of the resin.

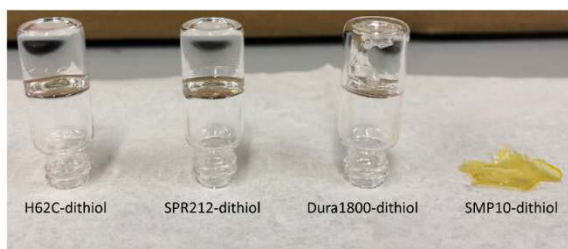


Figure 15. High penetration depth of incident light in H62C, SPR212 and Dura18-2T resins allows for the fabrication of bulk thermoset specimens with thickness of about 10 mm while SMP10-2T resin demonstrates significantly reduced curing depth due to its intrinsic yellowish color.

To test the applicability of thiol-ene reaction regarding various chemical environments, polar (acetone, THF, TBA) and non-polar (cyclohexane) solvents are added to dissolve the preceramic polymer-dithiol mixture, and the whole mixture is stirred under mild conditions for 10 min using magnetic stirring. The amount of organic solvents is kept constant at 67 wt % (see Table 7). Resultant transparent solutions are placed into cylindrical silicone mold and illuminated with UV lamp to start the photopolymerization. The employed organic solvents are shown in Table 10.

Table 10. Photocuring of preceramic polymer-dithiol solutions. Dura1800 was only dissolvable in THF and cyclohexane, because tert-butanol and acetone react with the polysilazane.

	H62C-2T	SPR212-2T	Dura18-2T
Acetone	X	X	
THF	X	X	X
TBA	X	X	
Cyclohexane	X	X	X

Since the SMP 10 resin undergoes a slow photopolymerization process and has low curing depth, H62C, SPR212 and Dura18 dithiol resins are further investigated to study their versatility and adaptability. The thiol-ene polymerization is called as a type of click reaction, because it fulfills several criteria, one of them is that the reaction should be not influenced by employing additional solvents in the resin.

Figure 16 illustrates the thermosets fabricated from preceramic resins dissolved in organic solvents. After the UV illumination, the SPR212 and Dura1800 solution turned into transparent and self-standing organogels, which are composed of liquid organic solvents dispersed within the three-dimensional, cross-linked network of the preceramic polymers. These organogels demonstrated typical gel-like properties, including free standing, no steady-state flow, and very high elasticity. In contrast, the photopolymerized H62C solution demonstrates very weak mechanical integrity, as they do not show a defined geometry and could not free standing. The underlying reason is based on the less amount of reactive sites (vinyl groups) presented in H62C, which results in the polymerization degree not reaching the critical gel point. As a conclusion, the thiol-ene click reaction based on different preceramic polymers exhibits excellent versatility with the presence of solvents by showing unaltered photopolymerization behavior. The results could have huge implications in the production of PDCs-based membranes or coatings, and resultant organogels could be utilized for the preparation of highly porous ceramic monoliths.

3.2 Photoinitiated cross-linking of preceramic polymers

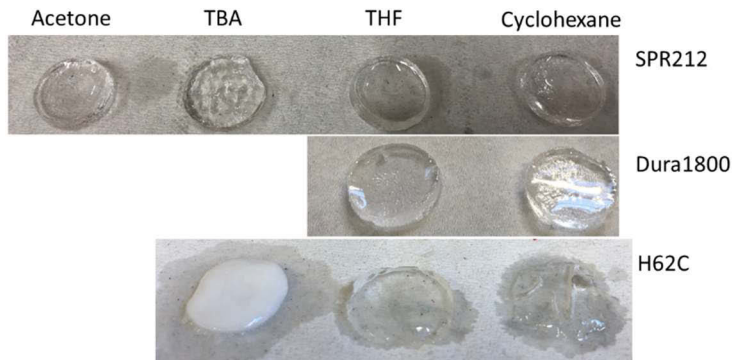


Figure 16. Gel formation in SPR212, Dura1800 and H62C resins dissolved in different organic solvents (from left to right, acetone, tert-butanol, tetrahydrofuran and cyclohexane) with a weight ratio of 1:2 (PCPs to solvents).

3.3 Energetics and kinetics of thiol-ene click chemistry

To study the kinetics of thiol-ene click reaction, in-situ real-time differential scanning calorimetry (DSC) under UV irradiation is conducted. It allows for the investigation of the curing efficiencies in preceramic polymer resins. As described in Chapter 2, dithiol is mixed with SPR212 and Durazane 1800 in a weight ratio of 15:100, and for SMP10 and H62C - in a weight ratio of 10:100 due to the lower amount of vinyl groups present in these two polymers. The H62C, SPR212 Durazane1800 resins displays very strong and sharp exothermic peaks immediately after being exposed to UV light, which indicates a fast thiol-ene click reaction for these polymer systems (see Figure 17). The measured differential heat flow, which is a real-time representation of the cross-linking rate, increases to a maximum within ~ 1 s of UV illumination. The heat flow then quickly decreases to zero due to the consumption of dithiol and alkene and to the growing 3D interconnected polymeric network, which strongly degrades the diffusion rate of reacting species and turns the reaction from thermodynamically- to diffusion-controlled regime. In contrast,

the cross-linking rate of thiol-ene click reaction with polycarbosilane SMP10 is significantly lower and is accompanied also by a slower reduction of the heat flow. The magnified UV-DSC plot in Figure 17b visualizes that it takes around 4.5 s for the SMP10-2T resin to reach the peak polymerization rate, the maximum intensity of the evolved heat flow is only one fourth of the peak values of SPR212 and Dura1800 based resins.

This is due to the strong absorbance of SMP10 polymer in the blue-violet region of the visible spectrum, as evident by its intrinsic orange color as well as its absorbance in the UV-Vis spectra shown in Figure 14. The incident UV light is thus being absorbed both by the photoinitiator and the polymer itself leading to a much slower polymerization rate as well as a decreased curing depth of SMP10-2T resins, which will be shown in the later section.

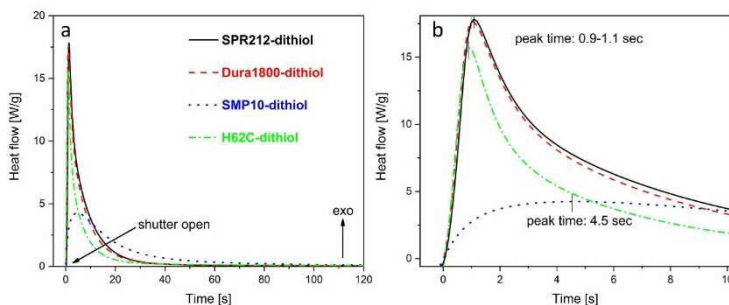


Figure 17. (a) Results of the in-situ differential scanning calorimetric characterization (UV-DSC) of preceramic resins with dithiol. (b) Magnified UV-DSC plots demonstrate the lower reaction rate of SMP10 than other preceramic polymers (SPR212, H62C and Dura1800).

The area under the heat flow curves reflects the total reaction heat evolved during photopolymerization of the preceramic polymer-2T systems. The reaction heat, which is obtained by integrating the heat flow curves from 0 to 300 s, are listed in Table 11. The measured reaction heat of SPR212 and Dura1800 are approximately the same, since they consist of similar amount of dithiol and vinyl groups (note that both SPR212 and Dura1800 are mixed with dithiol in a weight

3.2 Energetics and kinetics

ratio of 100:15). The reaction heat of the H62C resin is slightly lower since the weight ratio of H62C to dithiol is set 100:10.

Surprisingly, the SMP10 resin demonstrates a specific reaction heat comparable with that of the SPR212 resin, despite containing far fewer vinyl groups compared to SPR212 and Durazane1800, which should have led to a lower amount of photoinduced thiol-ene cross-linking and less reaction heat. The specific reaction enthalpies of each preceramic polymer-2T resin can be calculated assuming full consumption of the added dithiol using the following equation:

$$\Delta H = \Delta H^o \times \frac{\omega_{2T}}{M_{2T}} \times 2 \quad \text{Equation 3}$$

where ΔH^o is the theoretical molar reaction enthalpy of thiol-ene click reaction, being -79 kJ/mol according to the report by Northrop and Coffey¹⁰⁶, ΔH is the calculated reaction enthalpy of 1 g resin mixture, ω_{2T} is the mass fraction of dithiol in the different resins (13 wt.% in SPR212 and Durazane1800 resins and 9.1 wt% in H62C and SMP10 resins), M_{2T} is the molecular weight of dithiol multiplied by 2 due to two thiol groups being present in one molecule of dithiol.

Table 11. Measured reaction heat and calculated reaction enthalpy and conversion efficiency of thiol-ene click reaction between dithiol and preceramic polymers.

	SPR212	Dura1800	H62C	SMP10
Measured reaction heat [J/g]	118.0	112.8	84.9	113.3
Calculated reaction enthalpy [J/g]	-137.5	-137.5	-95.9	-95.9
Reaction yield [%]	85.8	82.0	88.5	118.1

In Table 11 the measured reaction heat obtained from the UV-DSC measurements of the photopolymer resins are compared with

the absolute value of reaction enthalpy calculated according to Equation 3. The smaller measured reaction heat for SPR212, Dura1800 and H62C resin compared to that calculated value by assuming complete consumption of dithiol in the thiol-ene click reaction indicate an incomplete photopolymerization reaction, which in turn indicates the presence of residual dithiol and vinyl side groups remaining in the photopolymerized thermosets. Indeed, the FTIR spectra of UV cured resins display low intense absorption bands of vinyl groups as well. Free radical polymerization requires sufficient mobility of reacting species to facilitate the reaction. Instead, preceramic polymer with high molecular weight, which has less mobility compared to monomers, is utilized in this thesis to conduct the thiol-ene reaction. With the propagation of photopolymerization, the diffusion process is further hindered, as the polymer network becomes more and more rigid. Therefore, the reaction yield, calculated through dividing the measured reaction heat with calculated reaction heat, is below 100 %, meaning incomplete consumption of thiol and alkene functional groups.

For the SMP10 resin, the measured reaction heat surpasses the calculated value, which leads to a thiol conversion greater than 100%. The reason for that could be an additional photopolymerization route related to dehydrocoupling reaction between two silane (Si-H) bonds. Such dehydrocoupling reactions have been reported previously in SMP10 polymer under UV illumination in the presence of platinum-based catalysts, the Si-Si bond formed in this dehydrocoupling reaction was confirmed by $^{29}\text{Si-NMR}$ ⁸⁴. In this work, the DSC is equipped with a wide range UV light source with wavelengths ranging from 320 nm to 500 nm and SMP10 polymer itself demonstrates significant absorbance with UV illumination. Hence it is probable that during the UV-DSC measurement SMP10 polymer absorbs high energy photons which lead to the dissociation of Si-H bonds and the formation of Si-Si bonds via dehydrocoupling. As a result, the measured reaction heat was higher than the reaction heat that only originates from the thiol-ene click reaction.

3.2 Energetics and kinetics

The normalized integral of the heat flow curves can be further utilized to reveal the conversion degree of the thiol-ene click cross-linking for different preceramic polymers. It shows the fast reaction kinetics of preceramic polymer-based thiol-ene click reaction, as more than 60 % of conversion is reached with SPR212, H62C and Dura1800 dithiol resin mixture after 10 s of UV illumination. In contrast, the SMP10 resin requires 23 s of UV irradiation to achieve 60 % conversion (see Figure 18)

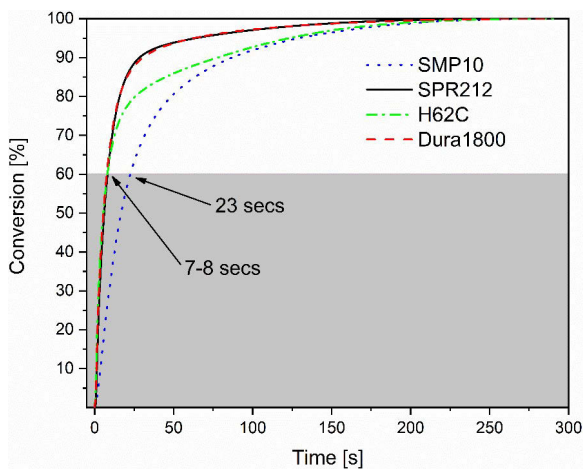


Figure 18. The conversion of thiol-ene click reaction of preceramic polymers with dithiol obtained by integration of the heat flow curves and subsequent normalization.

Summarizing, these results demonstrate that the thiol-ene click reaction between dithiol and preceramic polymers with side vinyl groups is an effective tool towards fast and efficient photoinitiated cross-linking, which is beneficial and necessary in various fabrication methods, including additive manufacturing and freeze casting of liquid preceramic polymers.

Due to the two times higher amount of thiol groups in tetrathiol in comparison to dithiol, its utilization in the preceramic resins is expected to result in a higher cross-linking degree in the thermoset network which would enhance the mechanical strength in

the resulting thermoset. However, the improvement in mechanical stability of fabricated thermosets is not observed in this work and the utilization of tetrathiol instead of dithiol for the preparation of preceramic photopolymer does not improve the photopolymerization process, probably due to the reasons given below. One reason for that could be the limited solubility of tetrathiol in the preceramic polymers under study. In contrast to dithiol, which form clear solutions when mixed with preceramic polymers, tetrathiol is not soluble in SPR212 at all, and an unstable emulsion (similar to oil in water) is formed instead. Mixing tetrathiol with H62C results in a stable milky-like emulsion with significantly increased viscosity, as both H62C and tetrathiol are highly viscous liquids with viscosities of 1200 and 500 mPa·s at room temperature, respectively, while hexane dithiol has an extremely low viscosity of 0.9 mPa·s. The curing behavior of H62C-4T resin, which contains the same amount of thiol groups like H62C-2T resin, reveals different reaction kinetics in comparison to H62C-2T resin as seen in Figure 19.

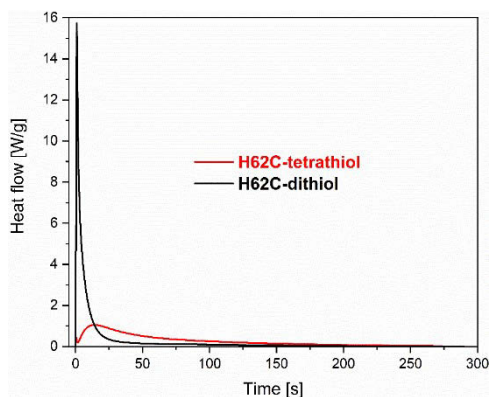


Figure 19. Results of the in-situ differential scanning calorimetric characterization (UV-DSC) of H62C-4T and H62C-2T resins, demonstrate the significantly reduced heat flow maximum due to tetrathiol.

The heat flow maximum is reduced for more than one order of magnitude (from 15.7 W/g to 1.1 W/g) for H62C-4T in

3.2 Energetics and kinetics

comparison to H62C-2T resins, while the required time to reach peak heat flow is increased to 14 s. These results indicate that the thiol-ene click reaction is hindered in the resin with 4T thiol. The reasons for that can be threefold. Firstly, the penetration depth of the incident UV is reduced in the milky/cloudy 4T-H62C resin. Secondly, since the H62C polymer does not dissolve as well with tetrathiol as it does with dithiol, the resulting reaction species are not uniformly distributed to allow optimal reaction. Thirdly, the photopolymerization process in the H62C-4T resin is less efficient due to the significantly increased viscosity of this resin compared to the H62C-2T resin. As in reaction systems with high viscosity, the diffusion process of the reacting species is hampered, thus they collide less frequently per unit time and lead to decreased reaction rates.

Despite the low reaction rate, the slowly reducing heat flow of H62C-4T under UV illumination revealed the photopolymerization is still occurring until 200 s, while the thiol-ene reaction of H62C-2T resins terminates after 50 s. The resultant overall reaction heat of H62C-4T resin after 5 min of UV irradiation is merely decreased to a small extent (73.5 J/g compared to 84.9 J/g in the H62C-2T system), demonstrating the majority of thiols groups and alkene functionalities were consumed. As a conclusion, the thiol-ene polymerization efficiency is reduced when using 4T instead of 2T, while the overall reaction is still effective under long-time UV exposure.

Considering the significantly reduced photopolymerization rate as well as the possible oxygen contamination in oxygen-free preceramic polymers (Durazane1800 and SMP10), tetrathiol appeared as being not suitable for thiol-ene click reaction with the preceramic polymers under study. Therefore dithiol was chosen for the preparation of preceramic resins due to its low viscosity and good solubility in various preceramic polymers as well as fast photopolymerization reaction.

3.4 Summary

In this chapter, we have extensively studied the photopolymerization of alkene groups containing preceramic polymers with multifunctional thiol monomers. It is demonstrated that thiol-ene click reaction is an efficient tool to cross-link preceramic polymer with different Si-X bonding, including polycarbosiloxane, polycarbosilane and polycarbosilazane. The photoinduced step-growth thiol-ene polymerization rate is significantly higher than the rate of conventional photoinduced vinyl addition in preceramic polymers. The fast reaction rate represents a great advantage in many shaping methods to fabricate PDCs, e.g. in the fabrication of micro-electro-mechanical-systems and additive manufacturing, which will be presented in the following Chapter 4. Since a very low concentration of photoinitiator is required for the initiation of thiol-ene polymerization, it allows us to produce thick structures with very high aspect ratios. In addition, we have also demonstrated the preparation of preceramic polymer based organogels by employing large amount of organic solvent within the polymer-thiol system by using the same radical-mediated polymerization. This versatility concerning the usage of a wide variety of solvents and pore forming agents could open a new approach to the preparation of highly porous preceramic polymer and subsequently porous polymer derived ceramics. In Chapter 5 we will demonstrate the preparation of polymer derived ceramics by freeze casting and freeze drying, which are both assisted by thiol-ene click reaction.

4 Thiol-ene click chemistry assisted additive manufacturing

4.1 Overall approach

As shown in the Chapter 3, thiol-ene click chemistry has been proven as an effective approach to cross-link the Si-containing preceramic polymers with suitable photoinitiators into infusible thermosets. Upon the absorption of incident photons, photoinitiators generate free radicals, which subsequently initiate cross-linking by addition reaction between the alkene side groups of preceramic polymers and thiol groups, as shown in Figure 20. Certain characteristics of this approach, such as fast reaction kinetics, high conversion and applicability to different classes of preceramic polymers make it highly suitable for the stereolithographic additive manufacturing of polymer-derived ceramics.

In this chapter, a novel stereolithographic additive manufacturing method based on VAT photopolymerization utilizing fast and inexpensive thiol-ene click chemistry is developed to 3D print Si-containing thermosets which are subsequently pyrolyzed into ceramics. The schematic representation of this approach is shown in Figure 21, which comprises three steps, namely (A) resin preparation, (B) additive manufacturing (3D printing) and (C) post-processing (pyrolysis).

4.1 Overall approach

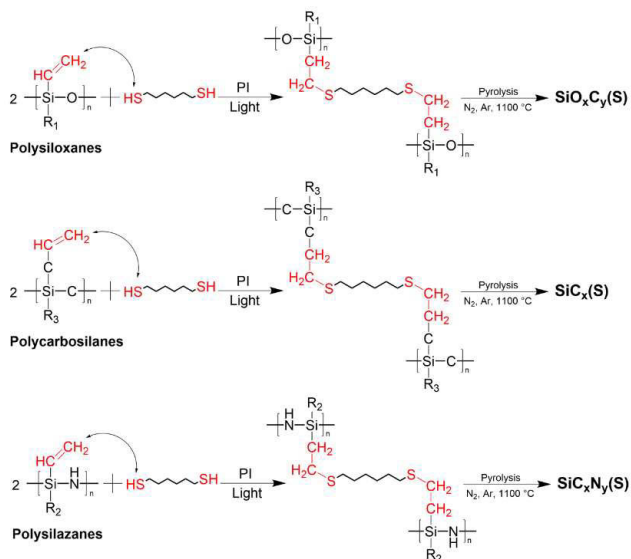


Figure 20. Schematic of the simplified thiol-ene click chemistry approach towards polymer-derived ceramics based on photoinduced cross-linking of vinyl-containing Si-based preceramic polymers with 1,6-hexanedithiol via an anti-Markovnikov addition followed by the pyrolysis at 1100 °C in N₂/Ar. Reprinted by permission from X. Wang et al.: ‘Additive manufacturing of ceramics from preceramic polymers: A versatile stereolithographic approach assisted by thiol-ene click chemistry’, *Additive Manufacturing*, 2019, 27, 80-90. Copyright 2019 Elsevier.

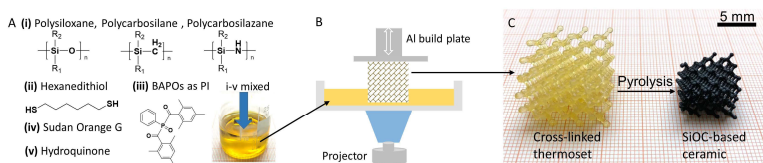


Figure 21. Additive manufacturing of ceramics from preceramic polymers: schematic representation of thiol-ene click chemistry-based stereolithography. (A) The preceramic photopolymerizable (B) Photopolymerization of preceramic resins in a benchtop DLP (C) Ceramic part after pyrolysis. Reprinted by permission from X. Wang et al.: ‘Additive manufacturing of ceramics from preceramic polymers: A versatile stereolithographic approach assisted by thiol-ene click chemistry’, *Additive Manufacturing*, 2019, 27, 80-90. Copyright 2019 Elsevier.

4. Additive manufacturing of PDCs

To achieve reproducible printing results and in turn, good quality final ceramic parts, the resin formulations, printing process and the post processing are investigated in detail and optimized. The details are given below.

- A) The photopolymerizable resins containing preceramic polymers are developed in this work. Besides Si-containing polymers, they contain thiols, photoinitiators, photoabsorbers and free radical scavengers. To utilize this hybrid polymer system for suitable stereolithography based additive manufacturing technology, the role of each component is thoroughly investigated and their respective amounts are optimized to fit to the process requirements. The resins are adjusted not just for a simple UV-curing experiment, but for the whole vat photopolymerization process, so that the prepared resins were suitable for the fabrication of complex three-dimensional structures with good quality and reproducibility. In the following sections, the influences of the nature of preceramic polymers, the polymer-to-thiol molar ratio, and the role and concentration of photoinitiators and photoabsorbers are discussed. Characteristics, such as curing efficiency, curing depth, minimal exposure time of photopolymerizable resins containing preceramic polymers are investigated to achieve a suitable resin formulation for the application of different preceramic polymer-based photopolymers in the stereolithographic process.
- B) Due to the fast and efficient thiol-ene click chemistry with preceramic resin formulations developed in this work, the additive manufacturing process can be effectively performed with conventional light sources (such as projectors) on a benchtop Digital Light Processing (DLP) 3D printer. For that purpose, the LittleRP2, an open source DLP printer, is assembled with a modified commercial projector to allow short-distance focusing. The software Creation workshop is

4.1 Overall approach

utilized to control the printing process and to optimize the printing parameters. Additionally, a new resin tank with FEP film as the bottom layer is designed and constructed to facilitate the detachment of fabricated thermosets. Furthermore, because the developed preceramic polymer resins possess good optical transparency with minimal light scattering, the preceramic resins are further applicable for more sophisticated techniques such as two-photon polymerization^{108, 109} and microstereolithography¹¹⁰.

- C) The optimized resin formulations, equipment and process parameters allow the printing of three-dimensional objects with complex geometry, ranging from cellular lattice structures to monolithic parts. Thermosets fabricated from preceramic polymers demonstrate the delicate structure and freedom of design obtained from 3D printing. The 3D printed thermosets are subsequently pyrolyzed to obtain SiOC, SiC and SiCN ceramics. The polymer-to-ceramic transformation is studied extensively via thermal gravimetric analysis (TGA) coupled with in-situ mass spectroscopy (MS) to determine the weight loss stages and the mechanism of the ceramization process. X-ray imaging (radiography) and tomography are utilized to examine the porosity and the presence of cracks inside the pyrolyzed samples. The chemical composition and microstructure of 3D-printed PDCs are further investigated via ATR-FTIR, XPS, Raman spectroscopy, SEM and TEM. Finally, the mechanical properties of fabricated SiOC samples are evaluated by nanoindentation and compression tests.

4.2 Process design

4.2.1 Selection of manufacturing equipment

The stereolithographic additive manufacturing with preceramic resins is performed on the DLP printer LittleRP2 (Brad “goopyplastic” Hill, Santa Barbara, CA) with an Acer X152H projector (New Taipei City, Taiwan) as the light source. The commercial projector is specifically modified to allow the short distance focusing. The setup and key components of LittleRP2 are shown in Figure 22, where the resin tank sits on top of a transparent support plate, and the emitted horizontal light from the projector is reflected to the vertical direction with first surface mirror, which is positioned at a 45° angle to the horizontal direction. The vertical movement of the building platform is allowed with a Z stepper motor. A separate computer, which runs the software Creation Workshop (DataTree3D, Dallas, TX, USA), is connected to the projector and the built-in Arduino microcontroller, which controls the stepper motor to coordinate the selected light exposure and building plate movement.

In a typical printing process, the 3D model is first sliced into 2D cross sections with the Creation Workshop software. Then the building platform is lowered into the resin tank and positioned one-layer thickness above the bottom of vat, followed by selective photocuring of the resin in-between. The building plate subsequently moves upwards to detach the cured polymer from the bottom of the resin tank, and repeat the whole process until the final 3D model is obtained.

Since the LittleRP2 is an open 3D printer running with an open source software, which imparts huge freedom in printer modifications and printing conditions. It is considered an ideal DLP printer for the support of research and innovation.

4.2 Process design

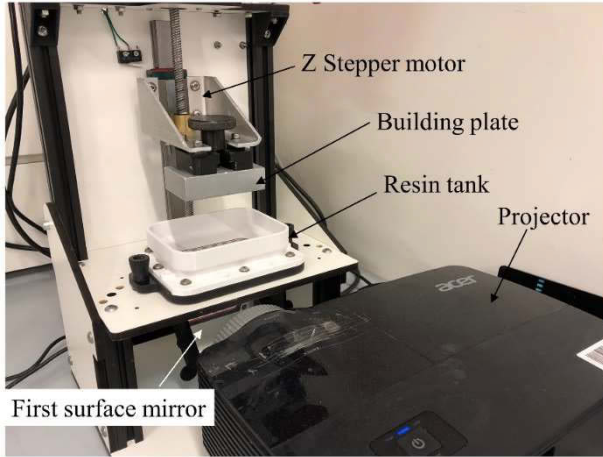


Figure 22. Set up of the LittleRP2 DLP 3D printer with mounted projector, which is modified to allow short distance focusing.

4.2.2 Resin tank design

In the bottom/up SLA (also called inverted SLA or DLP 3D printing), the building platform is lowered into the resin tank stepwise to specify the layer thickness. The light source then illuminates through the bottom of the resin tank and selectively cures the liquid photopolymer. Therefore, the bottom of the resin tank needs to possess high transparency to allow the transmission of emitted photons without attenuation. Another issue regarding the inverted bottom-up SLA or DLP is that the photocured resin will be attached between the building platform (or the last completed layer) and the bottom of the resin tank. When the building platform moves up, a detachment of the freshly-cured polymer from the bottom of the resin tank will occur, which is accompanied by a noticeable detachment force ¹¹¹. Sometimes the detachment force is too significant and leads to the incomplete detachment and failure of the printing ¹¹². In order to facilitate easy detachment, a non-adhesive transparent layer is usually applied to the bottom of the tank. In this work, an inverted DLP printer was chosen because this set-up

4. Additive manufacturing of PDCs

requires small amounts of material for each print, as only a sufficient volume of resin to cover the bottom of the resin tank is necessary. This is a significant advantage when using preceramic polymers as the photocurable resin due to their relatively high price.

Two most commonly used non-adhesive materials for the release layer at the floor of the resin vat are polydimethylsilicone (PDMS), and FEP, a thin transparent Teflon-based sheet. Both materials possess high optical transparency and low adhesiveness, with PDMS performing better in the aspect of non-sticking for most photopolymers. In the initial stage of this work, a Formlabs Form 2 SLA printer is utilized to print the developed preceramic polymer resins. This printer utilizes PDMS as the floor coating of the resin tank combined with a sliding mechanism to assist the detachment of the freshly-cured layer. This combination of material and mechanical movement is proven to be successful for most acrylate- or methacrylate-based photopolymers. Nonetheless, with silicone-based preceramic polymer resins, the printing with the Form 2 failed. As shown in Figure 23, the newly-cured thermoset layer is not successfully released from the bottom of the resin tank, and the detachment force is large enough to tear the printed apart. Photopolymer synthesized from thiol-ene click reaction is known to possess low mechanical strength and hardness, which is attributed to the flexible thioether linkage, with the C-S-C bond angle approaching 90° ^{113, 114}. Unlike mechanically-stable acrylate- or methacrylate-based photopolymers, the polymer synthesized from thiol-ene monomers cannot survive hundreds of peeling off motions during the printing process, and one unsuccessful release will lead to complete failure of the prints. Additionally, PDMS has a tendency to clouding due to its relatively loosely-packed polymer network, which allows the diffusion of foreign molecules.

4.2 Process design



Figure 23. Printing failures of a preceramic polymer resin in the Form 2 SLA printer due to unsuccessful release from the bottom of the resin tank.

Instead, an FEP film mounted with raised edges support plate is employed as vat to facilitate the detachment of preceramic polymer cured with thiol-ene polymerization. The detailed illustration of such a VAT design is shown in Figure 24. The advantage of this design lies in the placement of spacers (0.35 mm thick) at the edge of the supporting acrylate glass lifting the FEP film up slightly, which will allow the air to travel through in between the FEP film and support plate, and facilitate the separation of these two parts. As seen in the illustration during the peeling step, the highly tensed FEP film starts to bulge up at positions where the liquid polymer is cured and sticking to the FEP film. This process creates peeling edges in every direction of the printed parts and it can be assumed that the vat is being tilted from every direction. As a result, the detachment force with this peeling mechanism is significantly reduced compared to sliding or a simple pull-up mechanism, which allows the 3D printing of mechanically-weak photopolymers based on preceramic polymers. Figure 25 shows a cylindrical part prepared from SPR212 resin that was successfully printed without detachment failures.

4. Additive manufacturing of PDCs

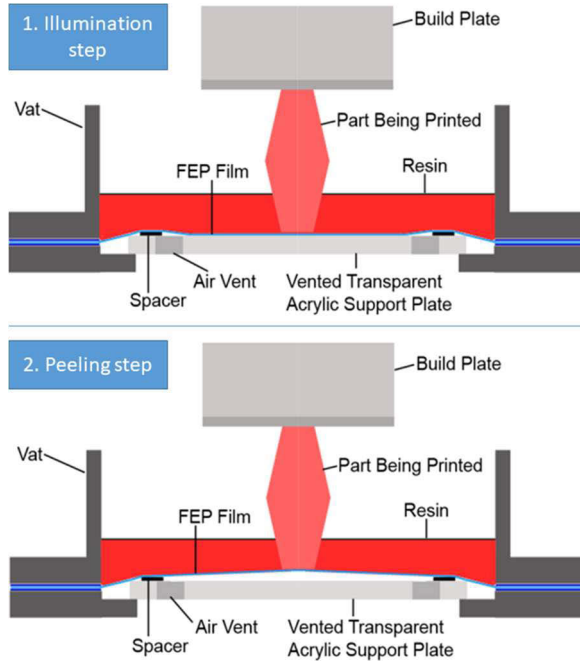


Figure 24. FEP Teflon film based 3D Printer Resin Vat with Raised Edge Vented Support Plate ¹¹⁵.

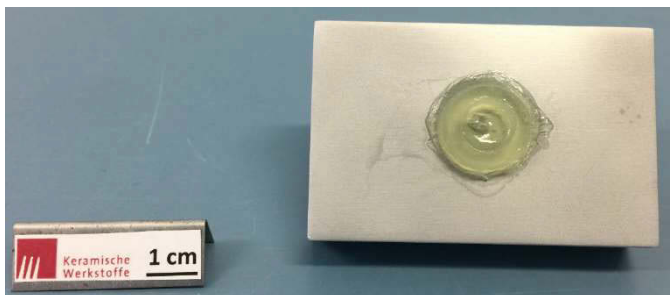


Figure 25. 3D-printed SPR212 cylinder utilizing the FEP film-based VAT design. The significant observed over-curing is due to the absence of photoabsorbers in the resin.

4.3 Resin formulations

4.3.1 Selection of preceramic polymers

Three preceramic polymer types, namely polysiloxane, polycarbosilane and polycarbosilazane, are applied as resins in the stereolithography approach, and after thermolysis yields SiOC-, SiC- and SiCN-based polymer-derived ceramics. As demonstrated in Chapter 3, polysiloxane SPR212 and polysilazane Dura1800 show excellent reactivity with dithiol with very fast reaction rates, achieving high cross-linking degrees in a short time (less than 10 s). The photocured thermosets from SPR212 and Dura1800 exhibit also sufficient shape stability, mechanical strength and elasticity, making these systems suitable for stereolithographic additive manufacturing.

Polysiloxane H62C resin demonstrates slightly different behavior, i.e., the photopolymerization proceeds more slowly, yielding less stable thermosets. Based on the evolved reaction heat in H62C photopolymerization compared to that for SPR212 and Dura1800 systems, it can be assumed that there are less vinyl groups present in the H62C polymer as well. Consequently, the thermosets obtained from H62C resins are less stable, which makes this system less suitable for bottom-up stereolithography and DLP printing. This issue will be discussed in more detail in the following sections.

Polycarbosilane SMP10 has the lowest fraction of carbon-carbon double bonds (i.e., allyl groups) according to its chemical structure. The effectiveness of thiol-ene click reaction is also strongly diminished by the polymer's high intrinsic light absorbance from visible to UV range. Nonetheless, SMP10 is the only commercially-available allyl-containing preceramic polymer for the synthesis of SiC-based high performance ceramics. Since the latter are of great interest for industrial applications, the SMP10 polymer is also utilized in the 3D printing process despite its low photocurability.

4. Additive manufacturing of PDCs

The photopolymer used in SLA or DLP 3D printer should have a relatively low apparent viscosity at shear rates between 0 and 1000 s^{-1} , preferably below 3000 mPa·s, to facilitate the self-leveling and recoating of a fresh new resin layer after each successive print ⁷⁰. The three preceramic polymers utilized in this work are therefore characterized for their rheological behavior at shear rates between 5 and 100 s^{-1} . Figure 26 shows the almost ideal Newtonian rheological behavior of the utilized preceramic polymers, as their dynamic viscosities are not influenced by the variation of shear rates. The viscosity values at 25 s^{-1} shear rate are listed in Table 12, and they are far smaller than 3000 mpa·s. The low viscosity enables effective self-recoating of fresh layer of employed resin during the print process, and a recoater/wiper system is most likely not needed during the stereolithography process.

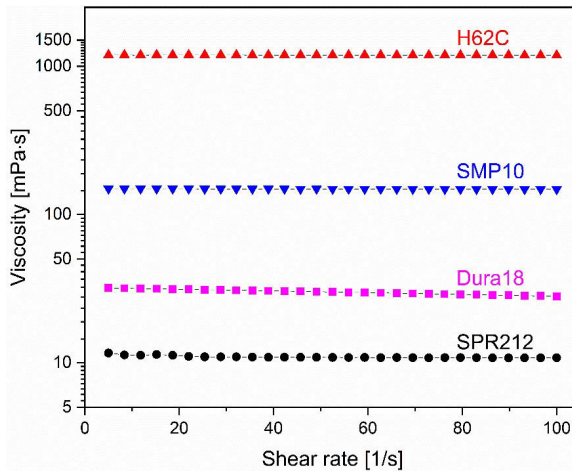


Figure 26. Dynamic viscosity of intrinsic preceramic polymers utilized in this thesis.

4.3 Resin formulations

Table 12. Viscosity of employed preceramic polymer at shear rate of 25 1/s.

Preceramic polymer	Viscosity at shear rate of 25 s ⁻¹ [mPa·s]
SPR212	11
Dura18	31
SMP10	149
H62C	1194

4.3.2 Selection of thiols

Due to the stoichiometric relationship between thiol groups and carbon double bonds consumed in the thiol-ene polymerization ¹¹⁶ (see also Figure 20), the preceramic resins are prepared by mixing the preceramic polymers and dithiol in a stoichiometric ratio, so that the molar ratio of thiol and carbon double bonds are equal. The structural formulas of Dura1800 and SMP10 are well-known and presented in Chapter 3. From the presented chemical structure and the approximated normalized molecular weight of preceramic polymer and, assuming consumption of all dithiol molecules, the required weight ratio of polymer to dithiol can be calculated according to the Equation 4:

$$\frac{m_{2T}}{m_{PCP}} = \frac{M_{2T}}{M_{PCP}} \cdot \frac{n_{vinyl}}{2} \quad \text{Equation 4}$$

where m_{2t}/m_{pcp} represents the weight ratio of dithiol to polymer, M_{2T} is the molecular weight of dithiol, M_{PCP} is the calculated molecular weight of preceramic polymers, and n_{vinyl} represents the molar fraction of vinyl groups (which is equal to 0.2 for Dura1800 and 0.05 for SMP10). The factor 2 demonstrates that one dithiol molecule can cross-link two vinyl groups. The results of the calculation are presented in Table 13

4. Additive manufacturing of PDCs

Table 13. The weight ratio of polymer to dithiol calculated according to Equation 4.

	Durazane 1800	SMP10	SPR212	Dithiol
Molecular weight, g/mol	64.2·n	46·n	Not known	150
Calculated PCP to dithiol weight ratio	100:23	100:8	100:23	
Applied ratio	100:20	100:8	100:20	

However, there is not enough information to reveal the exact chemical structure of SPR212. From the technical datasheet of the provider (Starfire systems), it is known that Polyramic® SPR-212 is a liquid precursor to thermally stable silicon oxycarbide ceramics with various Si-R functionalities, including Si-H, Si-CH₃ and Si-C=C. Since it shows very similar results to Dura1800 in the UV-DSC characterization (see Chapter 3), it was assumed that the amount of vinyl groups is comparable to that in Dura1800. Therefore, the SPR212-based resin is prepared similarly to the Dura1800 dithiol system.

4.3.3 Selection of photoinitiators

The nature and properties of photoinitiator play an important role in the thiol-ene click reaction, as it generates free radicals when exposed to light, thus initiating the cross-linking of the polymers. The created free radical abstracts the hydrogen atom from a thiol group to form a thiyl radical, which subsequently attacks the C=C bond. A suitable photoinitiator should have an overlapping absorption spectrum with the emission spectrum of the used light source. In the used experiment set up, a commercial Acer DLP projector is utilized as the irradiation source. The projector's emission spectrum is not provided by the manufacturer, but it was known that a UV filter was placed in front of the light source. Therefore, instead of DMPA, BAPO is utilized as photoinitiator due to its absorbance in visible-light region

4.3 Resin formulations

(at wavelengths between 400 and 440 nm), while DMPA does not show any absorbance in this region.

A photopolymerization test using squares as a model shape is conducted to evaluate the curing efficiency of SPR212-2T and SMP10-2T systems mixed with different amount of BAPO, in order to select a suitable amount for rapid photopolymerization. Durazane1800 is not examined in this test due to its high reactivity with the moisture in air and its tendency to evolve hydrogen and ammonia. As SPR212 and Durazane1800 demonstrated very similar curing efficiency with DMPA as proved in the previous UV-DSC measurements, the determined amounts of BAPO in the SPR212-2T system is applied in the Dura1800-2T system as well.

Two SPR212-dithiol resins (PI_{test1,2}) are prepared by adding BAPO as PI in weight ratios of 1:100 and 1.5:100 in relation to the SPR212 contents. For easier understanding, the weight percent of PI is approximated to 1 wt% and 1.5 wt%, respectively. The exact resin formulations can be found in **Table 7**. Resultant resin mixture (light yellowish in color) is cast drop-wise onto the glass slides and placed above the transparent support plate made of acrylate glass as shown in Figure 27. A square-shaped projection is subsequently exposed to the resin from the bottom side with increasing illumination time (1 s, 2 s and 3 s). The resultant polymerized film together with the glass slides is washed with isopropyl alcohol to remove the unpolymerized resin, followed by drying in ambient air.

The photopolymerization results of SPR212 mixed with different amounts of BAPOs with increasing exposure time are shown in Figure 28. SPR212 resin mixed with 1 wt% BAPO demonstrates sufficient curing rates by obtaining a square-shaped film with sharp edges under 1 s of exposure to white light emitted by the projector. Nonetheless, highly wrinkled surface morphology, which is caused by the swelling effect of utilization of isopropyl alcohol during washing, can be clearly observed in the films obtained under 1 s and 2 s of illumination. The swelling of the prepared photopolymer is a clear indicator of insufficient cross-linking and polymer network, which allows the absorption of the isopropyl

4. Additive manufacturing of PDCs

alcohol. Thin films prepared from SPR212-2T resin blended with 1.5 wt% BAPO does not demonstrate a strong swelling effect, as it showed an unaffected surface after 2 s and 3 s of illumination. Based on this experiment, an amount of 1.5 wt% of BAPOs with respect to the mass of SPR212 and Durazane1800 is selected, as it allows a fast curing speed and highly cross-linked photopolymer network.

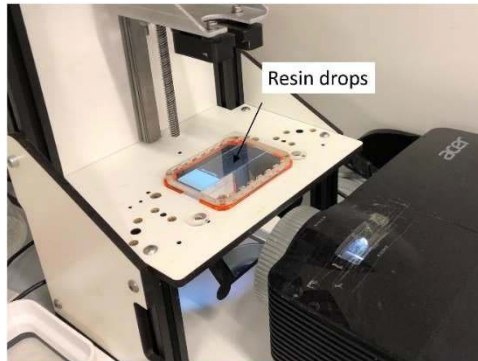


Figure 27. Set up to determine the photoinitiator contents.

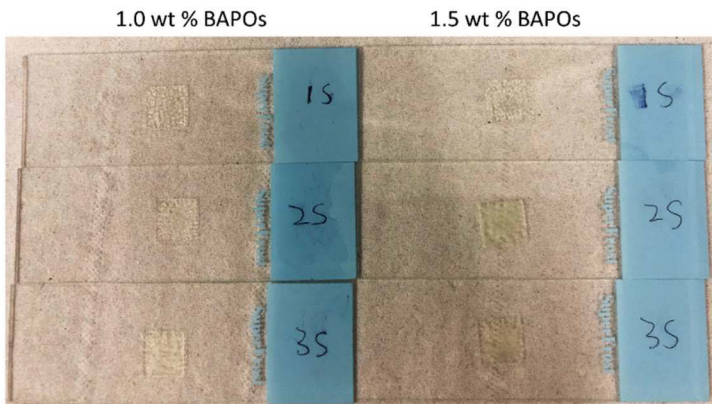


Figure 28. Results of photopolymerization tests for determining the optimal amount of photoinitiator for SPR212.

4.3 Resin formulations

4.3.4 Curing depth measurements and selection of photoabsorbers

Four SPR212-2T / SMP10-2T resins are prepared with different amount of Sudan Orange G as photoabsorber. Detailed compositions of each resin is listed in Table 14 and Table 7.

Table 14. Resin compositions for the curing depth measurements. Note the weight percent of BAPO and Sudan G is an approximation, for exact compositions please see Table 7.

Test	PCP	BAPO, wt. %	Sudan G, wt. %
C _d test1	SPR212-2T	1.5	0
C _d test2	SPR212-2T	1.5	0.05
C _d test3	SPR212-2T	1.5	0.1
C _d test4	SMP10-2T	1.0	0

To measure the curing depth precisely, a slightly different approach as compared to the method described in the last section is applied. As seen in Figure 29, a hollow cylindrical Teflon mold with a height of 15 mm is attached onto the glass slides and utilized as a resin container. The prepared preceramic polymer resin is cast into the mold until it is full, followed by applying photoillumination from bottom with different exposure time, ranging from 1 s to 10 s. The purpose for this modification is to avoid any unwanted reflection or scattering of incident light at the resin/air interface, which would lead to unreliable experiment results. Subsequently, the Teflon mold is carefully removed and the cured polymer together with glass slides is washed with isopropyl alcohol if SPR212 polymer was used, or with cyclohexane if SMP10 polymer was utilized. The resultant polymer films were dried in ambient air and their thicknesses were measured using a digital caliper.

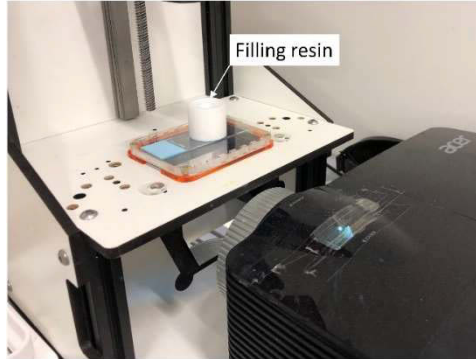


Figure 29. Set up for the curing depth measurements.

In general, uncontrolled photopolymerization is disadvantageous in the process of stereolithography, as it causes photocuring of unwanted areas, especially in the Z-direction (the direction at which the building platform moves). In order to increase the printing resolution in the Z-direction, photoabsorbers have to be introduced into the resin system to increase the attenuation of the incident light. Eventually, the resulting curing depth (C_d) under certain exposure time can be tuned to match closely with the predetermined layer thickness for 3D printing. Empirically speaking, C_d shall be 1.5 times or twice the value of the layer thickness to allow for a tight bonding between each printed layer and to simultaneously avoid significant over curing. Sudan orange G is selected as photoabsorber due to its high absorbance in the operational wavelength of the employed DLP projector. Subsequently, curing depth C_d measurements are conducted for SPR212-dithol-BAPO resin with addition of different amount of photoabsorbers (0 wt%, 0.05 wt% and 0.1 wt% with respect to SPR212) under the experiment set up as described in Chapter 2.

The relationship of the curing depth C_d with the applied energy dose E is expressed in Equation 1.

4.3 Resin formulations

$$C_d = D_p \cdot \ln\left(\frac{E}{E_c}\right) \quad \text{Equation 1}$$

where D_p is a parameter with unit of length, otherwise known as the attenuation length of the incident light, and E_c represents the critical energy dose at which a certain polymerization extent is required to reach the gel point of the photopolymer. Energy dose E as well as E_c can be expressed as the product of exposure energy density I with exposure time t and critical exposure time t_c , respectively. The energy density I and critical energy density I_c are assumed equal, so they cancel each other. Equation 1 can subsequently be expressed as follows:

$$C_d = D_p \cdot \ln\left(\frac{t \cdot I}{t_c \cdot I}\right) \quad \text{Equation 5}$$

$$C_d = D_p \cdot \ln\left(\frac{t}{t_c}\right) \quad \text{Equation 6}$$

$$C_d = D_p \cdot (\ln t - \ln t_c) \quad \text{Equation 7}$$

The curing depth C_d was measured for different PCP-2T resins over various exposure times. As shown in Figure 30, the x-axis is plotted in logarithmic scale to match the equation above, so that the linear relationship between C_d and $\ln t$ can be observed. The attenuation length D_p can be obtained from the slope of the curve and the critical exposure time t_c can be determined with the intercept of the linear fit with the x-axis (time scale). The resulting curing depths of one SPR212-2T resin containing 1.5 wt% photoinitiator BAPO and 0 wt% photoabsorber Sudan Orange G over different exposure times (Figure 30a) showed linear dependence, allowing the measured data to be fitted with linear function. Figure 30b shows the

4. Additive manufacturing of PDCs

results of SPR212-2T resins with the same BAPO content and varying photoabsorber contents of 0.05 and 0.1 wt% as well as results from SMP10-2T resin with 1.0 wt% BAPO and 0 wt% photoabsorber. It is notable that SPR212-2T resin with 1.5 wt% BAPO and without photoabsorbers (Figure 30a) exhibited extremely deep curing depths with an attenuation length D_p of 2263 μm and critical exposure time t_c of 0.9 seconds, which would lead to a significant overcuring effect when applying the resin in stereolithography. Blending the resin with only 0.05 wt% and 0.1 wt% of Sudan Orange G as photoabsorber led to the immediate reduction of the curing depth and prolongment of exposure time as shown in Figure 30b. This is due to the strong absorbance of photons emitted from the projector by Sudan Orange G. The attenuation length D_p of the resin mixed with photoabsorber is one magnitude lower than the D_p of resin without photoabsorber. Accordingly, the obtainable curing depth of resin with photoabsorbers is significantly reduced since the incident light is attenuated severely under the resin surface, which is a desirable characteristic for achieving stereolithography with good resolution. Note that the critical exposure time, which directly relates to the critical energy dose required for gel point degree photopolymerization, does not change as drastically as the attenuation length when employing photoabsorber. Thus it can be stated that the photoinitiator has a great influence on the critical energy dose, while the curing depth and attenuation length of incident light are largely determined by the photoabsorber and photoinitiator together. In this work, the layer thickness of each print is set to 100 μm to allow an overall rapid printing process; subsequently the desired curing depth is determined as 200 μm with acceptable exposure time. Since the SPR212-2T resin mixed with 0.1 wt% of Sudan G would require almost 7 s of illumination to reach 200 μm curing depth, 0.05 wt% of photoabsorbers for resins based on SPR212 and Durazane1800 was chosen.

4.3 Resin formulations

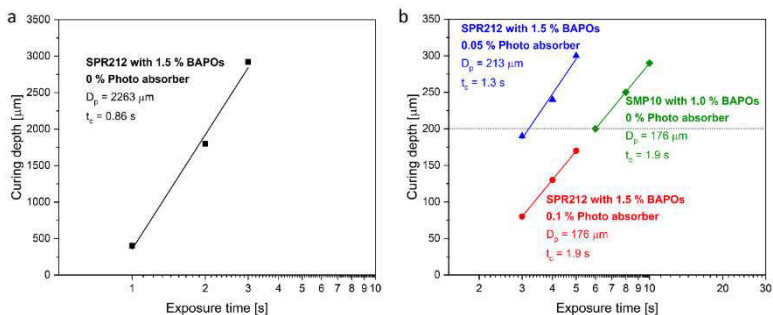


Figure 30. Measured curing depth versus exposure time for preceramic polymer-2T resins mixed with different amounts of photoinitiator BAPO and photoabsorber Sudan Orange G.

The polycarbosilane SMP10-2T resin blended with BAPO as photoinitiator demonstrated notably slower polymerization rate comparing to SPR212-2T (Figure 30b, green data points). This is due to SMP10's high absorbance in the operational wavelength of the DLP projector. For this resin, 1 wt% of BAPO as photoinitiator is chosen to trigger the thiol-ene click reaction. Adding a higher amount of BAPO is not considered due to the potentially significant reduction of curing depth caused by the polymer itself, which was demonstrated in Chapter 3. The critical exposure time to allow the formation of a photopolymer network with a thickness of $200 \mu\text{m}$ is significantly increased to 6 s, compared to SPR212-2T resin without the addition of photoabsorbers. The calculated attenuation length D_p and critical exposure time t_c of the SMP10-2T resin lies on par with the SPR212-2T resin blended with 0.1 wt% of photoabsorbers, which shows that SMP10-2T resin exhibits the same behavior as SPR212-2T resin with photoabsorber. Thus the SMP10 polymer serves as both the reacting species for thiol-ene click reaction and photoabsorber in the resin system. Based on this result, 1 wt% BAPOs as the amount of photoinitiator and extrinsic photoabsorber were not necessary in the SMP10-2T resin for the 3D printing process.

4. Additive manufacturing of PDCs

The attenuation length D_p gives a rough estimate of how far the incident light can penetrate through the resin surface, and it is inversely proportional to the attenuation factor A_d , which describes how strong the incident light is attenuated. Figure 31 illustrates the attenuation length of 2T-modified preceramic polymer resins in comparison to resins used for ceramic stereolithography, which are based on suspending ceramic particles in liquid photopolymers. Because the SPR212 polymer and 2T are highly miscible, the resultant transparent solution has ultra-high attenuation length above 2000 μm , even when mixed with 1.5 wt% of PI. Introducing extra PA or the utilization of SMP10 polymer will lead to the significant decrease of attenuation length because of absorbing effects. In contrast, the photopolymer suspended with ceramic particles demonstrate decreased attenuation length because of the scattering of incident light by the suspended ceramic particles. The resin mixed with SiO_2 powder (which has a refractive index RI close to the photopolymer) shows low attenuation factor, while the resin consisting of Al_2O_3 powder with high RI demonstrates a significant reduction of attenuation length due to the strong scattering effect.

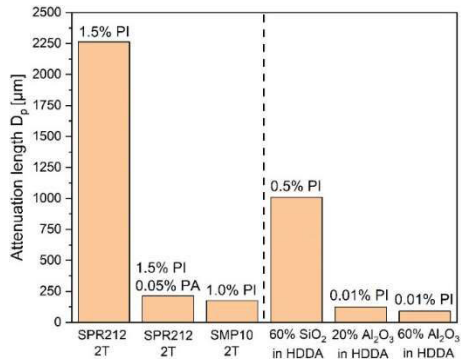


Figure 31. Calculated attenuation length D_p of preceramic polymer-2T resins compared to the attenuation length of hexanediol diacrylate (HDDA) filled with ceramic particles, PI represents photoinitiator, PA represents photoabsorber. The data for SiO_2 in HDDA is taken from ⁷⁴, while the data for Al_2O_3 in HDDA is taken from ⁷³.

4.3 Resin formulations

With the experimental results from resin formulations, it can be concluded that the 2T-modified preceramic polymer resin exhibits two distinct advantages over conventional ceramic suspension-based resins used for ceramic stereolithography. First, the preceramic polymer-2T resin possess relative low viscosity compared to the polymer with high solid content of ceramic powders. This eliminates the requirement for a recoater system since the resin can self-recoat a fresh layer during the platform lift-up. Second, the absence of ceramic powder also avoids the light scattering effect, thus allowing a higher printing resolution comparable to polymer-based stereolithography.

4.4 Additive manufacturing of preceramic polymers and their conversion to ceramics

4.4.1 Printing parameters

SPR212, Durazane 1800 and SMP10-based resins are finally applied with the LittleRP2 printer to conduct the 3D printing of polysiloxane, polycarbosilane and polycarbosilazane. The exact compositions of each preceramic polymer resin are shown in Table 15. Please note that tiny amount of hydroquinone is added in the final SPR 212 and Dura18 resin mixtures to prolong their shelf life.

Table 15. Resin formulations for the application in LittleRP2 DLP printer.

	2T	BAPO	Sudan Orange G	Hydroquinone
SPR212 , 20 g	4 g	0.3 g	10 mg	1 mg
Dura18 , 20 g	4 g	0.3 g	10 mg	1 mg
SMP10 , 20 g	1.6 g	0.2 g	0 mg	0 mg

The creation workshop software allows the modifications of many printing parameters. The layer thickness during printing is set to be 100 μm in this work, so objects can be printed with a fast speed. Besides the layer thickness, exposure time of each layer is determined

4. Additive manufacturing of PDCs

based on the curing depth measurements, based on the criterion that the obtained C_d shall be 1.5 times or 2 times the layer thickness. Exact exposure time is further modified through various printing tests to find out the optimized time. The specifications of printing parameters are shown in Table 16.

Table 16. Printing parameters set by creation workshop.

Parameters	SPR212, Dura1800	SMP10
Layer thickness [mm]	0.1	0.1
Exposure time [ms]	3500	7000
Bottom exposure time [ms]	4500	7500
Bottom layers	3	3
Z lift distance [mm]	5	5
Z lift speed [mm/min]	30	30
Z bottom speed [mm/min]	30	30
Z retract speed [mm/min]	30	30
Rest interval [s]	1	1

After the printing process is completed, the fabricated thermoset from preceramic polymer resting on the building platform is immersed in a tank filled with organic solvents to wash away the unpolymerized resins. The polysiloxane is washed with isopropyl alcohol, and the polycarbosilane and polycarbosilazane are washed with cyclohexane. After washing, the printed parts were carefully removed from the building plate and vacuum dried, followed by post-curing under UV lamp for half an hour.

4.4.2 Fabricated thermosets

The photopolymerization behavior of polysiloxane, polycarbosilane and polysilazane have been intensively studied in the previous section and chapter. Despite the fact that SMP10 has a low photoreaction rate with 2T and the non-oxygen containing preceramic polymers, namely Durazane 1800 and SMP10 are unstable

4.4 Additive manufacturing of PCP and their conversion to ceramics

in air, all three preceramic polymer resins were successfully applied in the benchtop DLP printer and 3D-printed, complex-shaped thermoset parts were achieved as demonstrated in Figure 32.

Highly cellular lattice-like structure with SPR212 and a complicated hollow turbine part with Durazane 1800 are well-fabricated with the developed approach, demonstrating almost no printing restriction in the geometry of the 3D structures. The Kelvin cell structure (Figure 32 A) is presented with large overhangs, cavities and with strut thickness down to several hundreds of micrometers. The successful 3D printing of such delicate geometry demonstrates again the high photoreactivity of the preceramic polymer with multifunctional thiols, the optimized resin formulations and improved FEP film resin tank design, which facilitate the detachment and thus allows the continuous 3D printing.

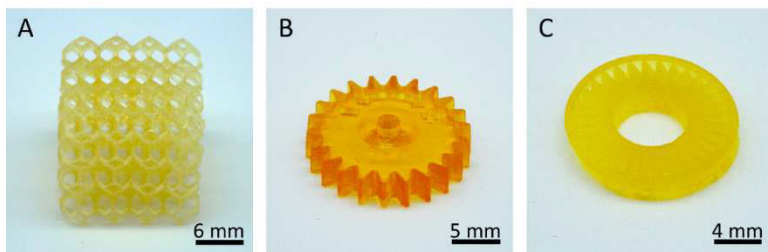


Figure 32. Representative examples of thermoset parts fabricated from three different polymer classes: (A) Kelvin cell structure printed with polysiloxane SPR212, (B) cog wheel printed with polycarbosilane SMP10 and (C) turbine structure printed with polycarbosilane Durazane 1800. Reprinted by permission from X. Wang et al.: ‘Additive manufacturing of ceramics from preceramic polymers: A versatile stereolithographic approach assisted by thiol-ene click chemistry’, *Additive Manufacturing*, 2019, 27, 80-90. Copyright 2019 Elsevier.

Meanwhile, the resin based on polycarbosilane SMP10 is utilized successfully to print simple structures without substantial amounts of overhangs or undercuts, which are largely present in the slices of a Kelvin cell or a turbine structure. Printing the cog wheel structure (Figure 32B) starting with the bottom is simpler, as each freshly-cured polymer layer is either identical or smaller than the

previously cured layer. This structure design facilitates the peel-off process with less developed stress and thus imparts less mechanical challenges to the cured photopolymer, since SMP10-2T resin is especially mechanically soft and prone to tearing under tension. Nonetheless, the 3D printing of all three preceramic polymers proved successful: the produced thermosets are believed to be synthesized via the thiol-ene click reactions presented in Figure 20.

4.4.3 Thermal transformation of thermosets into ceramics

To transform the cross-linked thermosets into ceramics, they are subjected to further processing steps. First, they are rinsed with organic solvents (isopropanol for SPR212 and anhydrous cyclohexane for SMP10 and Durazane1800), to remove the remaining non-polymerized resin on the surface or inside the cavities, and post-cured under UVA light between 350 – 400 nm to complete the polymerization process and to enhance their mechanical stability. In the next step, they are transferred to a tube furnace and pyrolyzed in N₂ at 1100 °C according to heating profile A as described in Chapter 2. During pyrolysis, the cross-linked preceramic polymers decompose and convert into amorphous Si-containing ceramics; this transformation is usually accompanied by the release of hydrogen, methane and other carbon- and hydrogen-containing species. This process entails mass loss, isotropic volume shrinkage and densification of the material itself. Upon the pyrolytic conversion of cross-linked polymers to the corresponding ceramics, a linear shrinkage of roughly 30 % is observed (see Figure 33). Because the shrinkage is isotropic, the thermoset is transformed into a ceramic part without any noticeable distortion in the architecture. The preservation of geometry means that utilizing thiol-ene click reactions is an effective and easily-accessible pathway to highly cross-link the preceramic polymer into a rigid 3D thermoset polymer, which is infusible and resistant to melting during the pyrolysis step. This is a

4.4 Additive manufacturing of PCP and their conversion to ceramics

key characteristic and requirement for the stereolithography of polymer derived ceramics. The thiol-ene click reaction combined with preceramic polymers provides an effective route towards the AM fabrication of ceramic parts with excellent resolution and smooth surfaces.

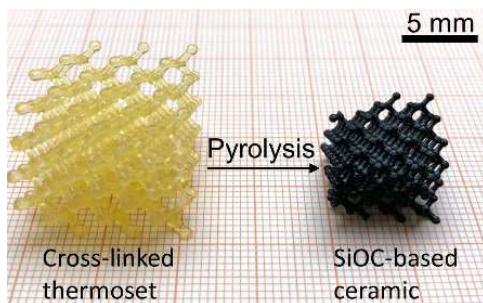


Figure 33. A representative printed cross-linked thermoset of SPR212 and the resultant glassy ceramic formed upon pyrolysis at 1100 °C under N₂ atmosphere, demonstrating a roughly 30 % linear shrinkage. Reprinted by permission from X. Wang et al.: ‘Additive manufacturing of ceramics from preceramic polymers: A versatile stereolithographic approach assisted by thiol-ene click chemistry’, *Additive Manufacturing*, 2019, 27, 80-90. Copyright 2019 Elsevier.

Using the procedures developed in the present work, further ceramic compositions beyond the SiOC, SiC and SiCN materials studied here can be obtained by using suitable preceramic polymers. General guidelines for the selection of appropriate ceramic precursors for use with thiol-ene click reactions can be stated as follows: (i) an inorganic-organic hybrid polymer or monomer, where the inorganic core comprises species (such as Al, B, Si, Ti or Zr) that form stable oxides, carbides, nitrides or oxycarbides upon pyrolysis; (ii) the presence of unsaturated carbon double or triple bonds, such as those in vinyl groups; (iii) the propensity to form thiyl radicals through photoinitiation. Furthermore, the methodology developed here can be easily adapted to produce composite ceramics containing fillers to impart catalytic, photocatalytic or magnetic functionalities.

4. Additive manufacturing of PDCs

In this work, I am able to fabricate black glassy ceramics composed of silicon oxycarbide, silicon carbide and silicon carbonitride. Figure 34 A-D displays several examples of ceramic parts—ranging from cellular lattices to bulk structures—fabricated by our approach. Substantial internal flaws or major cracks, which can lead to the failure of the pyrolyzed parts, are not observed in their corresponding radiography images (Figure 34 E - H), which validate the concept of our approach to the AM fabrication of high-performance ceramics. Nonetheless, small amounts of voids and tiny cracks can be observed in the magnified radiography images of the cog wheel and turbine structures, respectively. The cause for the presence of such flaws is connected to the nature of polymer-derived ceramics, in that the polymer-to-ceramic conversion is accompanied with volume shrinkage (density increase), gas release and formation of microporosity, all of which could lead to the formation of defects such as cracks and pores. If one dimension of the printed parts become so thick that the evolved gaseous species within the sample does not have sufficient time to out-diffuse to the surface of the specimen, the gases can build up a substantial internal pressure and lead to the cracking and failure of the final ceramic parts. To avoid cracking during pyrolysis, the maximum wall thickness of the printed structures is limited to 2 mm. The SiOC and SiCN(O) parts are successfully fabricated with satisfying resolution and very smooth, pore-free surfaces. Surprisingly, SiC parts, which are fabricated from the polycarbosilane SMP10, cracks and exploded during pyrolysis when the heating temperature reached 600 °C. At temperatures between 550 and 800 °C, SMP 10 transforms into an inorganic SiC-based material accompanied by the release of hydrogen (H₂) and methane (CH₄), as well as volumetric shrinkage (the density increases 2-fold), which is indicative of the polymer-to-ceramic conversion^{24, 117, 118}. As discussed before, relative to SPR212 and Durazane 1800, the SMP10 polymer was cross-linked at a lower degree due to the lower amount of vinyl functionalities. More importantly, the FTIR spectrum of SMP10 suggests its polymer structure contains greater amounts of silyl (Si-H) and carbosilane (Si-CH₂-Si) groups, leading to

4.4 Additive manufacturing of PCP and their conversion to ceramics

a greater hydrogen and methane gas evolution during pyrolysis. Based on a recent report by Raj et al.¹¹⁹, it is suggested that the fracture behavior of the polymer-to-ceramic transition is dominated by the release of hydrogen and methane, starting at temperatures around 700 °C. Therefore, it is believed that the significant hydrogen and methane gas egression during the ceramization process of SMP10, along with shrinkage stresses, resulted in the formation and rapid propagation of cracks, thereby manifesting in the explosion of samples. High over-pressure of hydrogen or methane as the pyrolyzing atmosphere could be used to oppress such crack formation.

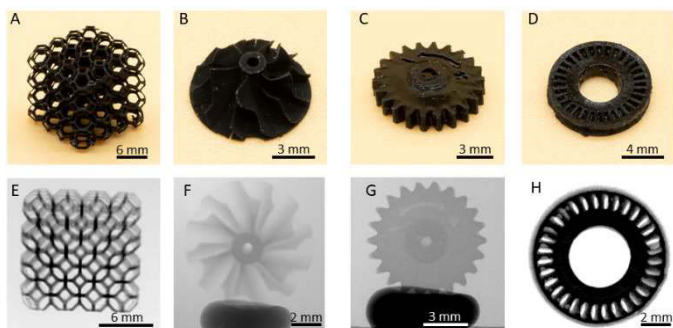


Figure 34. Examples of ceramic components free from macrosized voids and defects fabricated by pyrolyzing the cross-linked thermosets (shown in Fig. 4): (A-D) Images of components and (E-H) the corresponding radiography images of the (A,E) SiOC Kelvin cell structure; (B,F) SiOC turbine impeller; (C,G) SiCN(O) cog wheel and (D,H) SiCN(O) turbine. Reprinted by permission from X. Wang et al.: ‘Additive manufacturing of ceramics from preceramic polymers: A versatile stereolithographic approach assisted by thiol-ene click chemistry’, *Additive Manufacturing*, 2019, 27, 80-90. Copyright 2019 Elsevier.

The polymer-to-ceramic transformation is examined by thermal gravimetric analysis coupled with mass-spectrometry, with results shown in Figure 35. The 3D-printed SPR212, SMP10 and Durazane 1800 after pyrolyzing at 1100 °C demonstrate ceramic yields of 51.8 %, 70.4 % and 63.2 %, respectively. As expected, the

4. Additive manufacturing of PDCs

overall weight loss of cured preceramic resins is larger in comparison to pure preceramic polymers^{18, 120}. This additional weight loss is attributed to the presence of thiol monomers and the evaporation and breakdown of the thioether linkages during the pyrolysis, since they are thermally unstable. As seen in Figure 35A, a substantial release of sulphur-containing species with low molecular mass, including SO₂, CH₃SH and H₂S, is observed within the temperature range between 400 and 600 °C.

As verified by ATR-FTIR, X-ray photoelectron spectroscopy, and TEM characterization (Figure 36), 3D printed parts pyrolyzed at 1100 °C in flowing nitrogen are amorphous silicon-containing ceramics with a general formula of SiC_xO_yN_z, with small amount of residual sulfur. Their chemical composition depends on the preceramic polymer applied for the fabrication. The exact chemical composition and empirical structure is listed in Table 17.

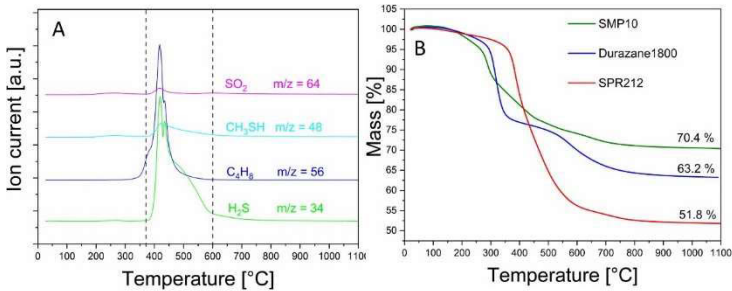


Figure 35. STA characterization of the polymer-to-ceramic transformation of the cross-linked thermosets fabricated from SPR212, SMP10 and Durazane 1800: (A) selected MS data for SPR212 indicating the release of SO₂ (m/z = 64), CH₃SH (m/z = 48), C₄H₈ (m/z = 56) and H₂S (m/z = 34) due to the decomposition of thioether linkages during the major mass loss region and (B) TG curves indicating the overall weight loss. Reprinted by permission from X. Wang et al.: ‘Additive manufacturing of ceramics from preceramic polymers: A versatile stereolithographic approach assisted by thiol-ene click chemistry’, *Additive Manufacturing*, 2019, 27, 80-90. Copyright 2019 Elsevier.

4.4 Additive manufacturing of PCP and their conversion to ceramics

Table 17. Elemental composition of ceramics pyrolyzed at 1100 °C in flowing nitrogen.

Preceramic polymer	Fabricated ceramic	Content, at. %				
		Si	O	C	N	S
Polysiloxane SPR212	SiC _{1.39} O _{1.53} S _{0.01}	5.48	8.88	5.47		0.17
Polycarbosilane SMP10	SiC _{1.22} (O _{0.78})S _{0.04}	3.00	5.77	0.04		0.19
Polycarbosilazane Durazane 1800	SiC _{1.02} N _{0.59} (O _{1.12})S _{0.04}	8.52	8.92	6.22	5.27	0.07

ATR-FTIR spectra of pyrolyzed PDCs demonstrate typical broad absorption bands attributed to the Si-O-Si, Si-C-Si and Si-N-Si bonds in accordance to the selected preceramic polymer. The complete disappearance of absorption bands associated with organic groups indicates a complete polymer-to-ceramic transformation. From the XPS data, it is clear that ceramics with targeted compositions of SiC and SiCN possess significant oxygen content. These materials again demonstrate broad absorption bands around 1100 cm⁻¹ in the FTIR spectra, which are attributed to Si-O-Si stretching vibrations. Since the additive manufacturing process in this work is performed in ambient air, the silane (-Si-H) and silazane (Si-N-Si) bonds contained in the preceramic polymers reacted with atmospheric oxygen and moisture rapidly, leading to the increased oxygen content. Consequently, the “reacted” SMP10 and Durazane 1800 polymers are thermally converted into SiC(O) and SiCN(O) ceramics, respectively. To minimize oxidation in stoichiometric SiC and SiCN ceramics, the entire fabrication process would have to be conducted under an inert atmosphere, for example in a glovebox filled with nitrogen.

4. Additive manufacturing of PDCs

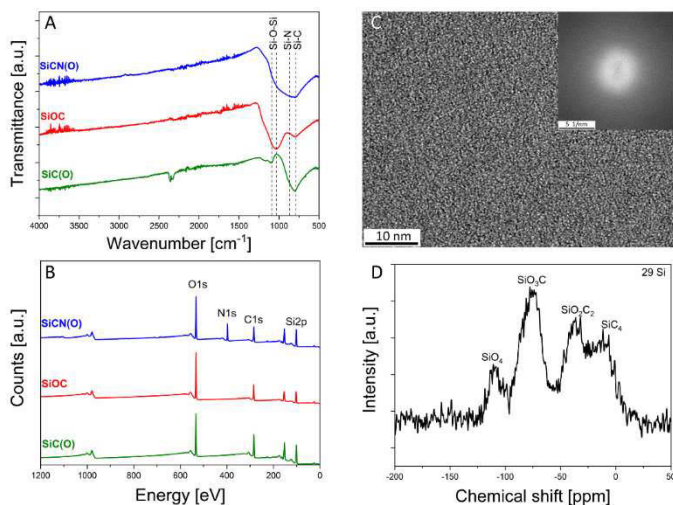


Figure 36. Characterization of additively-manufactured polymer-derived ceramic materials: (A) ATR-FTIR data; (B) X-ray photoelectron spectra of SiOC (red), SiC(O) (green) and SiCN(O) (blue) synthesized at 1100°C from SPR212, SMP10 and Durazane 1800, respectively. Analysis of SPR212-derived SiOC ceramic pyrolyzed at 1100 °C; (C) TEM image, with selected area electron diffraction (SAED) pattern shown in inset indicating a homogeneous amorphous structure; (D) solid state ²⁹Si NMR spectra, revealing mixed bonding between Si, O and C. Reprinted by permission from X. Wang et al.: ‘Additive manufacturing of ceramics from preceramic polymers: A versatile stereolithographic approach assisted by thiol-ene click chemistry’, *Additive Manufacturing*, 2019, 27, 80-90. Copyright 2019 Elsevier.

To continue, I focus on the representative SiOC ceramics fabricated from polysiloxane SPR212. As described above and as verified by TEM, the SiOC formed by pyrolysis at 1100 °C in flowing nitrogen is amorphous. Further insight into the SPR212-derived SiOC microstructure is provided by solid-state ²⁹Si-NMR characterization (Figure 36D). The characteristic peaks at chemical shifts of -114 and -14 ppm correspond to SiO₄ and SiC₄ units, respectively, and the peaks at -82 and -39 ppm can be assigned to mixed-bond SiO₃C and SiO₂C₂ units, respectively ¹²¹. Based on XPS measurements, the fabricated SiOC ceramic can be considered as consisting of 66.2 wt % SiO₂, 13.7 wt % SiC and 20.1 wt % free carbon. The fabricated SiOC parts exhibited a measured Archimedes

4.4 Additive manufacturing of PCP and their conversion to ceramics

density of 2.10 g/cm^3 , which approaches 97 % of the calculated theoretical density of 2.17 g/cm^3 assuming densities of 2.2, 3.1 and 1.45 g/cm^3 for amorphous SiO_2 , amorphous SiC and pyrolytic carbon, respectively ¹²². This confirms that the fabricated SiOC parts are near fully-dense with negligible pore volume. This is essential for ceramic materials, since cracks and pores act as stress concentrators under load and can initiate failures. As can be seen in the radiography images (Figure 34), SiOC components are free from observable internal cracks and closed pores. Here, 3D-printed cellular cubes of SiOC are completely dense and free of macrosized defects, as confirmed by the homogeneous X-ray absorption in the tomographic images of the diamond lattice (Figure 37A) and Kelvin cell (Figure 37E) structures. The corresponding SEM images (Figure 37B-D and F-H) demonstrate again the delicate microstructures and fine features with struts size down to $200 \mu\text{m}$, which can only be obtained via stereolithographic additive manufacturing with excellent printing resolution. Along the printing direction, the step-like surfaces are clearly visible which is related to the layer-by-layer printing process. In this work the layer thickness during printing is set to be $100 \mu\text{m}$ to yield rapid fabrication. At higher magnification, smooth glassy surfaces are observed, with no porosity. This is consistent with the radiography images and shows that high-quality ceramic components were fabricated in this work.

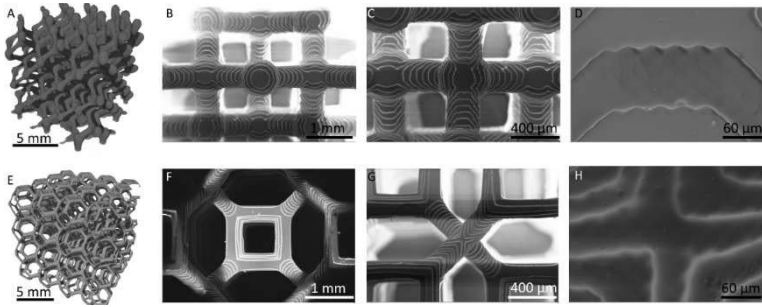


Figure 37. Morphology and microstructure of additively manufactured SPR212-derived SiOC: (A and E) tomographic images of the diamond lattice (A) and Kelvin cell (E) structures. The delicate design is perfectly replicated without any detectable flaws. (B-D, F-H) corresponding SEM images at higher magnification showing the step-like surfaces as well as the crack-free struts. Reprinted by permission from X. Wang et al.: ‘Additive manufacturing of ceramics from preceramic polymers: A versatile stereolithographic approach assisted by thiol-ene click chemistry’, *Additive Manufacturing*, 2019, 27, 80-90. Copyright 2019 Elsevier.

4.4.4 Mechanical properties of SiOC 2D honeycombs

The hardness and elastic modulus of the SiOC ceramics are evaluated in nanoindentation experiments (Figure 38). Figure 38A shows the 3D-printed honeycomb used for the nanoindentation measurements along with an AFM image of an indent. The typical load-hold-unload curve is shown in Figure 38B. 200 measurements were conducted to evaluate the reduced elastic modulus and hardness, as given in Figure 38C and D. Over a range of penetration depths, the mean values of the reduced Young’s modulus and hardness are found to be 106 ± 6 GPa and 12 ± 1 GPa, respectively. An earlier study showed that SiOC ceramics with lower O/C ratios behave similarly to amorphous-SiC materials, while the mechanical properties of SiOC with higher O/C ratio are similar to those in amorphous SiO₂¹²³. In the present work, the hardness and elastic modulus of AM-fabricated SiOC materials lie between the predicted limit of amorphous SiO₂¹²³ and amorphous

4.4 Additive manufacturing of PCP and their conversion to ceramics

SiOC¹²⁴ and are further in good agreement with reported values for silicon oxycarbide glasses with variable C/O ratio^{123, 125}.

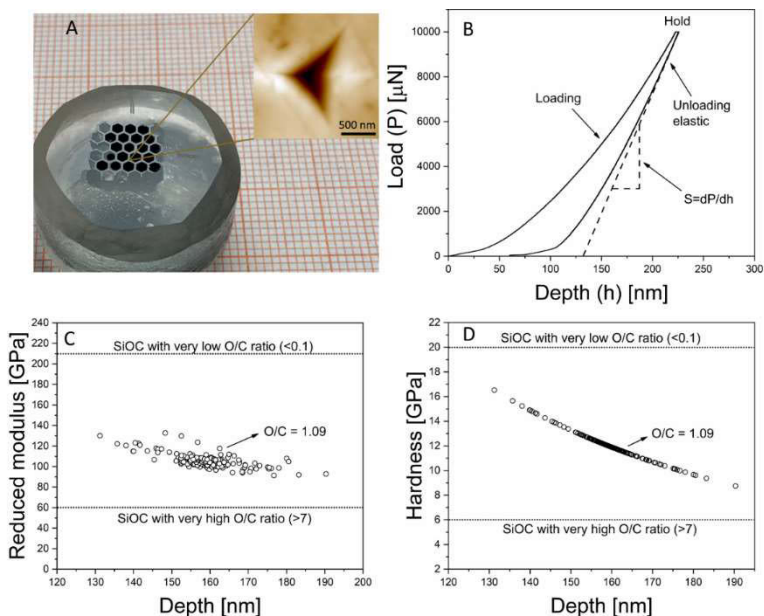


Figure 38. Results of nanoindentation tests performed on 2D honeycombs of additively-manufactured SPR212-derived SiOC. (A) A polished SiOC honeycomb imbedded in epoxy resin. Inset shows the AFM image of one indenter. (B) Load-Hold-Unload curve of one indenter. Elastic modulus is determined via the elastic unloading process. (C, D) Reduced modulus and hardness as a function of the penetration depth. 200 measurement results are shown here. Reprinted by permission from X. Wang et al.: ‘Additive manufacturing of ceramics from preceramic polymers: A versatile stereolithographic approach assisted by thiol-ene click chemistry’, *Additive Manufacturing*, 2019, 27, 80-90. Copyright 2019 Elsevier.

It is worth emphasizing that our fabrication method resulted in SiOC ceramics with comparable or even slightly better mechanical properties than those of SiOC glasses fabricated either via hot-pressing or via radio frequency (RF)-magnetron sputtering. Both of these methods could yield high surface quality SiOC components (bar and thin films) with minimized defects and pore volume.

4. Additive manufacturing of PDCs

Since our manufacturing methods allow for the fabrication of 2D and 3D periodic cellular structures, in the next step we evaluate the out-of-plane compression strength of 2D SiOC honeycombs as a representative example of a material with high strength to density characteristics, and apply Gibson and Ashby's model¹²⁶ to analyze these results. The honeycomb geometry is particularly strong when loaded along the main axis of the hexagonal prism (out-of-plane, X_3) compared to the in-plane directions (X_1 and X_2), as the thin cell walls are much stiffer under extension or compression than in bending. Therefore, honeycomb shapes are mostly used as cores in sandwich panels to provide high strength-to-weight ratios. Likewise, honeycombs made from ceramic materials are frequently used as catalyst supports, filtration membranes and components in heat exchangers due to their superior chemical and mechanical stability in harsh environments.

Figure 39 shows the corresponding stress-strain curves. 2D SiOC honeycomb structures fabricated in this work are found to exhibit a foam density of 0.61 g/cm³ and compressive strength of 216 MPa, as summarized in Table 18 and Figure 39. The SiOC honeycomb demonstrates linear-elastic behavior as well as catastrophic failure, which is accompanied by a sudden drop in the measured stress. The plateau presented in the stress-strain curves before failure is a result of the slight misalignments of load-bearing faces in the fabricated lattices, which in an ideal structure should be perfectly parallel, as well as an edge effect that, cell walls from internal to external can't fail simultaneously. Therefore, in our experiments the compressive strength is taken as the value at which this plateau occurs rather than the maximum crushing stress.

4.4 Additive manufacturing of PCP and their conversion to ceramics

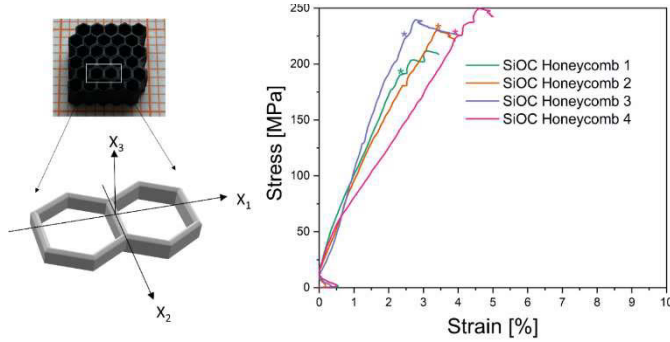


Figure 39. Left: Schematic representation of 2D honeycomb with a cellular density of 0.61 g/cm^3 of additively-manufactured SPR212-derived SiOC carrying loads on the faces normal to X_3 . Right: Measured stress-strain curves of fabricated SiOC honeycombs. Symbol “*” represents the first major failure of ceramic honeycomb. Reprinted by permission from X. Wang et al.: ‘Additive manufacturing of ceramics from preceramic polymers: A versatile stereolithographic approach assisted by thiol-ene click chemistry’, *Additive Manufacturing*, 2019, 27, 80-90. Copyright 2019 Elsevier.

Table 18. Detailed information of honeycombs utilized for compression tests and the obtained compressive strength and cell modulus of SiOC honeycombs.

Samples	Honeycomb1	Honeycomb2	Honeycomb3	Honeycomb4
Weight [g]	0.123	0.125	0.128	0.129
Length [mm]	8.57	8.57	8.69	8.70
Width [mm]	8.57	8.57	8.70	8.70
Height [mm]	2.78	2.78	2.78	2.78
Density [$\text{g}\cdot\text{cm}^{-3}$]	0.60	0.61	0.61	0.61
Compressive strength [MPa]	190	230	222	224
Cell modulus [GPa]	7.86	7.89	9.42	7.42

4. Additive manufacturing of PDCs

Gibson and Ashby's model relates the mechanical properties of a cellular solid with its relative density ρ_{relative} (which is the density ρ^* of the foam divided by the density ρ_s of the solid which the foam is made of) and its solid strength and bulk modulus (σ_s, E_s). The strength (σ) as well as the modulus (E) of the cellular material can then be expressed as follows:

$$\frac{\sigma}{\sigma_s} = C \left(\frac{\rho^*}{\rho_s} \right)^m \quad \text{Equation 8}$$

$$\frac{E}{E_s} = C \left(\frac{\rho^*}{\rho_s} \right)^m \quad \text{Equation 9}$$

where C is a dimensional constant and the exponent m depends on the cell morphology. In the case of a 2D honeycomb carrying loads on the faces normal to X_3 , Equation 8 and Equation 9 can further be simplified to ¹²⁷:

$$\frac{E}{E_s} = \frac{\rho^*}{\rho_s} \quad \text{and} \quad \frac{\sigma}{\sigma_s} = \frac{\rho^*}{\rho_s} \quad \text{Equation 10}$$

In this case the Young's modulus of the 2D honeycomb simply reflects the solid modulus scaled by the load-bearing area. Using Equation 10 with calculated relative density ρ_{relative} of 0.29 and the Young's modulus of 106 ± 6 GPa which is obtained from the nanoindentation experiments, we obtain 31 ± 2 GPa for the theoretical honeycomb stiffness. Because of the measurement error, which occurred when evaluating the true strain of SiOC honeycomb under compression, we shall not compare the measured Young's modulus with this calculated theoretical value here. The fact that the honeycomb's modulus measured in this work is significantly lower than the calculated theoretical value is caused by the unusual high strain (dP/h , displacement divided by sample height) of up to 3.5 % as seen in Figure 39, whereas for typical ceramic materials the strain to failure is typically less than 1 %. As shown in Figure 40, the walls

4.4 Additive manufacturing of PCP and their conversion to ceramics

of the SiOC honeycomb are imprinted into the steel plates during the compression test, since SiOC has much higher hardness than steel (1–3 GPa). The measured displacement is thus the sum of the deformation of the steel plates and the ceramic honeycomb. Therefore, the true displacement/strain is significantly overestimated and the measured elastic modulus is untrue and should not be used for evaluating the mechanical properties.

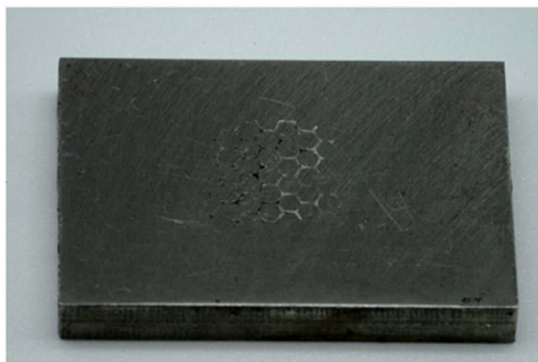


Figure 40. Image of the metal face sheet showcased apparent hexagonal scratches and ceramic residual after compression test due to the imprinting of SiOC ceramic into steel.

In Figure 41, SiOC honeycombs printed in this work are compared to natural and engineered cellular solids as well as other honeycombs made from SiOC⁸², SiOC nanocomposites¹²⁸, Al₂O₃^{129–131}, and SiC¹³². The silicon oxycarbide honeycombs fabricated in this work display an outstanding strength to density ratio that is significantly higher than other materials of similar density. Its absolute strength is also comparable with fiber-reinforced polymers and metal alloys. The compressive strength of 216 MPa is comparable to that exhibited by α -Al₂O₃ honeycombs of approximately twice the density and is around one order of magnitude higher than commercial SiC honeycombs. The silicon oxycarbide honeycombs fabricated in this work further demonstrate a higher compressive strength compared to SiOC honeycombs with the densities ranged from 0.5 to 0.8 g/cm³

4. Additive manufacturing of PDCs

reported in previous works (see e.g. ^{82, 128}). The exceptional performance of the additively-manufactured SiOC honeycombs is the result of their dense and defect-free structure, which was observed by radiography and SEM characterization. As shown in Equation 10, the strength of a cellular solid—whose cell walls display a stretch-dominated behavior—scales linearly with its relative density ¹³³. This behavior is represented as a line with a slope of 1 in the double-logarithmic strength-density plot. Accordingly, the theoretical compressive stress of cellular polymer-derived SiOC ceramics can be defined by these lines passing through bulk silicon carbide, silicon nitride and silica, which thus delineate the maximum obtainable performance for PDCs ¹³⁴. As can be seen, SiOC honeycombs in this work with a density of 0.6 g/cm^3 reach the theoretical compressive strength of silica-based materials while approaching the predicted theoretical value of silicon carbide and silicon nitride. Shifting the ceramics' compositions towards higher C to O ratios by choosing polymers of higher carbon content and avoiding oxidation can further boost its specific strength towards the theoretical limit of SiC. By utilizing polysilazane in an oxygen-free environment, silicon carbonitride ceramics can be obtained, offering further avenues towards high mechanical performance of printed cellular structures.

4.4 Additive manufacturing of PCP and their conversion to ceramics

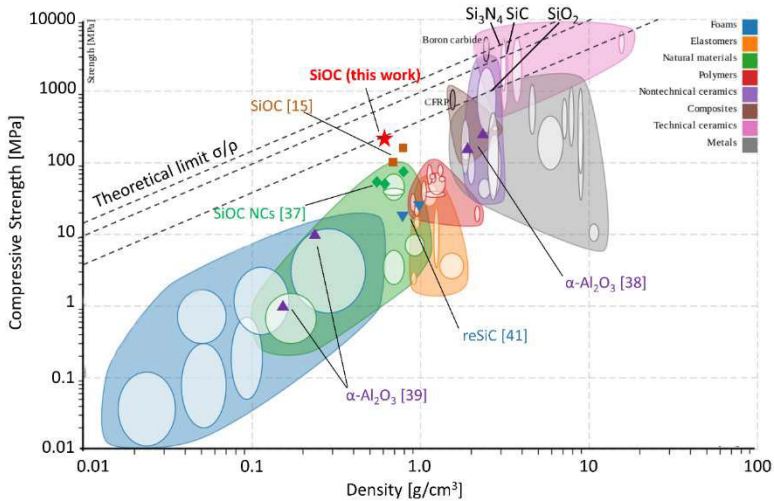


Figure 41. Strength-density Ashby chart for designing light strong structures. In this chart, our additively-manufactured SiOC honeycombs are compared to other ceramic (i.e. SiOC, Al_2O_3 , SiC) honeycombs as well as to other natural and technical materials. Figure and material properties are generated by Nicoguaro using JavaScript and D3.js¹³⁵, except the data points of different ceramic honeycombs, which were inserted manually from the corresponding references. Reprinted by permission from X. Wang et al.: ‘Additive manufacturing of ceramics from preceramic polymers: A versatile stereolithographic approach assisted by thiol-ene click chemistry’, *Additive Manufacturing*, 2019, 27, 80-90. Copyright 2019 Elsevier.

4.5 Summary

I have closely examined the utility of thiol-ene click chemistry towards additive manufacturing using preceramic polymers. We demonstrated a versatile stereolithographic manufacturing route whereby high performance polymer-derived ceramics are obtained with well-controlled geometry. The developed approach can be applied for the entire range of known PDC systems. For precursors to be used in thiol-ene click-assisted stereolithography they should exhibit an inorganic backbone, unsaturated carbon bonds and the photoinitiation of thiol radicals. High levels of hydrogenated groups

4. Additive manufacturing of PDCs

in precursors are detrimental, as the evolution of a significant volume of hydrogen gas during pyrolysis can cause failure under certain firing conditions. The photocurable preceramic polymers of this method are easily prepared and can be applied in any SLA/DLP printer, as well as in techniques like microstereolithography and two-photon polymerization to produce microstructures beyond the resolution limit of DLP techniques. The additively-manufactured polysiloxane-derived SiOC components fabricated here are nearly fully dense, achieving 97 % of the maximum theoretical density. 2D SiOC honeycombs with a cellular density of 0.61 g/cm^3 exhibit a compressive strength of 216 MPa, surpassing the performance of comparable porous ceramics and stretching the boundaries of material property space in terms of strength-to-weight ratio under compression. The presently developed methods represent a flexible and rapid route towards high-performance additively-manufactured polymer-derived ceramics that can find broad application in various engineering fields, particularly for load-bearing materials applied in harsh environments and high temperatures. With appropriate AM techniques, ceramic components can be produced with the developed methods across a range of length scales with high precision, thus representing a valuable new capability for industries such as aerospace, automotive, energy conversion and chemical engineering.

5 Cryo thiol-ene click chemistry assisted freeze casting of preceramic polymers

5.1 Process design

5.1.1 Overall approach

In this chapter a novel approach towards highly porous polymer-derived ceramics with well-controlled pore morphology is developed. It is based on freeze casting of preceramic polymer solutions assisted with cryo photopolymerization. During the process, the temperature of the polymer solution is lowered to induce phase separation between the solute and the solvent. This is also known as thermally-induced phase separation (TIPS) and is frequently utilized to produce porous polymer forms and membranes. The mechanical integrity of the utilized liquid preceramic polymer is obtained through a photopolymerization step under the frozen state, followed with solvent removal via sublimation to impart porosity. Then, thermal pyrolysis is utilized to convert the prepared preceramic polymer monoliths into Si-based ceramic materials. The whole fabrication process is schematically outlined in Figure 42.

The success of freeze-casting liquid preceramic polymer to produce highly porous ceramics relies greatly on the mechanical integrity (green strength) provided by means of binders or cross-linking reactions. In this work, UV thiol-ene polymerization in the frozen state is the key factor to polymerize liquid preceramic polymers into solid state with sufficient mechanical integrity as well as infusibility. When the freeze-dried green body is brought back to room temperature and further to the pyrolysis step, insufficient cross-linking of the preceramic polymer will lead to distortions or even

5.1 Process design

catastrophic collapsing of the produced polymer monoliths. Thus the pore channels and cell walls will not be preserved.

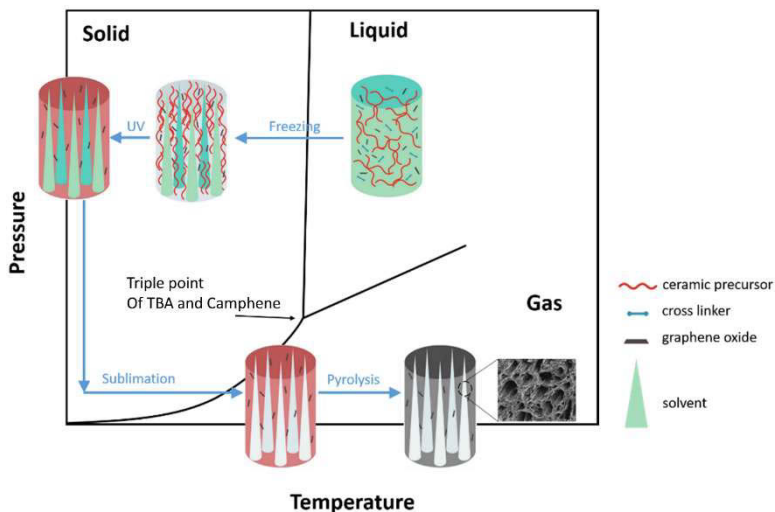


Figure 42. Schematic of cryo thiol-ene click chemistry assisted freeze casting of preceramic polymers.

5.1.2 Materials selection

To perform freeze casting with preceramic polymers, it is crucial to select suitable polymer systems and freezing vehicles, which fulfill their roles separately during the freeze casting process. The polymer system shall become the solid constituent of the freeze cast foam with sufficient mechanical integrity and the solvent—the freezing vehicle—will determine the produced pore morphology.

Polysiloxanes H62C and SPR212 are selected due to their stability in air and as they are representative preceramic polymers for the production of SiOC ceramics. The polycarbosilane SMP10 and polycarbosilazane Durazane 1800 are not considered for freeze casting, as they readily react with oxygen and moisture in air. To perform the photopolymerization in frozen state at $-20\text{ }^{\circ}\text{C}$, dithiol is

selected as a cross-linking agent and DMPA was chosen as photoinitiator. As shown in Chapter 3, the polysiloxane-2T-DMPA resin system demonstrates excellent versatility by showing efficient photocuring ability in the presence of organic solvents, which makes them ideal for a combination of freeze casting and cryo photopolymerization.

Not all organic solvents that can dissolve polysiloxane-2T-DMPA polymer mixtures are applicable in freeze casting fabrication. The utilized solvents should possess a high freezing point to facilitate freezing and the vacuum drying process. The additional photopolymerization in frozen state restricts the handling temperature of freeze cast samples further. Tert-butanol (TBA) and camphene, two conventional freeze casting solvents, are utilized due to their high melting temperature of about 26 °C and 51 °C, respectively. In addition, TBA and camphene also demonstrated excellent solubility with polysiloxane and hexane 2T.

The addition of fillers can greatly influence the pore morphology and microstructure of the resulting freeze cast samples. Graphite oxide (GO), which is synthesized through oxidation of graphite using a strong oxidizing agent, is introduced in tert-butanol and exfoliated to graphene oxide via sonication due to its expanded layer separation and hydrophilic property. The prepared GO/TBA suspension is subsequently mixed with the polysiloxanes. The original purpose of incorporating GO in the preceramic polymer is to enhance the mechanical strength and electrical conductivity of produced porous ceramic monoliths, as GO will be thermally reduced to graphene platelets during the pyrolysis and serve as reinforcing units embedded inside the ceramic matrix. Nonetheless, completely different pore morphology is observed when using GO as filler materials, which will be intensively studied in the next section. In addition to GO, nano-sized silicon dioxide powder was incorporated into the preceramic polymer solution for freeze casting, as they can be selectively etched away via a wet etching process after pyrolysis of the resulting monoliths, and can serve as a secondary sacrificial template in the production of highly porous ceramics. In the

5.1 *Process design*

production of porous carbon-based catalyst supports, nano-sized silicon dioxide powder or aqueous suspensions are frequently employed to produce mesopores through HF etching. The same principle will be applied in this work to produce freeze cast SiOC/SiO₂ ceramic composites, followed with HF etching to remove nano-sized silica powder or domains. As a result, ceramic monoliths with multi-scale porosity were fabricated via this route. This work will be described in Section 5.3.

5.1.3 Unidirectional freeze casting set up

The controlled directional freezing of prepared preceramic polymer solution is carried out in a home-made freeze casting set up as shown in Figure 43a. It consists of a brass rod which sits inside a stainless container filled with liquid nitrogen, and a heating element with a thermocouple. This set up allows the surface temperature of the brass rod to decrease from room temperature to -120 °C in a controlled manner, thus allowing a more homogeneous growth of the solidified crystals. A cylinder-shaped acrylate glass mold with an inner diameter of 10 mm and height of 20 mm is attached to the brass rod for the casting of prepared solutions. Thus the freeze-cast samples have the same cylinder shape.

The rapid directional freezing is carried out with a similar and simpler self-made set up (see Figure 43b), in which the heating element was removed. Instead, the brass rod that sits below the same acrylate glass mold is simply placed inside a Teflon container, and the filling of liquid nitrogen leads to the instant cooling of its overall temperature. This set up allows a simpler and faster complete solidification process within 10 min, where the cooling rate is undetermined and believed to be extremely high.

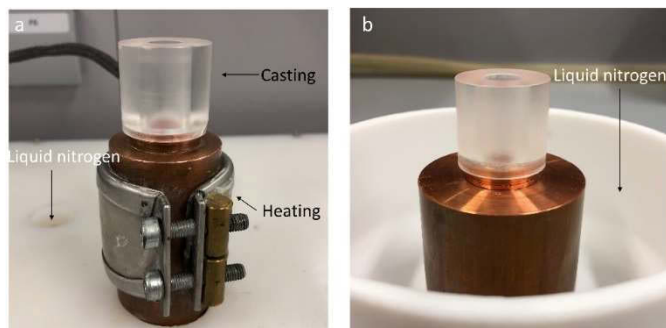


Figure 43. Self-made freeze casting set up with (a) controlled freeze rate and (b) rapid freezing.

Frozen samples are subsequently demolded from the acrylate glass and transferred to a $-20\text{ }^{\circ}\text{C}$ freezer, followed with cryo UV illumination with a UV illuminator, whose specifications are described in Chapter 3 Table 8.

5.2 SiOC/GO shells

In this part the fabrication of macroporous ceramic monoliths from liquid phase preceramic precursor (polysiloxane H62C) by freeze-casting assisted with UV-initiated thiol-ene click reaction is demonstrated. Furthermore, the formation of a ceramic shell—a monolith with open cylindrical (tubular) shape with an axial hole—freeze cast from a preceramic polymeric solution with graphene oxide (GO) filler is discussed. In the latter part of this work, the formation mechanism of such ceramic shells will be studied and explained.

5.2.1 Synthesis of samples

Three compositions based on polysiloxane H62C without (sample HG0) and with graphene oxide filler (samples HG1 and HG2) are investigated in this part. In a typical preparation route, polysiloxane H62C is dissolved in tert-butanol at a polymer weight loading of

5.2 SiOC/GO shells

20 %, followed by adding DMPA in a 1:100 weight ratio regarding the H62C content and hexane dithiol in a 1:10 weight ratio to H62C. The solution is mixed for 10 min at room temperature until a clear transparent solution is obtained. Freeze cast samples produced from H62C solution without graphene oxide filler are denoted as HG0. For the preparation of HG1 and HG2 samples, graphene oxide powder is initially added to tert-butanol with concentrations of 0.5 mg/ml and 1 mg/ml, respectively, followed with mild stirring for 30 min and 1 h ultra-sonication to exfoliate the graphene oxide powders. The resultant GO/TBA suspension is used to dissolve H62C, DMPA and hexane dithiol as described in the preparation of HG0. The compositions of prepared solution and suspension is shown in Table 19.

Table 19. Compositions applied for freeze casting.

	HG0	HG1	HG2
H62C [g]	2	2	2
DMPA [mg]	20	20	20
2T [g]	0.2	0.2	0.2
TBA [g]	8	8	8
GO [mg/ml]	0	0.5	1

As shown in Figure 44, the polymer solution of H62C dissolved in TBA has a completely different appearance compared to H62C dissolved in GO/TBA suspension. While the pure H62C solution looks clear, colorless and is optically transparent, the GO/TBA suspension is of a dark brown color which can be attributed to the intrinsic appearance of GO, as the color of GO can differ from light yellow to brown depending on the degree of oxidation.

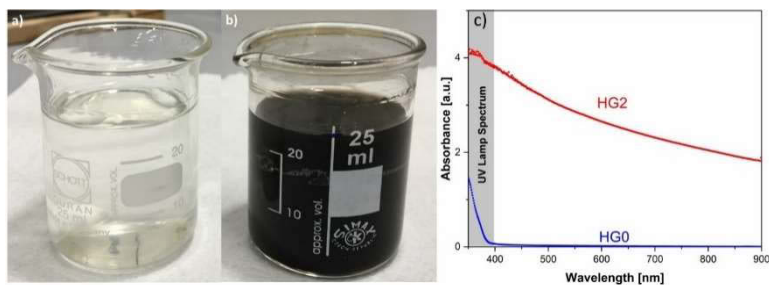


Figure 44. Optical images of a) H62C/DMPA/TBA (HG0) solution and b) H62C/GO/DMPA/TBA (HG2) suspension with corresponding UV-Vis absorption spectra shown in c).

In conventional freeze casting technique, the optical properties of the solutions / suspensions do not affect the final achievable porous structures. However, the additional cryo photopolymerization step required in this work to cross-link the liquid preceramic polymer will be greatly affected by the light absorption in the prepared solution / suspension. As shown in Chapter 3, the penetration depth of incident light is reduced in the presence of photoabsorbers / light absorbing polymers, thus leading to the reduction of photopolymerization depth in the materials.

UV-Vis spectroscopy is used to evaluate the absorption of starting solution / suspension as demonstrated in Figure 44c. The clear H62C/TBA solution (HG0) only absorbs incident light below 400 nm due to the absorption of DMPA used as photoinitiator. The penetration depth of incident light within the operational wavelength of the UV lamp is therefore solely depending on the concentration of the utilized photoinitiator. In contrast, even a low concentration of GO (1 mg/ml) in H62C/GO suspension results in high absorption in visible and UVA ranges, acting as photoabsorber in these materials.

Freeze casting of HG0, HG1 and HG2 are carried out with controlled directional freezing as described in Section 5.1.3. In a typical freeze casting process, the prepared starting solution or suspension is cast into the acrylate glass mold, followed with decreasing the temperature of the surface of brass rod from 25 °C to

5.2 SiOC/GO shells

-120 °C with a constant cooling rate of 6 °C/min. The solidification of the solvent generally takes 40 min to complete. Afterwards, frozen samples with glass mold is allowed to rest in a -80 °C freezer for half an hour. Then they were transferred to a -20 °C freezer and the frozen samples were carefully demolded from the acrylate glass mold, followed with cryo UV illumination with a UV lamp (see Figure 45). The frozen samples are allowed to rotate 180 ° after 30 min illumination to ensure even photopolymerization. The whole cryo UV exposure takes one hour.



Figure 45. Optical image demonstrating cryo photopolymerization of frozen HG0 (white) and HG2 (black) samples.

The cross-linked samples are subsequently transferred to a freeze drier (Christ Gamma 2-20), which operates at -80 °C and 0.13 mbar pressure, to allow the sublimation of solidified TBA or camphene crystals for 3 days to obtain foam-like monoliths that are shown in Figure 46. Liquid H62C is successfully cross-linked into a foam-like solid via the thiol-ene click reaction with dithiol in the frozen state at -20 °C. This result confirms the feasibility of the approach developed here, showing that solution-based freeze casting assisted with additional cryo photopolymerization can be used as an effective approach to freeze cast liquid monomers or polymers, which are so far considered as very challenging in conventional freeze casting techniques.

Fourier-transform infrared spectroscopy (FTIR) confirms the thiol-ene click reaction between dithiol and H62C by evidently showing the reduction of absorption bands of the corresponding

5. Freeze casting of PDCs

vinyl groups of H62C at 1407 cm^{-1} ($=\text{CH}_2$ scissoring) and 1597 cm^{-1} ($\text{C}=\text{C}$ stretch) after UV illumination in frozen state (see Figure 46 left a,b). This cryo photopolymerization result is very similar to the photocuring behavior of preceramic polymer resins at room temperature as demonstrated in Chapter 3. Despite the successful cross-linking, fabricated H62C and H62C/GO monoliths barely maintain their original form, which is determined by the cylindrical cast mold, and show some significant distortion and shrinkage after the vacuum drying process as observed in Figure 46 right. This is likely due to the H62C polymer containing less vinyl groups compared to SPR212 and Dura1800. Therefore, H62C-thiol-ene polymerized samples are not mechanically stable enough to withstand the stress development during the solvent removal process. To overcome this problem, the utilization of preceramic polymers which are enriched with vinyl groups (e.g., SPR212 and Durazane 1800) or additional organic binders could be applied to enhance the mechanical stability of the specimens.

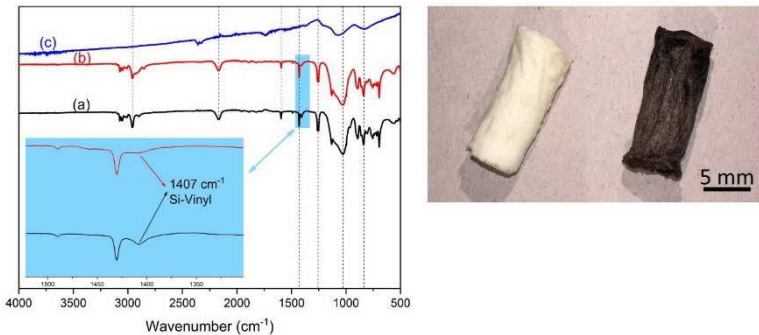


Figure 46. Left: FTIR spectra of (a) liquid polysiloxane H62C, (b) freeze cast H62C monolith after cryo UV polymerization and vacuum drying and (c) H62C-derived SiOC after pyrolysis. The decreasing intensity of Si-vinyl absorption bands is shown in inset. Right: Optical image of freeze cast H62C foam (white) and H62C/GO foam (brown) after freeze drying.

The freeze cast polysiloxane monoliths are subsequently pyrolyzed at $1100\text{ }^{\circ}\text{C}$ (with heating profile B as described in Chapter

5.2 SiOC/GO shells

2) to complete the polymer-to-ceramic conversion, as confirmed by the FTIR-ATR spectroscopy (Figure 46). Since the FTIR spectra of pyrolyzed HG0, HG1 and HG2 are exactly the same, only the spectrum of HG0 is shown here. The decomposition and ceramization of the polysiloxane during pyrolysis is indicated by the vanishing of absorption bands at 1250, 1430, 2170 and 2958 cm^{-1} , characteristic to Si-CH₃, Si-phenyl, Si-H and C-H bonds, respectively. The absorption spectrum of the pyrolyzed specimens is characterized by a broad absorption band around 1100 cm^{-1} attributed to the Si-O-Si bonds and a band around 800 cm^{-1} which is attributed to Si-C bonds, demonstrating the pyrolyzed ceramic as SiOC.

5.2.2 Composition and structure

Figure 47 shows optical and SEM images of pyrolyzed SiOC samples fabricated from pure polysiloxane (HG0) as well as from polysiloxane-GO suspensions (HG1 and HG2). The SiOC cylinder monolith formation is accompanied by approximately 40 % of linear shrinkage due to the decomposition of polysiloxane H62C and the further ceramization process which leads to the density increase. The well-controlled macroporous structure produced via freeze casting is preserved in the ceramic monoliths. As shown in Figure 47a, the pore channels are highly aligned to the temperature gradient and the pore shapes are prismatic, replicating the controllable growth of TBA crystals during the directional freezing. The obtained pore morphology is in good agreement with previous works^{136,137} on using TBA as a template in freeze-casting routes, and demonstrates the applicability of the freeze casting-assisted with cryo photopolymerization approach.

Addition of small amounts of GO into the H62C-TBA-solution with subsequent freeze casting and photopolymerization led to the formation of a shell-like architecture in the pyrolyzed GO/H62C samples (see Figure 47b and c). Both HG1 and HG2 monoliths possessed an open cylindrical (tubular) shape with an axial hole, in which the sizes of the axial hole increased with increasing GO

concentrations, and the wall thickness decreased with increasing GO concentration. Both HG1 and HG2 samples possessed almost the same outer diameter. The diameter of the cylindrical hole in the HG2 sample is approximately three fourths of the sample outer diameter. The HG2 sample with the higher GO amount has a wall thickness of 0.88 mm, which is 42 % thinner than the wall thickness of HG1. More importantly, despite the significant change in the bulk structure, the directional pore channels can still be observed inside the cylinder walls of both samples (Figure 47b, c). They possess the identical pore morphology and almost the same pore size as pure H62C freeze cast sample, which indicates a successful freeze casting as well as polymer-to-ceramic transformation while preserving the fabricated pore structures in the outer shell of the samples.

X-Ray Computed Tomography (μ CT) is utilized to reveal more information about the microstructure of these ceramic shells. As seen in Figure 48, the HG2 ceramic shell has a relatively uniform wall thickness. The ceramic wall consists of two phases with different morphologies, which are highlighted with different colors in the reconstructed image from X-Ray tomography. The outer part of the shell possesses an open cellular structure, which is attributed to the freeze casting technique and is demonstrated in the SEM images previously. The inner part of the shell represents as a dense coating without aligned porosity covering the inner side of the shell wall, its thickness is significantly smaller than the porous part of the shell.

5.2 SiOC/GO shells

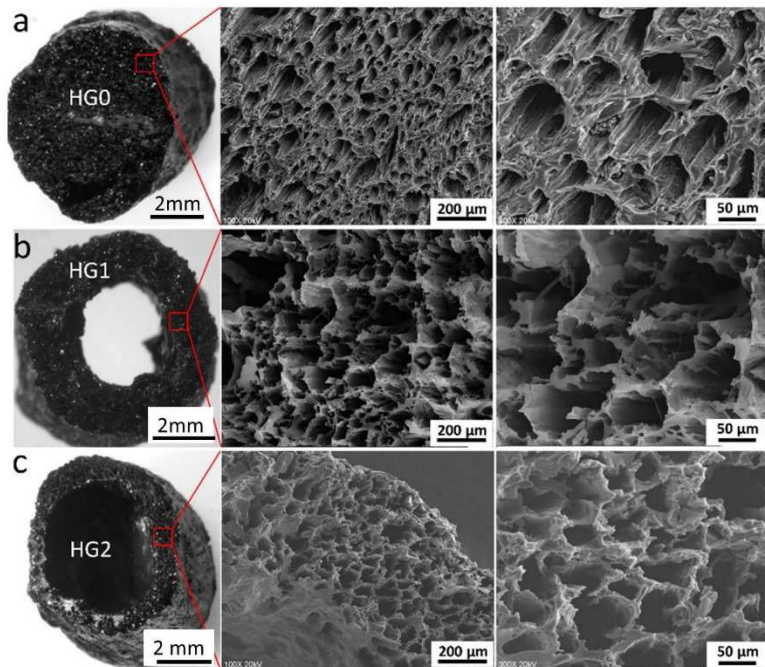


Figure 47. Optical (left) and SEM (middle and right) images of (a) SiOC monoliths (sample HG0 and (b, c) SiOC/GO shells (samples HG1 and HG2) displaying aligned pores in the specimens.

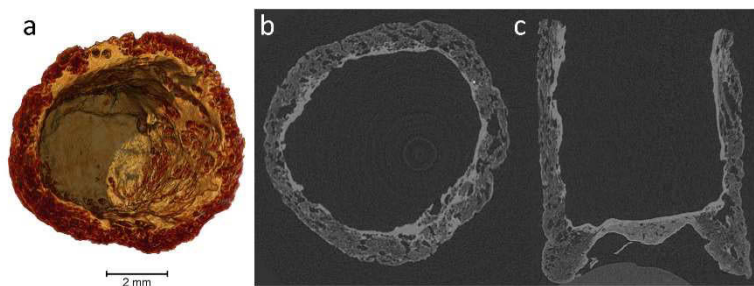


Figure 48. X-Ray Computed Tomography (μ CT) images demonstrate the two-phase composition of HG2 samples.

The microstructure and chemical composition of the ceramic walls are further analyzed with Field Emission-Electron Probe Microanalysis (FE-EMPA). The backscattered electron images (BSE) (Figure 49a, b) are in agreement with the tomography pictures, demonstrating that the shell consists of macroporous outer surface and nonporous inner walls.

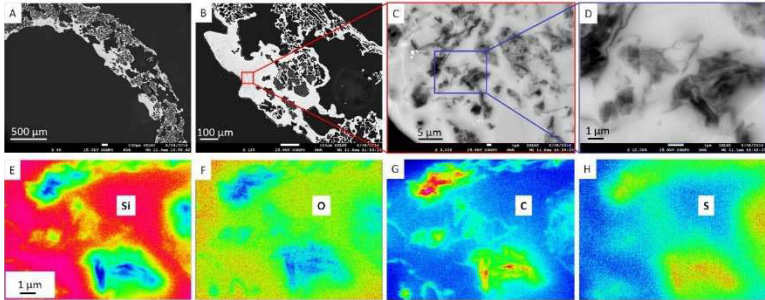


Figure 49. (A-D) SEM images in BSE mode of the sample HG2. (E-H) FE-EMPA spectral maps of the Si, O, C and S from the part shown in D (which are slightly rotated clockwise).

The elemental composition is analyzed at six positions uniformly chosen across the sample by EMPA and shown in Table 20. The sample has similar chemical composition independent of the measurement position (whether external part or internal part of the sample) consisting of an average of 34.5 wt% silicon, 28.9 wt% oxygen, 36.0 wt% carbon and 0.6 wt% sulphur. Nonetheless, the BSE images (compositional contrast) with higher magnification (Figure 49C, D) showed that the specimen is inhomogeneous at nanoscale. The elemental analysis of the dark areas (Table 20, position Nr. 7) reveals that they consist of 10 wt% more carbon and 1 wt% more sulphur. The element mapping (Figure 49E, F, G, H) of Si, O, C and S further confirms the excess of carbon and sulfur in these areas, while Si and O are depleted. This is attributed to the presence of the the agglomerated product of a reaction between dithiol and graphene oxide embedded in the SiOC matrix.

5.2 SiOC/GO shells

Table 20. Chemical composition of the HG2 sample analyzed by FE-EMPA. Position numbers 1 to 6 are selected uniformly at low resolution throughout the whole sample at macroscale, whereas position 7 corresponds to local inhomogeneity seen as dark areas in Figure 49 C, D.

Nr.	Position in sample	C [wt%]	O [wt%]	Si [wt%]	S [wt%]
1	Uniformly distributed	36.5	27.7	35.0	0.8
2		35.1	28.7	35.6	0.6
3		36.7	32.0	30.9	0.4
4		37.0	27.7	34.9	0.4
5		35.4	29.6	34.3	0.7
6		35.5	27.9	36.0	0.6
Average from (1-6)		36.0	28.9	34.5	0.6
7	precipitates	45.7	25.3	27.3	1.7

Transmission electron microscopy (TEM) is further utilized to characterize this carbon- and sulphur-rich area, where the presence of crystalline areas is clearly identified with bright regions as seen in the dark-field images (Figure 50a). The bright-field (BF) high-resolution imaging (Figure 50b, d) together with selected area electron diffraction (SAED) further identify the crystalline area as a graphitic structure based on the lattice spacing d_{002} of 0.37 nm. In the SiOC matrix, the BF-image (Figure 50) and SAED show a homogenous contrast indicating the amorphous nature of the matrix. Therefore, it can be concluded that the graphitic precipitates originate from the GO added instead of phase separation of the SiOC matrix. The SiOC ceramic obtained after pyrolysis at 1100 °C is amorphous, as demonstrated, with added GO being reduced to rGO and becoming crystalline graphite with an estimated thickness of 25-40 nm. It is noteworthy to mention that the morphology of these areas is highly crumpled and warped, which is also consistent with the reported structure of rGO sheets embedded within PDC matrices¹³⁸.

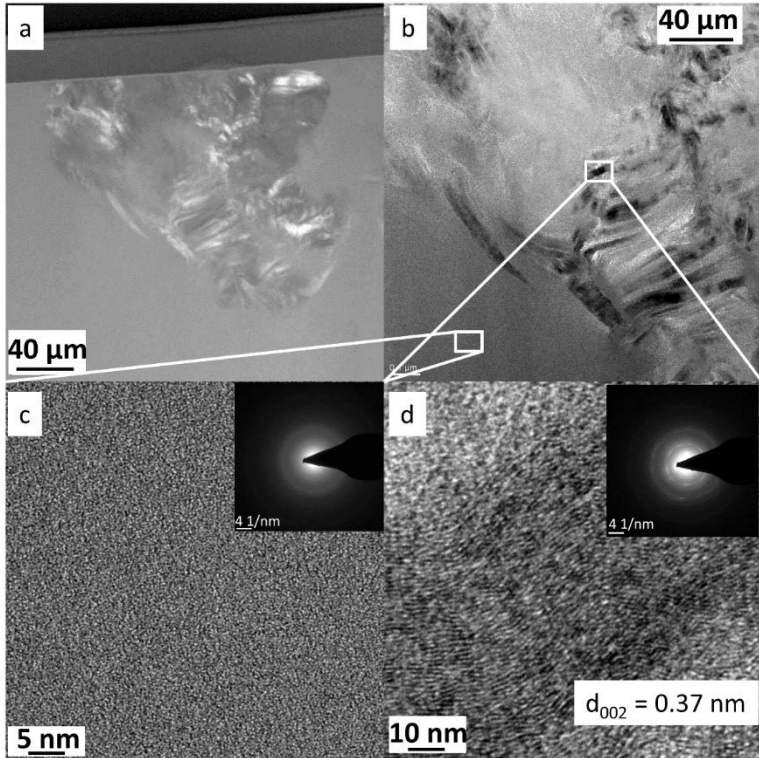


Figure 50. TEM (a-d) images in the dark-field (b) and bright-field (c, d) mode and selected area electron diffraction patterns shown as insets in c and d.

The XRD characterization (see Figure 51) further confirms the amorphous state of obtained SiOC-based ceramics, as there are no noticeable diffraction reflexes in the HG0 sample, which is typical for PDCs synthesized at 1100 °C. In contrast, the sample HG2 with the highest amount of incorporated GO demonstrates a tiny reflection attributed to the graphite (002), which is consistent with the TEM characterization. In the HG1 sample, the graphite reflection is not observed, likely due to the very small amount of GO which is under the detection limit of the XRD characterization.

5.2 SiOC/GO shells

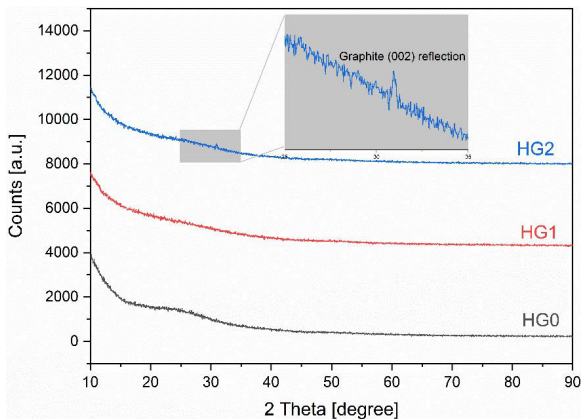


Figure 51. XRD diffraction patterns of HG0, HG1 and HG2 samples. The inset displays a tiny reflection in HG2 attributed to the graphite (002) (PDF 041-1487)

5.2.3 Mechanism of axial hole formation in SiOC/GO shells

In the following study, the focus is on rGO-SiOC cylindrical shell structures (samples HG1 and HG2) with radial density gradients. Two questions are addressed: first, what is the mechanism of void formation, and secondly, what are the two co-existing phases in the shell walls observed in μ CT images.

By examining the weight after vacuum drying and pyrolysis, freeze-cast samples HG0 and HG1/HG2 produced with and without GO demonstrate approximately the same weight losses (approximately 88 %), which are consistent with the ideal mass losses expected from the removal of solvent and the polymer-to-ceramic conversion of H62C polysiloxane. This suggests that the axial void is not created by material loss during the drying or pyrolysis steps but is probably attributed to the spatial redistribution of the preceramic polymer and pores.

To investigate the formation mechanism of the void, radiography images of the HG0 and HG2 samples are collected after each step of the fabrication route, namely directional freezing, UV-

polymerization and solvent sublimation. As seen in Figure 52a, the longitudinal section images of samples with and without GO show visually no difference after the directional freezing, suggesting that the GO addition does not alter the solidification of TBA and the dissolution of H62C. Both frozen samples demonstrate homogenous microstructure and no sign of agglomerated TBA crystals in the middle of the sample. The TBA crystals appear in the radiographic images as grey lines aligned to the freezing direction and represent the potential pore arrangement. As a conclusion, the void formation could not be caused by the phase separation in the solution as well as in the frozen state.

After UV-illumination, the outer shells of both samples appear to be more transparent in the radiographic images (see Figure 52b) indicating lower X-ray absorbance compared to the inner part of the samples. This is likely due to a slight but noticeable sublimation of TBA crystal during the cryo photopolymerization step due to its relatively large vapor pressure. Reaction heat originating from the thiol-ene click reaction initiated by UV illumination facilitates the sublimation process of TBA crystals in the outer shell of the samples as well. As a result, the outer shell mostly consisted of cross-linked polymer, compared to the inner part which is still a mixture of TBA crystals and polysiloxane. After complete sublimation of the TBA crystals (Figure 52c and d) the shell-like structure becomes apparent in the HG2 specimens. The cross-sectional radiographic image of the HG2 sample displays the formation of the axial hole, while the longitudinal one indicates that the hole is enclosed by a solid shell. In contrast, the HG0 sample fabricated from polysiloxane without GO exhibits a non-hollow structure, with the cross-linked polymer distributed homogeneously inside the whole specimen volume. This result further confirms that GO plays a determining role in the formation of cylinder shell-like structures with an axial hole positioned in the center.

5.2 SiOC/GO shells

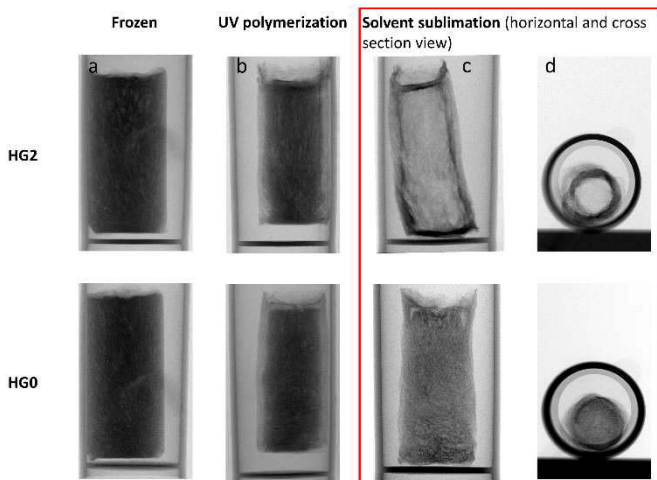


Figure 52. The microstructure samples without (HG0) and with GO (HG2) after each processing step documented by radiography images. The images in (d) are a cross-sectional view of samples in (c).

In-situ radiographic investigations are carried out on HG0 and HG2 samples during the sublimation step to monitor the formation mechanism of this axial hole. The results of these investigations are demonstrated as a selection of representative radiography images (see Figure 53), which are captured every 10 seconds during the solvent sublimation process.

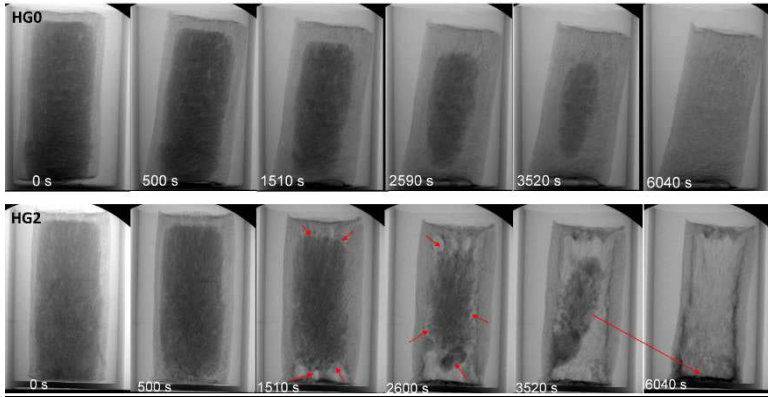


Figure 53. In situ radiography images captured during the vacuum drying of frozen samples with (HG2) and without GO (HG0). Red arrows indicate the interface where the cross-linking of the polysiloxane H62C is insufficient.

As observed in the radiography images of HG0, the darker area, where TBA crystal and polysiloxane are densely packed together, vanished gradually until the end of the drying process. This observation indicates a uniform sublimation of TBA crystals from the outer towards the inner volume of the specimen, while cross-linked preceramic polymer remains unaltered. Consequently, a highly-porous polysiloxane monolith is formed, with aligned pore channels following the directional growth of TBA crystals. In contrast, the vacuum drying of the HG2 sample containing GO proceeds completely differently. The continuous sublimation of the TBA crystals leads to the appearance of several interfaces, as indicated by the red arrows in Figure 53, where the polysiloxane and TBA mixture is being detached from the outer part of the monolith. Further vacuum drying results in pull-off and detachment from the outer wall. Eventually, the material in the center collapsed and fell to the bottom of the sample due to gravitational force, thereupon creating a hollow cylinder with an axial hole positioned in the middle.

UV-Vis absorption spectra of prepared H62C/TBA solution and H62C/GO/TBA suspension demonstrate a significant difference regarding the absorption of UV light, since dispersed GO

5.2 SiOC/GO shells

platelets absorb the incident light strongly. The successful freeze casting of HG0 sample from H62C solution indicates that UV light can penetrate through the whole 10 mm-thick sample and trigger the stepwise proceeding thiol-ene click reaction. Nonetheless, the presence of GO changes the UV polymerization process dramatically. GO platelets dispersed in the TBA solution strongly reduce the penetration depth of the incident UV light, by evidently demonstrating high absorbance throughout the visible and UVA ranges in the UV-Vis spectra of HG2 suspension compared to HG0 solution. The UV light can correspondingly only reach the external segment of the freeze cast sample, while leaving the internal part unilluminated and non-polymerized. As displayed in Figure 54b, the FTIR spectra show an almost complete disappearance of the characteristic peak at 1407 cm^{-1} (attributed to the C=C bonds) in the outer surface, while the intensity of this peak has only been slightly reduced in the inner walls, indicating reduced cross-linking towards the middle of the specimen. By adjusting the GO concentration in TBA solution, it is possible to control the degree of cross-linking and in this way manufacture graded architectures. The degree of cross-linking can also be monitored through the conversion of vinyl groups in preceramic polymers. In a control experiment by utilizing 10 mg/ml GO/TBA suspension as solvent for the freeze casting of H62C, only a thin layer of the frozen body was polymerized even after up to 24 hr of UV irradiation. As seen in Figure 55, the resultant polysiloxane monolith failed to sustain its original shape and demonstrated an unsuccessful freeze casting result.

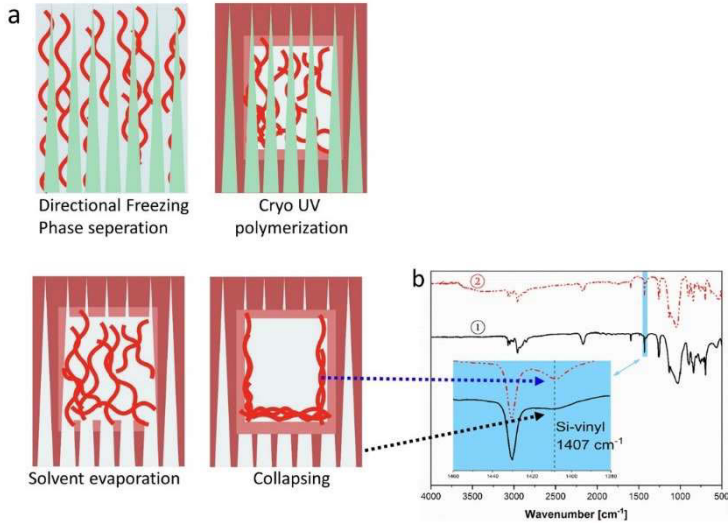


Figure 54. (a) Two dimensional schematic illustration of GO containing samples after each freeze casting step. Red and worm-like polymer chain represents the original preceramic polymer, while solid red areas represent the cross-linked interconnected region. TBA crystals are shown as prisms in green. (b) FTIR spectra of the internal (a) and external (b) segments of the freeze cast and dried HG2 samples, while the internal part still exhibits clear Si-vinyl absorption band.

Therefore, this unique shell-like structure is caused by insufficient photopolymerization of preceramic polymers located in the center of the sample where incident UV light cannot reach. The schematic representation of the void formation is illustrated in Figure 54a. During the cryo UV polymerization process, the liquid polysiloxane in the center of the specimen remains in a non- or less-cross-linked state, and is supported mechanically by the surrounding TBA crystals. Low temperature helps to preserve their shape as well due to the increased viscosity of liquid H62C. Nonetheless, during the vacuum drying process, TBA crystals start to sublime from the outside to inside, and will eventually reach the area where H62C is not polymerized. As a result, the H62C begin to lose their mechanical integrity and flow due to the gravitational force as well as the increased temperature, which leads to a decrease in viscosity.

5.2 *SiOC/GO shells*

Eventually parts of the liquid polymer will remain adhered to the wall, while most of it will collapse and fall down to the bottom of the sample as shown in Figure 48a. In the following pyrolysis step, the two-phase-containing ceramic shell, as seen in the previous tomography imaging, is thus derived from this unique microstructure. Insufficiently cross-linked H62C adhering to the inner surface converts into a thin dense SiOC inner coating, while the cross-linked outer part transforms into porous walls with aligned pores representing the morphology of the grown TBA crystals.

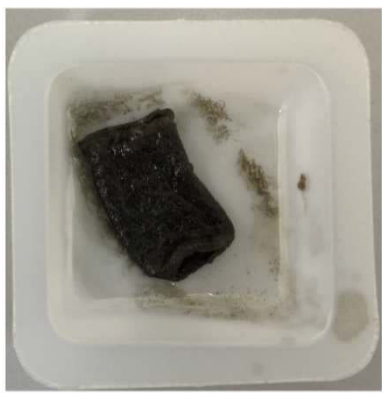


Figure 55. Optical image of freeze cast specimens derived from H62C dissolved in a 10 mg/ml GO/TBA suspension confirming that the cross-linking is solely restricted to the external part of the sample.

5.2.4 Summary

In this work, a novel approach based on the combination of freeze casting and frozen photopolymerization is utilized for the production of porous polymer-derived ceramic foams. Pre-ceramic polymer solutions were prepared and cast into a cylindrical mold and subsequently exposed to directional solidification. The thiol-ene click reaction was selected to cross-link the pre-ceramic polymer at relatively low temperatures due to its high curing efficiency and versatility in different chemical and physical environments.

Experimental results showed that the freeze casting of liquid preceramic polymer through this approach was successful and solid gel-like polymer foams can be obtained. It proved that free radical initiated thiol-ene click reaction can effectively cross-link the vinyl-containing liquid preceramic polymers at low temperatures, and allows to preserve their shape during solvent removal, retaining the pore morphology in the post-processing step and pyrolysis.

The complete photopolymerization of the whole frozen cylindrical samples relies on the sufficient penetration depth of incident UV light to reach the middle of the sample. Therefore, weak absorption of utilized freezing liquid and preceramic polymers regarding UV light is preferred to allow a high penetration depth. If the frozen photopolymerization process is altered by the presence of photoabsorbers (in this case GO), unique ceramic shells of open cylindrical (tubular) shape with an axial hole were obtained. Extensive in-situ radiography studies using X-ray imaging led to the conclusion that the axial hole is caused by non-polymerized polysiloxane, which flows due to the gravitational force when TBA crystals are sublimated and temperature increases. It was proven that GO strongly impedes the thiol-ene crosslinking reaction towards the center of the frozen sample and prevents the formation of form- and shape-stable monoliths by strongly absorbing the incident UV light. HG1 samples with half the concentration of GO/TBA suspension compared to HG2 demonstrated thicker shell walls and a narrower axial hole, since the smaller amount of GO present allows a deeper UV polymerization depth. Therefore, it is reasonable to assume that it is possible to fine-tune the shell thickness as well as the hole size by adjusting the GO amount in the specimens, which subsequently alters the penetration depth of the UV light.

5.3 SiOC and SiOC/SiO₂ foams with multiscale hierarchical porosity

5.3.1 Synthesis of samples

In the previous section, the concept of combining the freeze casting technique with cryo photopolymerization is successfully proven. The developed approach is utilized to produce polymer-derived ceramics with well-controlled pore morphology. Nonetheless, the freeze cast H62C samples demonstrate relatively low mechanical stability and noteworthy shape distortions after the solvent sublimation leading to deformation of the ceramic sample. This is caused by low amounts of vinyl groups in the preceramic polymer H62C, which strongly influences the crosslinking degree by thiol-ene click chemistry. Therefore, a mixture of H62C and SPR212 polymers in a weight ratio of 1:1 is employed to enhance the mechanical stability of cross linked samples, since SPR212 polymer demonstrates a higher cross-linking degree than H62C (see Chapter 3 for further discussion). The composition of samples studied in this chapter is given in Table 21.

To prepare the samples, polysiloxanes H62C and SPR212 in the weight ratio 1:1 are dissolved in the solvent (TBA or camphene), followed with the addition of DMPA and dithiol in a 15:100 weight ratio to the polysiloxane mixture. The mixture is stirred to obtain a clear solution. For SiO₂-containing samples, two silica powders with different particles sizes are employed, with particles around 40 nm (OX50-40) and between 5 to 15 nm (SA-15). The information of particle size is from the producer. First, SiO₂ powder is slowly added to TBA upon stirring followed by ultra-sonication for 1h to break down the agglomerates to achieve a weight ratio of SiO₂:H62C/SPR212 of 1:4. Then the SiO₂/TBA suspension is utilized to dissolve H62C/SPR212 mixture, DMPA and dithiol as described above. Due to their hydrophilic nature, both silica nanopowders can be easily dispersed and de-agglomerated in TBA solution by ultrasonic treatment.

The prepared solutions / suspensions are freeze cast in the rapid freezing set up as described in Section 5.3. The acrylate glass mold is additionally protected with a teflon cylinder from radial cooling due to the evaporation of liquid nitrogen. The complete solidification of samples occurs within 10 min. Subsequently, the same procedures—cryo UV polymerization followed with freeze drying and subsequent pyrolysis in N₂ atmosphere—which have been applied to the preparation of HG0, HG1 and HG2 monoliths and are described in Section 5.2.1, are applied to produce H62C/SPR212/dithiol derived SiOC and SiOC/SiO₂ monoliths.

Table 21. Composition of samples studied in this chapter.

	Cam30	TBA30	TBA20	TBA30-15	TBA30-40
H62C	1.5 g	1.5 g	1.5 g	1.5 g	1.5 g
SPR212	1.5 g	1.5 g	1.5 g	1.5 g	1.5 g
DMPA	30 mg	30 mg	30 mg	30 mg	30 mg
2T	0.45	0.45 g	0.45 g	0.45 g	0.45 g
TBA		7 g	12 g	7 g	7 g
Camphene	7 g		7 g		
OX50-40					0.75 g
SA-15				0.75 g	

As shown in Figure 56a, all five samples freeze-cast from H62C/SPR212 polymer mixture preserve their shape and mechanical stability after vacuum drying, which is due to a higher cross-linking degree in thiol-ene click chemistry polymerized SPR212 compared to H62C (Figure 46). The addition of SiO₂ powder does not restrict the penetration of incident UV light and allowed full cross-linking across the whole cylinder volume. This is in contrast to the photocuring behavior of GO-containing samples described in the previous section. As explained in the Chapter 1, the refractive index mismatch between photopolymer and dispersed ceramic powder significantly diminishes the attenuation length of UV light. Because SiO₂ powder is UV-transparent and possesses a refractive index of 1.46 (similar to that of the polymer solution), the penetration depths of UV light in these

5.3 SiOC and SiOC/SiO₂ foams with multiscale hierarchical porosity

system is not reduced as significantly as it was in GO/H62C suspension, thus allowing a complete cross-linking over the whole sample.

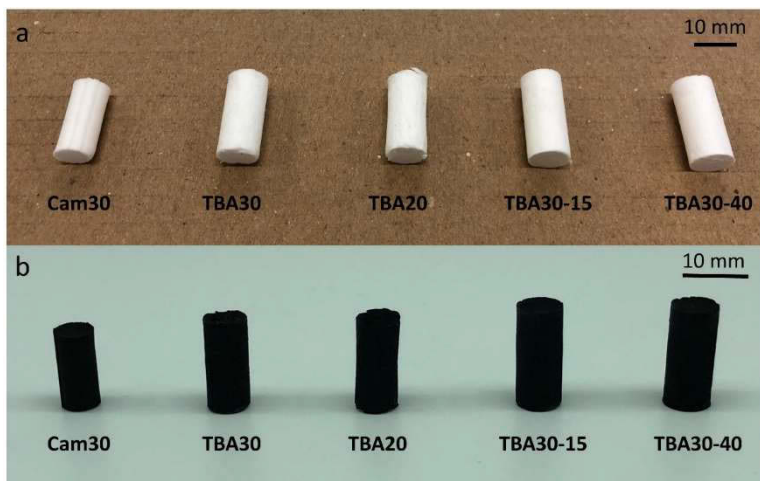


Figure 56. Optical images of (a) freeze dried and (b) pyrolyzed specimens demonstrating almost perfect cylindrical form. In (b) different shrinkage degree is observed while the cylinder geometry was not distorted during the pyrolysis.

Table 22 displays the diameters (d) and linear shrinkage ($((1-d_v/d_0)*100\%)$) of all samples along with other parameters. SiO₂ added to polymers reduces the shrinkage from 8 % in pure polymers to 5 – 6 % in SiO₂ containing samples. The Cam30 sample fabricated from camphene solution exhibits a noteworthy shrinkage of 20 % after vacuum drying, which is significantly larger than that of the other four samples. This could be attributed to the dendritic morphology of camphene crystals, which facilitates the shrinkage of the specimen after sublimation of crystals.

Ceramic monoliths derived by pyrolyzing freeze dried samples at 1100 °C under nitrogen atmosphere following the heating procedure B are shown in Figure 56b. The ceramization process leads to the density increase of specimens accompanied with volumetric

shrinkage, the latter depending on the specimen composition. The Cam30-derived sample exhibits the highest linear shrinkage of 42 % after pyrolysis, while the SiO₂-containing samples demonstrate the lowest linear shrinkage of 29 %. Silica acts as a passive filler, reducing the shrinkage during the ceramization process and enhancing the ceramic yield (m_p/m_v). Regardless of the freezing solvent and polymer concentration, H62C/SPR212-derived samples demonstrate a ceramic yield between 63–65 %, while ceramic yield in the samples with SiO₂ increases to 71 %, corresponding well to the amount of added silica powders. The foam density (ρ^*) of pyrolyzed samples is calculated using Equation 11

$$\rho^* = \frac{m_p}{\pi \cdot \left(\frac{d_p}{2}\right)^2 \cdot h_p} \quad \text{Equation 11}$$

where m_p , d_p and h_p are mass, diameter and height of each ceramic cylinder, respectively. The Cam30-derived sample exhibits the highest foam density of 1.14 g/cm³, with the TBA20-derived sample exhibits the lowest foam density of 0.51 g/cm³. The addition of silica nanopowders enhances the foam density from 0.79 g/cm³ to 0.95 g/cm³ independent of the particle size of the employed SiO₂ powders.

Table 22. Characteristics of freeze cast, vacuum dried and pyrolyzed specimens studied in this chapter.

Sample	Cam30	TBA30	TBA20	TBA30-15	TBA30-40
Freeze cast					
Diameter d_0 [mm]	10	10	10	10	10
Vacuum dried					
Diameter d_v [mm]	8.0	9.2	9.2	9.5	9.4

5.3 SiOC and SiOC/SiO₂ foams with multiscale hierarchical porosity

Mass m_v [g]	0.476	0.429	0.273	0.533	0.524
Linear shrinkage [%]	20	8	8	5	6
Pyrolyzed					
Diameter d_p [mm]	5.8	6.7	6.6	7.1	7.1
Height h_p [mm]	12.6	14.7	14.1	16.0	15.9
Mass m_p [g]	0.301	0.279	0.173	0.373	0.375
Final linear shrinkage [%]	42	33	34	29	29
Foam density [g/cm³]	1.14	0.79	0.51	0.94	0.95
Ceramic yield [%]	63.2	65.0	63.4	70.0	71.6

5.3.2 Pore morphology

Figure 57 shows SEM micrographs of the typical cross-sections of TBA-20 and -30 derived samples taken perpendicular to the solidification direction. A columnar structure is observed in both samples, due to the prismatic form of TBA crystals growing along the freezing direction. Some pores replicate facets of TBA crystallized as rhombic prisms. Highly-aligned pore channels are observed at the top part of the ceramic monoliths. The SEM micrographs of the cross sections close to the cooling source (Figure 57a, c, e & g) demonstrate a more irregular pore morphology, with random pore orientation instead of parallel growth to the freezing direction.

5. Freeze casting of PDCs

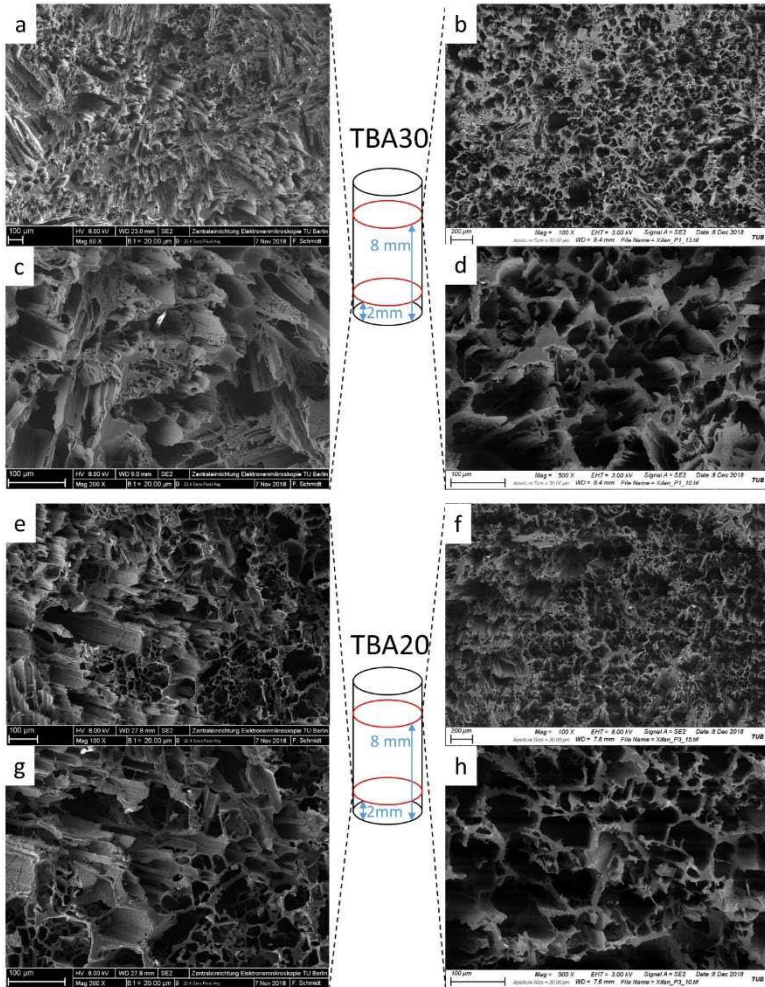


Figure 57. SEM micrographs of ceramic foams derived from TBA30 and TBA20 samples. These images are taken from cross-sections perpendicular to the freezing direction, at distances of 2 mm (left images) and 8 mm (right images) away from the bottom of the sample.

The sample cross-sections positioned far away from the cooling source show more ordered pore morphology, and pore channels are aligned to the freezing direction (Figure 57b, d, f, h).

5.3 SiOC and SiOC/SiO₂ foams with multiscale hierarchical porosity

This phenomenon is frequently observed in freeze cast samples which were subject to instant cooling instead of controlled cooling with stable and low cooling rates. In this work, after casting the polymer solution into the cylindrical mold, the temperature of the brass finger placed below the mold is instantly reduced by immersing it in liquid nitrogen. As a result, a very high cooling rate was applied to the specimens. For the solution near the cold surface, homogeneous nucleation is dominating the solidification of liquid TBA leading to high undercooling in that area. Therefore, the crystal growth rate is significantly smaller than the nucleation rate. The TBA crystals start to grow both randomly and oriented along the freezing direction, because TBA tends to remain liquid under high degrees of undercooling. Therefore, the thermal gradient, which is supposed to guide the crystal growth, vanishes and is replaced by random thermal fluctuations. These fluctuations will eventually lead to random crystal growth. Such unstable freezing behavior of TBA was clearly observed during the freeze casting process, as the transparent solution allowed for observation of the freezing front (see Figure 58).

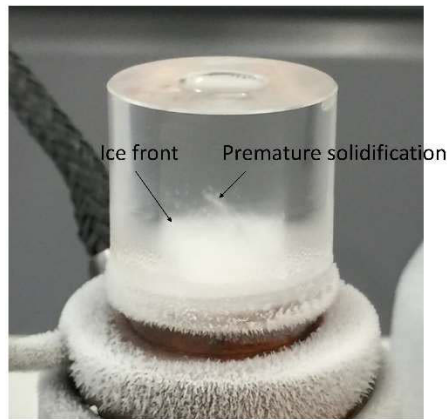


Figure 58. The transparent polymer solution allows the clear observation of the solidification process, here shown exemplarily for sample TBA30.

As shown in Figure 58, premature solidification of TBA takes place even ahead of the planar ice front, and ordered vertical growth does not occur, which further confirms the assumption that significant undercooling was present in this area. As a result, the observed pore morphology in this area is highly irregular. With the continuous growth phase of the TBA ice front, the temperature gradient becomes more significant because of the improved thermal conductivity, thus the growing crystal morphology transits to a more ordered fashion as seen in Figure 57b, d, f, h. Therefore, the pore channels in this area are mostly parallel and aligned with the freezing direction.

The pore size and wall thickness of the freeze cast samples is affected by the solid loading (which in turn is determined by polymer concentration in the starting solutions) as well. As shown in the SEM micrographs of TBA30- and TBA20-derived samples (Figure 57d and Figure 57h, respectively), the wall thickness increases with the polymer concentration, which is consistent with the increase in ceramic foam density as well (Table 22). The influence of polymer concentration on pore size cannot be clearly distinguished, possibly due to the small concentration difference and the fact that TBA tends to solidify in a highly unstable manner.

The Cam30-derived ceramic foam utilizing camphene as freezing vehicle yields distinctly different pore morphologies (Figure 59) compared to the TBA-derived samples due the dendritic growth of camphene crystals. In the bottom of the sample, dendrite arms grew both laterally and vertically to give rise to isotropic pore structure. With the diminishing of the solidification front velocity (middle and top of the sample), primary dendrites started to form caused by the guidance of the applied temperature gradient and secondary dendrite arms began to form laterally due to the distinct structure of the camphene crystal. The pore size as shown in the SEM micrographs is around 10 μm , which is significantly smaller than that in TBA30-derived samples with pore sizes ranging from 50 to 100 μm . This result agrees with the findings that Cam30-derived ceramic

5.3 SiOC and SiOC/SiO₂ foams with multiscale hierarchical porosity

foam demonstrates higher volumetric shrinkage and higher foam density (see Table 22) in comparison to the TBA30-derived foam.

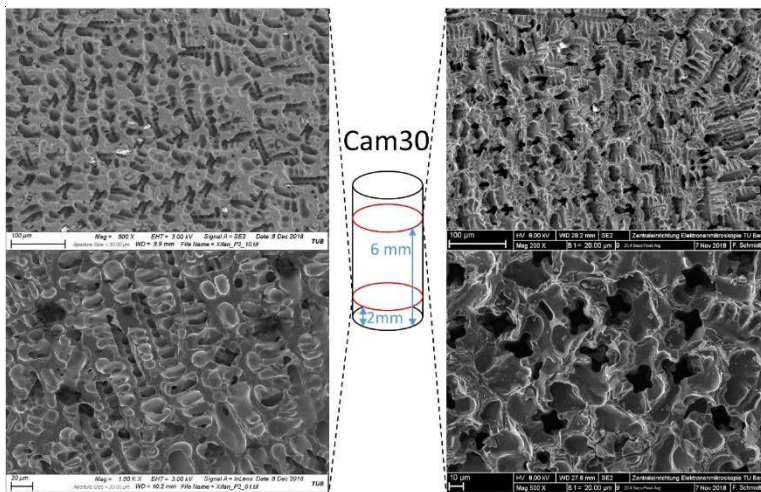


Figure 59. SEM micrographs of ceramic foams derived from Cam30 specimen. These images are taken from cross-sections perpendicular to the freezing direction, at distances of 2 mm (left images) and 6 mm (right images) away from the bottom of the sample.

The ceramic foams derived from SiO₂-containing samples (TBA30-15 and -40) demonstrate columnar pore morphologies similar to TBA30-derived samples, but with significantly improved alignment as shown in Figure 60. This finding is in line with previous results^{96, 98, 136, 137, 139}. In the TBA30-15 and -40 derived samples, the pore channels are highly unidirectional and exhibit well-controlled pore morphology across the whole samples, in contrast to the more irregular pore morphology observed in TBA30-derived samples. It is shown by Brener et al.¹⁴⁰ that thermal fluctuations at the solvent-solid interface can abruptly the solidification of the solvent, which leads to a destruction of the regular crystal growth and in turn pore pattern. Nonetheless the opposite phenomenon is observed in our case. SiO₂ nanoparticles facilitate the formation of regular pore morphologies since they are acting as heterogeneous nucleation centers, which

5. Freeze casting of PDCs

reduce the ability of TBA to remain liquid under significant undercooling and preventing in this way the premature and irregular solidification. Hence the resulting pore structure of silica-containing samples are far more ordered and demonstrate regular prismatic pore channels that template the sublimated TBA crystals. In addition, the pore size gradually increases towards the top of the samples (see Figure 60c,d), with larger pores at the top of the sample and smaller pores at the bottom due to higher degree of undercooling and faster cooling rate near the cooling source.

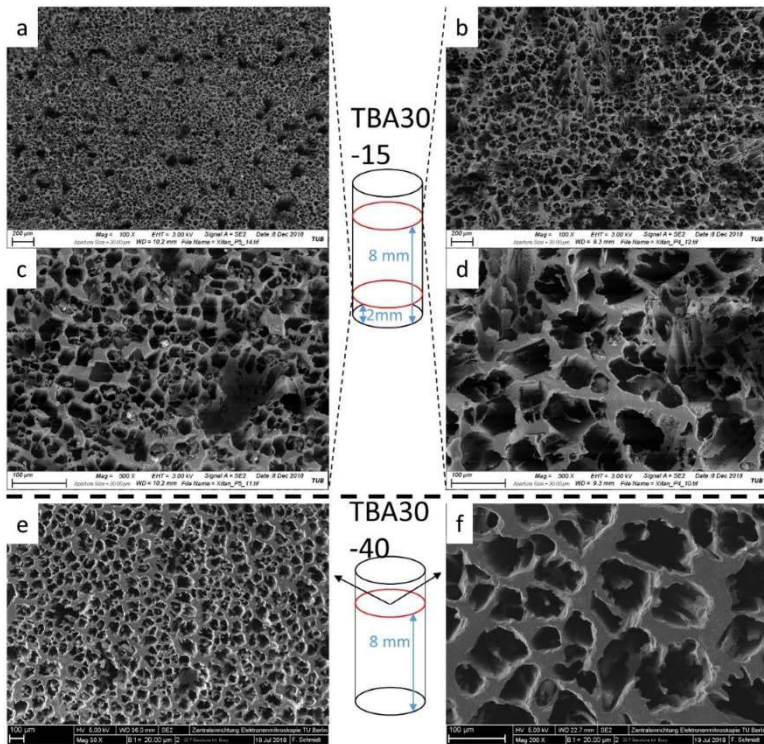


Figure 60. SEM micrographs of TBA30-15 and 40 derived ceramic foams with SiO₂ filler. The images are taken from cross-sections perpendicular to the freezing direction, 2 and 8 mm away from the bottom of the sample.

5.3.3 Multiscale porosity in HF-etched foams

The TBA30- and TBA30-40 derived ceramic foams with and without SiO₂ filler are further etched with hydrofluoric acid solution to generate multiscale porosity. In a typical HF etching process, the samples are first placed in a boiling water bath for 2 hr, which leads to the complete removal of trapped air inside the ceramic foams. Subsequently, the wet ceramic samples are immersed at room temperature under stirring in a 20 vol% HF acid solution for 7 – 72 h. After etching, samples are washed with deionized water three times and dried in ambient conditions, followed with vacuum drying (1 mbar) for 24 hours at room temperature. As known, HF can selectively remove the silica-rich domains in SiOC ceramics, leaving behind carbon-rich domains with nanoporous microstructure^{92, 141–143}. As a result, ultrathin-walled carbon-based materials can be obtained from the HF-etched SiOC¹⁴⁴. Instead of treating the SiOC powder with concentrated HF, in this work, SiOC and SiOC/SiO₂ foams are etched with diluted HF leading to high specific surface area (SSA) monoliths with hierarchical porosity. For the former, the etching time is considered as not important due to the ease of diffusion of the reactant and products (HF and H₂SiF₆, respectively). The reaction can be further facilitated by applying mild stirring and thereby providing sufficient reaction sites. The long channels present in macroporous SiOC monoliths studied in this work hinders HF infiltration and diffusion of reactants and products in-/outside the pore channels. Therefore, the HF etching of SiOC monoliths is conducted with three different reaction times (7 h, 24 h and 72 h). The recorded N₂ adsorption-desorption isotherms of SiOC monoliths before and after HF etching are displayed in Figure 61.

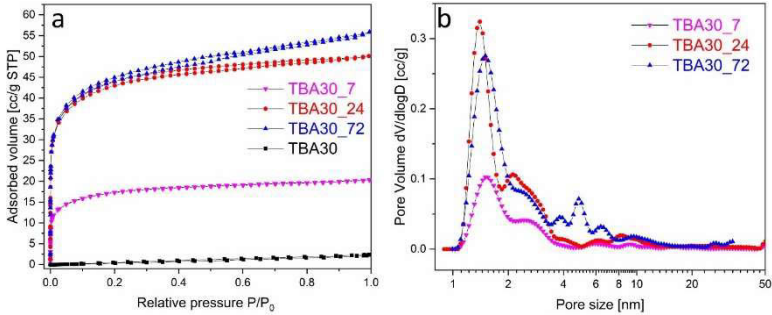


Figure 61. (a) Nitrogen adsorption-desorption isotherms and (b) pore size distribution in micro- and mesopore range for the TBA30-derived samples. For details see Table 23.

The non-etched TBA30-derived SiOC monolith shows an almost planar sorption isotherm, which is characteristic for nonporous materials. The etched TBA30-derived SiOC samples demonstrate typical type I isotherms with a clear steep increase up to $P/P_0 < 0.1$, showing the presence of micropores which are created by the removal of silica-rich nanodomains. The obtained specific surface areas are increased to 63.0, 158.7 and 162.2 m^2/g , with increasing immersion time in HF acid. The increase in SSA values obtained from 24 or 72 hr HF treatment is not significant, suggesting the etching is mostly complete after 24 hr. The desorption isotherm of the sample etched for 72 hr demonstrates a slight hysteresis loop, which could suggest that some pore sizes are increased to the mesopore range (Figure 61b). The majority of the pores are in the micropore range below 2 nm as is typical for type I isotherms. Increasing the etching time to 72 hr does give rise to the appearance of small amounts of mesopores between 4–6 nm. This observation is consistent with the increase of total pore volume despite a slight decrease of micropore volume as shown in Table 23.

5.3 SiOC and SiOC/SiO₂ foams with multiscale hierarchical porosity

Table 23. Specific surface area and micro- and mesopore volume for HF-etched samples studied in this work.

Sample	SiO ₂ filler	HF etching time [h]	SSA, m ² /g	SSA _{micro} , m ² /g	V _{micro} , 10 ⁻² cc/g	V _{total} , 10 ⁻² cc/g
TBA30_7	-	7	63.0	45.6	1.10	3.15
TBA30_24	-	24	158.7	116.3	3.00	7.75
TBA30_72	-	72	162.6	112.9	2.80	8.63
TBA30-40_24	OX50-40	24	406.2	221.5	4.80	43.9
TBA30-40_72	OX50-40	72	494.5	294.5	6.60	49.0

The composition and microstructure of HF-etched samples are further characterized. Energy-dispersive X-ray spectroscopy (Figure 62b) displays homogenous C, O and Si distribution in the samples, while HR-TEM image displays worm-like turbostratic carbon in an amorphous SiOC matrix (Figure 62a).

TBA30-40 derived SiOC foams with SiO₂ filler demonstrate complex adsorption isotherms (Figure 63a), which can be assumed as a combination of type I and IV isotherms. The pore size distribution (Figure 63b) shows micropores below 2 nm, a small amount of mesopores from 2 to 10 nm, and a large amount of mesopores above 30 nm. Due to the abundance of micropores, the absorbed nitrogen volume dramatically increases at low relative pressure again. The clear hysteresis loop appears above P/P₀ = 0.8, indicating the presence of large mesopores and macropores in these samples as well, which are caused by the HF etching of the added silica fillers. Consequently, the SSA of these samples increases from 406 to 494 m²/g with increasing etching time from 24 to 72 hr, with the SSA of these samples being two times larger than the SSA of TBA30-derived samples without SiO₂ filler. Another noteworthy difference between these samples is that the total pore volume of the TBA30-40 derived SiOC foam with SiO₂ filler is one magnitude higher than that of samples without SiO₂, while the corresponding micropore volume is not as significantly

increased. This drastic increase in total pore volume is attributed to the mesopores created by the removal of silica nanopowder. The etching of the added silica nanopowder seems to have the effect of facilitating the etching of the SiOC matrix as well, confirmed by the drastic increase in SSA_{micro} from 113 to 294 m^2/g and micropore volume from 2.8×10^{-2} to $6.6 \times 10^{-2} \text{ cm}^3/\text{g}$ for the samples without and with SiO_2 , respectively. Probably, the SiO_2 dissolution exposes new SiOC surfaces allowing for HF attack and creating interconnected large meso-macropores, which ease the HF diffusion inside the pores. This leads to the formation of significantly larger amounts of micropores. The presence of hierarchical porosity, i.e., micro-, meso- and macropores is evidently shown in HR-TEM images (Figure 64) as well.

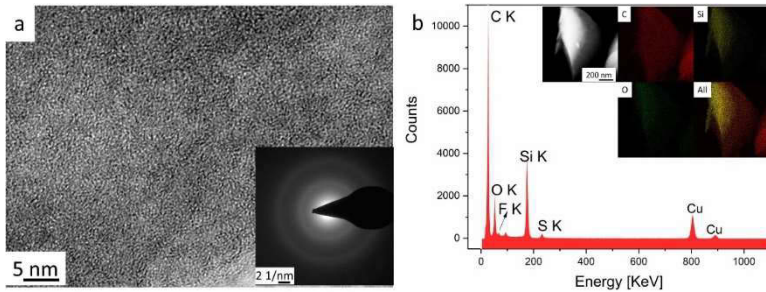


Figure 62. (a) HR-TEM image and (b) EDX spectrum of TBA-30 derived SiOC sample etched with HF for 72 hours. Inset in (a) shows the selected area electron diffraction (SAED) pattern. Insets in (b) are the TEM images and corresponding element distribution of C, Si and O.

5.3 SiOC and SiOC/SiO₂ foams with multiscale hierarchical porosity

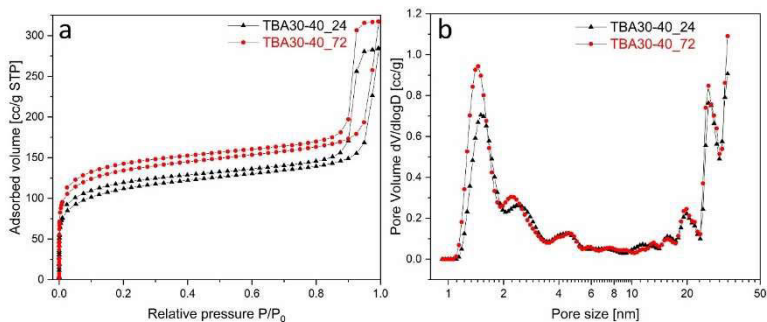


Figure 63. (a) Nitrogen adsorption-desorption isotherm and (b) pore size distribution in micro- and mesopore range for the TBA30-40 derived samples with SiO₂ filler. For details see Table 23.

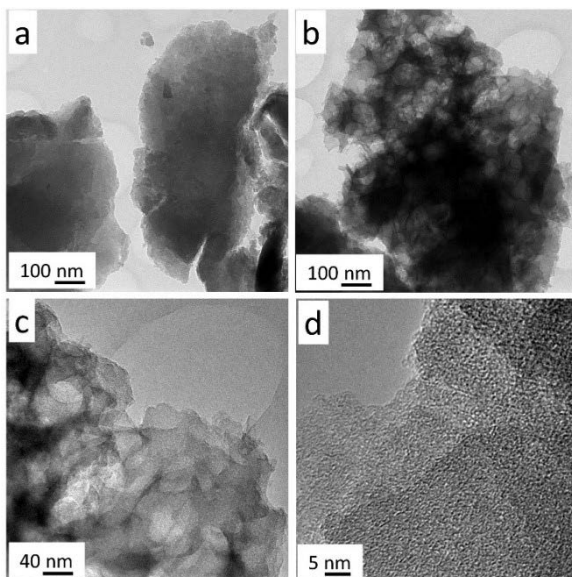


Figure 64. TEM images of HF-etched TBA30 (a) and TBA30-40 derived ceramic foams. The latter demonstrates the hierarchical porosity.

As shown in Figure 64b, the addition of silica nanopowders has introduced a significant amount of interconnecting macropores which are around or smaller than 100 nm after HF etching in

comparison to samples without added silica (Figure 64a), in which macropores produced by freeze casting at this scale are not observable. Despite the added silica powder having an average primary particle size of 40 nm, the obtained slightly larger pore size is possibly attributed to the partial agglomeration of silica powders during the temperature-induced phase separation process. Extensive agglomeration, which would result in significantly larger pores, was not observed, indicating that the silica powders were well-dispersed inside the preceramic polymer matrix after the freeze casting and latter pyrolysis processes. In Figure 64c, mesopores created by the removal of silica nanoparticles and some macropores due to the partial etching of small silica aggregates can be clearly identified, while the micropores induced by etching of silica-rich nanodomains within the SiOC matrix are identified in Figure 64d. The TEM data corroborates the pore size distribution obtained from the adsorption isotherms, and confirms the hierarchical porosity derived from the chemical removal of multi-scale silica regions. In addition, the well-controlled macroporosity derived from freeze casting technique remains unaffected after the HF etching, giving one extra order to the hierarchical porosity of the final ceramic monolith.

5.3.4 Summary

Two vinyl-containing polysiloxanes H62C and SPR212 are selected as SiOC precursors in the developed solution-based freeze casting technique. They both demonstrate applicability with the developed approach, but the polymer foam consisting of pure H62C is vulnerable to developed stress during vacuum drying and tended to deform during handling and processing. As a result, irregular H62C-based cylinders are obtained. In contrast, using a H62C and SPR212 mixture significantly enhances the mechanical integrity of the produced porous foam, which is attributed to the large amount of vinyl functionalities in the SPR212 polymer. This resulted in a higher cross-linking degree. Furthermore, mixed solution- and suspension-based freeze casting is employed by adding silica nanopowders to the

5.3 SiOC and SiOC/SiO₂ foams with multiscale hierarchical porosity

polysiloxane solutions. Polysiloxane / SiO₂ foams with almost perfect cylindrical shapes are obtained, demonstrating that the presence of nano-SiO₂ do not alter the penetration of incident UV light and additionally improved the mechanical stability by minimizing the volumetric shrinkage.

The freeze-cast SiOC monoliths possess aligned pores typical for conventional ceramic suspension-based freeze casting. TBA-based samples are characterized by the unique prismatic pore channels due to the morphology of TBA crystals, while camphene samples yield distinct pore morphologies representing the dendritic growth of camphene crystals. The solution- and suspension-based freeze cast samples using TBA as freezing liquid demonstrate similar pore shapes relative to solution-based TBA samples, but also demonstrate higher ordered pore morphology by showing highly aligned pore channels.

Hierarchical porosities of pyrolyzed SiOC cylinders are obtained by post-pyrolysis HF acid treatment. SiOC samples after immersion in HF acid demonstrated type I adsorption isotherm indicating the presence of micropores, which are produced by the removal of silica-rich nanodomains within the SiOC microstructure. Etching the SiOC-SiO₂ nano-composites changed the type I adsorption isotherm and showed hysteresis loops above the relative pressure of 0.8. This hysteresis loop clearly indicates the presence of meso- and macropores above 30 nm, which are produced by the HF etching of the added SiO₂ nanopowder as pore-forming template. As a result, hierarchically porous polymer-derived ceramics with high surface area can be obtained, due to the presence of multi-scale sacrificial templates, with micropores below 2 nm formed by the selective etching of silica-rich domains in the SiOC microstructure, mesopores and macropores ranging from 30 to 100 nm created by the removal of added silica nanopowders and aligned macropore channels larger than 10 μm created by the freeze casting technique. Considering the applications of pores with different sizes, micro- and mesopores are known for their functionality, while macropores around 100 nm and larger macropores produced via freeze casting are

5. Freeze casting of PDCs

beneficial for material and heat transfer by providing abundant interconnections, good flowability and low pressure drop. Hence the fabricated SiOC cylinder carrying multi-scale porosity ranging from hundreds of μm to less than 2 nm would find enormous applications in various areas, e.g. as catalyst supports and thermal insulators.

6 Conclusions and outlook

In this thesis, the photoinduced thiol-ene polymerization of vinyl-containing preceramic polymers with multifunctional thiol monomers is systematically investigated, and their emerging applications with novel shaping technologies are explored. In this regard, thiol-ene click reaction with preceramic polymers is successfully applied with inverse stereolithography to fabricate 3D cellular polymer-derived ceramics, including SiOC, SiC and SiCN. In addition, performing the photoinduced thiol-ene polymerization at temperature below 0 °C allows the solution-based freeze casting of liquid preceramic polymers, thus leading to the controlled fabrication of macroporous polymer-derived ceramic foams with aligned pores. Accordingly, the developed photopolymerization approach shows high potential in various forming processes and will widen the industrial applications of polymer-derived ceramics significantly.

In the first chapter, an introduction to polymer-derived ceramics, with special focus on the cross-linking mechanisms of preceramic polymers and a comprehensive review on the stereolithography and freeze casting of preceramic polymers, are given. The fabrications methods are classified with utilized cross-linking mechanisms and discussed regarding their advantages and potential drawbacks, which enables the formulation of motivation and research questions in this work.

In the experimental part, in the third chapter, the cross-linking of alkene group-containing preceramic polymers by thiol-ene click reaction is extensively studied. FTIR results, by demonstrating the significant decrease in the intensity of absorption bands associated with alkene groups, confirm the photo-induced thiol-ene click reaction as an efficient tool to crosslink different classes of preceramic polymers, including polycarbosiloxanes, polycarbosilanes and polycarbosilazanes.

Since very low concentration of photoinitiator is required for the triggering of thiol-ene polymerization, it allows the formation of

6. Conclusions and outlook

thick structures with very high aspect ratios. The preparation of preceramic polymer-based organogels is also demonstrated by employing polymer-thiol systems in organic solvents by the same radical-mediated polymerization. This versatility concerning the usage of a wide variety of solvents and pore forming agents opens a new approach to the preparation of highly porous preceramic polymer, and subsequently porous polymer-derived ceramics.

In the fourth chapter, the developed thiol-ene photopolymerization approach is applied for the additive manufacturing of three classes of preceramic polymers, including polycarbosiloxane SPR212, polycarbosilane SMP10 and polycarbosilazane Durazane 1800. The resin formulations are optimized regarding the content of photoinitiator and dithiol. In the curing depth measurements, the presence of photoabsorbers in the prepared resin is shown to be necessary in order to control the penetration depth of incident photons. For the SMP10-based resin, photoabsorbers are not required since the yellowish polycarbosilane resin itself restricts the curing depth. The clean detachment of the thiol-ene cured preceramic polymer from the bottom of the resin tank without distortion and damage is essential for the printing process. Accordingly, a specially-designed resin tank consisting of a transparent FEP film facilitates a better separation between the freshly-cured polymer and the tank bottom than the conventional silicone layer, since it creates peeling edges from all directions and does not have clouding issues, which silicone is prone to. The printed thermosets are subjected to pyrolysis with low heating rate to complete the polymer-to-ceramic transformation. While the additively manufactured cellular polysiloxane SPR212 and polysilazane Dura1800 successfully convert to SiOC and SiCN ceramics without major cracks as shown in their corresponding radiography images, the polycarbosilane SMP10 exploded into tiny pieces under the same pyrolyzing conditions. It is believed that high levels of hydrogenated groups in precursors, which is the case for SMP10, are detrimental as the evolution of a significant volume of

hydrogen gas during pyrolysis can cause failure under certain firing conditions.

The additively manufactured polysiloxane-derived SiOC components fabricated here are nearly fully dense, achieving 97 % of the theoretical density. SEM micrographs demonstrate the smooth surface of printed ceramics without pores. 2D SiOC honeycombs with a cellular density of 0.61 g/cm³ demonstrate a mean hardness of 12 GPA and a mean elastic modulus of 106 GPa, which are in good agreement with reported values for silicon oxycarbide glass produced either via hot-pressing or magnetron sputtering. The honeycombs further exhibit a compressive strength of 216 MPa, surpassing the performance of comparable porous ceramics and stretching the boundaries of material property space in terms of strength-to-weight ratio under compression.

Furthermore, photocurable preceramic polymers with thiols are easily prepared and can be applied in any SLA/DLP printer, as well as in microstereolithography and two-photon polymerization to produce microstructures beyond the resolution limit of DLP technique. The presently developed methods represent a flexible and rapid route towards high-performance additively manufactured polymer-derived ceramics that can find broad application in various engineering fields, particularly for load-bearing materials applied in harsh environments and high temperatures. With appropriate AM techniques, ceramic components can be produced with the developed methods across a range of length-scales with high precision, representing a valuable new capability for industries such as aerospace, automotive, energy conversion and chemical engineering.

In the fifth chapter, a novel approach based on combining the freeze casting technique with cryo photopolymerization is developed. Polysiloxane H62C solutions and H62C/SPR212 mixtures containing thiol and photoinitiator are directionally frozen and illuminated with UV light in a freezer at -20 °C to induce the thiol-ene click reactions in frozen state. The attainment of free-standing solid polymer foam after vacuum drying and the subsequent SiOC cylinder after pyrolysis clearly demonstrates that the free radical-initiated thiol-ene click

6. Conclusions and outlook

reaction effectively cross-linked the vinyl containing liquid preceramic polymers into infusible thermosets even at such low temperatures. While the polymer foam consisting of pure H62C is vulnerable to developed stress during vacuum drying and tends to deform significantly, the porous foam made from H62C and SPR212 mixture demonstrate significantly enhanced mechanical integrity by showing no distortion; this is attributed to the large amount of vinyl functionalities in the SPR212 polymer. With the further addition of silica nanopowders into the freeze casted solutions, polysiloxane/SiO₂ foams with almost perfect cylindrical shape are obtained.

The key factor of this approach relies on the complete photopolymerization of whole frozen samples, which in other words depends on how far the UV light can penetrate through the resin. Therefore, the freezing liquid, preceramic polymers and fillers (e.g., SiO₂) with weak absorption for UV light is preferred to allow high penetration depth, thus leading to the production of filled samples. By utilizing GO suspension as freezing liquid and applying the same procedure, unique ceramic shells of open cylindrical (tubular) shape with an axial hole are obtained. Revealed by UV-Vis spectroscopy, GO demonstrate strong absorbance with the incident UV light, therefore reducing its penetration length and causes the presence of “dark” areas, where preceramic polymer remains in an un-polymerized state since no UV light can pass through. Extensive in-situ radiography imaging thus revealed the formation mechanism of this unique shell morphology, in that the axial hole is formed by the self-flow of non-polymerized polysiloxane due to the gravitational force when temperature increases and TBA crystals are sublimated. HG1 sample with half concentration of GO/TBA suspension compared to HG2 demonstrates thicker shell walls and narrower axial hole, since less GO allows a deeper UV polymerization depth. Therefore, it is reasonable to assume that it is possible to fine-tune the shell thickness as well as the hole size by adjusting the GO amount in the specimens, which subsequently alters the penetration depth of the UV light.

Well-controlled pore morphologies with aligned pore channels are obtained with the freeze-cast SiOC monoliths. Samples produced with TBA as solvents show prismatic pore channels, while in the case of camphene, dendritic pore morphology is observed, replicating the growth of camphene crystals. Adding SiO₂ nanopowder to the polysiloxane solution does not change the concept of developed photopolymerization-assisted freeze casting approach, as the produced SiOC-SiO₂ monoliths demonstrate similar pore shapes relative to solution-based samples. Additionally, higher ordered pore morphology by showing highly aligned pore channels is obtained with TBA-based monoliths by incorporating SiO₂ powder.

The post-pyrolysis HF acid treatments by immersing the SiOC samples in diluted HF acid yields hierarchical porosities. Type I adsorption isotherm is observed in the nitrogen physisorption experiments, indicating that the etched SiOC is incorporated with significant amounts of micropores which are produced by the removal of silica-rich nanodomains presented in the SiOC microstructure. The SiOC-SiO₂ nano-composites after HF etching demonstrated different nitrogen physisorption behavior, as the adsorption isotherm changed to a combination of type I and type IV by showing steep increase up to $P/P_0 < 0.1$ as well as hysteresis loop above $P/P_0 \geq 0.8$. The pore size distribution clearly indicates the presence of additional meso- and macropores above 30 nm, which resulted from the removal of added SiO₂ nanopowder as sacrificial templates. The resultant PDCs monolith thus demonstrates high SSA of 494 m²/g with hierarchical porosities, ranging from micropores below 2 nm produced by the etching of SiOC matrix, to meso- and macropores (30-100 nm) formed by the etching of SiO₂ nanopowder, and to aligned pore channels with pore size above 10 μm attributed to the freeze casting technique. Therefore, the produced ceramic monolith could find wide applications in different areas, e.g., filtration, separation, thermal insulation and chemical engineering.

The experimental results achieved in this work allow to suggest **future research directions** which can be categorized into three

6. Conclusions and outlook

groups: (a) novel hybrid materials design, (b) shaping technologies and (c) potential applications.

Novel hybrid materials design

(i) The synthesis of other ceramic precursors containing photocurable functionalities:

General guidelines for the selection of appropriate ceramic precursors for use with thiol-ene click reactions can be stated as follows: (i) an inorganic-organic hybrid polymer or monomer, where the inorganic core comprises species (such as Al, B, Si, Ti or Zr) that form stable oxides, carbides, nitrides or oxycarbides upon pyrolysis; (ii) the presence of unsaturated carbon double or triple bonds, such as those in vinyl groups; (iii) the propensity to form thiyl radicals through photoinitiation. The synthesis of such inorganic-organic hybrid polymer can be performed by reacting metal alkoxide with carboxylic acid as complexation agent, which contains photo-active groups, including acrylate, methacrylate, thiols, and epoxy. Following with controlled sol-gel reaction, novel metal oxide gel capable of photopolymerization can be obtained and is suitable for stereolithographic approach.

(ii) Filling preceramic polymer resins with ceramic particles:

Similar to conventional ceramic stereolithography, the developed preceramic polymer resin can be suspended with ceramic particles as well and applied with DLP- or stereolithography-based 3D printer. After the pyrolysis, the preceramic polymer will act as a non-sacrificial binder compared to conventional photopolymer and act as a matrix material where the ceramic particles are uniformly dispersed. There are several advantages to incorporating extrinsic ceramic particles: (1) they can act as inert or reactive fillers to accommodate the volume shrinkage and lower the risk of PDCs cracking during pyrolysis, thus facilitate the fabrication of thicker structures (2) they can provide extra functionalities to the PDCs, including biomedical, catalytical, electrical and magnetic properties.

Shaping technologies

(iii) Three-dimensional micro- and nano-fabrication of polymer derived ceramics:

Compare to photopolymers suspended with ceramic particles, the developed photocurable preceramic polymer resins blended with multifunctional thiol monomers are one-phase solutions that do not scatter incident photons, thus it possesses an ultra-high optical transparency. This property has much potential in its applicability in micro-3D printing techniques, including micro-stereolithography and two-photon polymerization. Accordingly, SiOC, SiC and SiCN microstructures down to hundreds of nanometers scale could be fabricated, and they shall open a new era in the nanofabrication of ceramic materials.

(iv) Coating, membranes, and microemulsions:

The developed preceramic polymer resin can be utilized for coating or membrane fabrication, by combining the conventional coating techniques, e.g., dip coating, spin coating, with one extra step of photopolymerization. The efficient thiol-ene polymerization will allow the rapid fabrication of preceramic polymer coatings, whereas the traditional coating of PDCs requires time consuming solvent removal and latter cross-linking process. Furthermore, the photo-induced thiol-ene click reaction can be incorporated with the preparation of preceramic polymer-based microemulsions, which yields micro-spheres. Once again, the photopolymerization is a convenient and rapid cross-linking mechanism for the preceramic polymer, therefore easing the production procedure.

Potential applications

(v) Strong high temperature resistant ceramics

The additively manufactured SiOC honeycombs exhibit impressive strength to density ratio, demonstrating huge potential as

6. Conclusions and outlook

load-bearing components. Since the PDCs are known to possess excellent thermomechanical properties (especially the SiCN, SiBCN, SiC classes), following studies shall be conducted to additive manufacture the complex shaped non-oxygen containing PDCs both from micro to macro scale and characterize their performance as temperature- and environment-resistant ceramics.

(vi) Catalysts supports

The produced ceramic foams with hierarchical porosity with high surface area can be ideal catalyst supports, since micro- and mesopores are beneficial for the coating of catalytically-active species, while macropores are advantageous for material and heat transport. Therefore, the fabricated cylinder shall be coated with catalytically active compounds (Ni, Pd or Pt), via incipient wetness impregnation or wet impregnation method, and be tested for its catalytic applications.

7 References

1. P. Colombo, R. Riedel, G. D. Soraru, and H.-J. Kleebe (eds.): ‘Polymer derived ceramics: From nano-structure to applications’; 2010, Lancaster, Pa., DEStech Publications.
2. R. Riedel, H.-J. Kleebe, H. Schönfelder, and F. Aldinger: ‘A covalent micro/nano-composite resistant to high-temperature oxidation’, *Nature*, 1995, **374**(6522), 526, doi: 10.1038/374526a0.
3. Z.-C. Wang, F. Aldinger, and R. Riedel: ‘Novel Silicon-Boron-Carbon-Nitrogen Materials Thermally Stable up to 2200°C’, *J American Ceramic Society*, 2001, **84**(10), 2179–2183, doi: 10.1111/j.1151-2916.2001.tb00984.x.
4. R. Riedel, G. Mera, R. Hauser, and A. Klönczynski: ‘Silicon-Based Polymer-Derived Ceramics: Synthesis Properties and Applications-A Review’, *J. Ceram. Soc. Japan*, 2006, **114**(1330), 425–444, doi: 10.2109/jcersj.114.425.
5. E. Ionescu, H.-J. Kleebe, and R. Riedel: ‘Silicon-containing polymer -derived ceramic nanocomposites (PDC-NCs): preparative approaches and properties’, *Chemical Society Reviews*, 2012, **41**(15), 5032–5052, doi: 10.1039/C2CS15319J.
6. P. Colombo, G. Mera, R. Riedel, and G. D. Soraru: ‘ Polymer - Derived Ceramics: 40 Years of Research and Innovation in Advanced Ceramics ’ , *Journal of the American Ceramic Society*, 2010, **93**(7), 1805–1837, doi: 10.1111/j.1551-2916.2010.03876.x.
7. E. Ionescu, C. Linck, C. Fasel, M. Müller, H. - J. Kleebe, and R. Riedel: ‘ Polymer - Derived SiOC/ZrO₂ Ceramic Nanocomposites with Excellent High - Temperature Stability

7. References

- ' , *Journal of the American Ceramic Society*, 2010, **93**, doi: 10.1111/j.1551-2916.2009.03395.x.
8. M. Hojamberdiev, R. M. Prasad, K. Morita, Y. Zhu, M. A. Schiavon, A. Gurlo, and R. Riedel: 'Template-free synthesis of polymer-derived mesoporous SiOC/TiO₂ and SiOC/N-doped TiO₂ ceramic composites for application in the removal of organic dyes from contaminated water', *Applied Catalysis B: Environmental*, 2012, **115–116**, 303–313, doi: 10.1016/j.apcatb.2011.12.036.
 9. E. Ionescu, B. Papendorf, H.-J. Kleebe, F. Poli, K. Müller, and R. Riedel: 'Polymer-Derived Silicon Oxycarbide/Hafnia Ceramic Nanocomposites. Part I: Phase and Microstructure Evolution During the Ceramization Process', *J American Ceramic Society*, 2010, 347, doi: 10.1111/j.1551-2916.2010.03765.x.
 10. G. Mera, M. Gallei, S. Bernard, and E. Ionescu: 'Ceramic Nanocomposites from Tailor-Made Pre-ceramic Polymers', *Nanomaterials*, 2015, **5**(2), 468–540, doi: 10.3390/nano5020468.
 11. M. Zaheer, T. Schmalz, G. Motz, and R. Kempe: 'Polymer derived non-oxide ceramics modified with late transition metals', *Chem. Soc. Rev.*, 2012, **41**(15), 5102–5116, doi: 10.1039/C2CS15326B.
 12. M. Seifollahi Bazarjani, H.-J. Kleebe, M. M. Müller, C. Fasel, M. Baghaie Yazdi, A. Gurlo, and R. Riedel: 'Nanoporous Silicon Oxycarbonitride Ceramics Derived from Polysilazanes In situ Modified with Nickel Nanoparticles', *Chem. Mater.*, 2011, **23**(18), 4112–4123, doi: 10.1021/cm200589n.
 13. H. P. Macedo, R. L.B.A. Medeiros, J. Ilsemann, D. M.A. Melo, K. Rezwan, and M. Wilhelm: 'Nickel-containing hybrid ceramics derived from polysiloxanes with hierarchical porosity for CO₂ methanation', *Microporous and Mesoporous Materials*, 2018, doi: 10.1016/j.micromeso.2018.11.006.
 14. H. Ichikawa: 'Polymer-Derived Ceramic Fibers', *Annu. Rev. Mater. Res.*, 2016, **46**(1), 335–356, doi: 10.1146/annurev-matsci-070115-032127.

15. K. Lu and D. Erb: 'Polymer derived silicon oxycarbide-based coatings', *International Materials Reviews*, 2017, **89**, 1–23, doi: 10.1080/09506608.2017.1322247.
16. R. M. Prasad, Y. Jüttke, H. Richter, I. Voigt, R. Riedel, and A. Gurlo: 'Mechanism of Gas Separation through Amorphous Silicon Oxycarbide Membranes', *Advanced Engineering Materials*, 2016, **18**, doi: 10.1002/adem.201500380.
17. Y. Jüttke, H. Richter, I. Voigt, R. M. Prasad, M. Bazarjani, A. Gurlo, and R. Riedel: 'Polymer Derived Ceramic Membranes for Gas Separation', *Chemical Engineering Transactions*, 2013, **32**, 1891, doi: 10.3303/CET1332316.
18. S. Kaur, R. Riedel, and E. Ionescu: 'Pressureless fabrication of dense monolithic SiC ceramics from a polycarbosilane', *Journal of the European Ceramic Society*, 2014, **34**(15), 3571–3578, doi: 10.1016/j.jeurceramsoc.2014.05.002.
19. A. Müller-Köhn, J. Janik, A. Neubrand, H. Klemm, T. Moritz, and A. Michaelis: 'Fabrication of Short Fiber Reinforced SiCN by Injection Molding of Pre-ceramic Polymers', in 'High Temperature Ceramic Matrix Composites 8: A collection of papers presented at the HTC MC-8 Conference, September 22–26, 2013, Xi'an, Shaanxi, China', (ed. D. Jiang and L. Zhang), 381–389; 2014, Westerville, Ohio, Hoboken, American Ceramic Society.
20. E. Bernardo, G. Parciannello, P. Colombo, and S. Matthews: 'Wollastonite Foams From an Extruded Pre-ceramic Polymer Mixed with CaCO₃ Microparticles Assisted by Supercritical Carbon Dioxide', *Adv. Eng. Mater.*, 2013, **15**(1-2), 60–65, doi: 10.1002/adem.201200202.
21. T. Taki, K. Ohamura, and M. Sato: 'A study of the oxidation curing mechanism of polycarbosilane fibre by solid-state high-resolution nuclear magnetic resonance', *J Mater Sci*, 1989, **24**(4), 1263–1267, doi: 10.1007/PL00020205.
22. H. Q. Ly, R. Taylor, R. J. Day, and F. Heatley: 'Conversion of polycarbosilane (PCS) to SiC-based ceramic Part 1.

7. References

- Characterisation of PCS and curing products', *Journal of Materials Science*, **36**(16), 4037–4043, doi: 10.1023/A:1017942826657.
23. G. Chollon, M. Czerniak, R. Pailler, X. Bourrat, R. Naslain, J. P. Pillot, and R. Cannet: 'A model SiC-based fibre with a low oxygen content prepared from a polycarbosilane precursor', *Journal of Materials Science*, **32**(4), 893–911, doi: 10.1023/A:1018597432067.
 24. G. D. Soraru, F. Babonneau, and J. D. Mackenzie: 'Structural evolutions from polycarbosilane to SiC ceramic', *Journal of Materials Science*, 1990, **25**(9), 3886–3893, doi: 10.1007/BF00582455.
 25. E. Ionescu: 'Polymer - Derived Ceramics', 2014/05/23, Wiley - VCH Verlag GmbH & Co. KGaA; available at <http://onlinelibrary.wiley.com/doi/10.1002/9783527631940.ch49/pdf>, doi: 10.1002/9783527631940.ch49.
 26. E. Kroke, Y.-L. Li, C. Konetschny, E. Lecomte, C. Fasel, and R. Riedel: 'Silazane derived ceramics and related materials', *Materials Science and Engineering: R: Reports*, 2000, **26**(4–6), 97–199, doi: 10.1016/S0927-796X(00)00008-5.
 27. R. L. Cicero, M. R. Linford, and C. E. D. Chidsey: 'Photoreactivity of Unsaturated Compounds with Hydrogen-Terminated Silicon(111)', *Langmuir*, 2000, **16**(13), 5688–5695, doi: 10.1021/la9911990.
 28. L.-A. Liew, R. A. Saravanan, V. M. Bright, M. L. Dunn, J. W. Daily, and R. Raj: 'Processing and characterization of silicon carbon-nitride ceramics: application of electrical properties towards MEMS thermal actuators', *Micromechanics section of Sensors and Actuators, based on contributions revised from the Technical Digest of the 15th IEEE International conference on Micro Electro mechanical Systems (MEMS 2002)*, **103**(1–2), 171–181, doi: 10.1016/S0924-4247(02)00330-8.
 29. L.-A. Liew, Y. Liu, R. Luo, T. Cross, L. An, V. M. Bright, M. L. Dunn, J. W. Daily, and R. Raj: 'Fabrication of SiCN MEMS by photopolymerization of pre-ceramic polymer', *Sensors and*

- Actuators A: Physical*, 2002, **95**(2), 120–134, doi: 10.1016/S0924-4247(01)00723-3.
30. R. A. Saravanan, L. - A. Liew, V. M. Bright, and R. Raj: ‘ Integration of Ceramics Research with the Development of a Microsystem’ , *Journal of the American Ceramic Society*, 2003, **86**(7), 1217–1219, doi: 10.1111/j.1151-2916.2003.tb03453.x.
 31. C. Wang, G. Jia, L. H. Taherabadi, and M. J. Madou: ‘A novel method for the fabrication of high-aspect ratio C-MEMS structures’, *J. Microelectromech. Syst.*, 2005, **14**(2), 348–358, doi: 10.1109/JMEMS.2004.839312.
 32. M. Schulz: ‘Polymer derived ceramics in MEMS/NEMS – a review on production processes and application’, *Advances in Applied Ceramics*, 2009, **108**(8), 454–460, doi: 10.1179/174367609X422171.
 33. M. Schulz, M. Börner, J. Göttert, T. Hanemann, J. Haußelt, and G. Motz: ‘Cross Linking Behavior of Preceramic Polymers Effected by UV - and Synchrotron Radiation’ , *Advanced Engineering Materials*, 2004, **6**(8), 676–680, doi: 10.1002/adem.200400082.
 34. T. A. Pham, P. Kim, M. Kwak, K. Y. Suh, and D.-P. Kim: ‘Inorganic polymer photoresist for direct ceramic patterning by photolithography’, *Chem. Commun.*, 2007, **39**(39), 4021–4023, doi: 10.1039/B708480C.
 35. T.-H. Yoon, H.-J. LEE, J. YAN, and D.-P. Kim: ‘Fabrication of SiC-Based Ceramic Microstructures from Preceramic Polymers with Sacrificial Templates and Lithographic Techniques-A Review’, *J. Ceram. Soc. Japan*, 2006, **114**(1330), 473–479, doi: 10.2109/jcersj.114.473.
 36. S. K. Reddy, N. B. Cramer, T. Cross, R. Raj, and C. N. Bowman: ‘Polymer-Derived Ceramic Materials from Thiol-ene Photopolymerizations’, *Chem. Mater.*, 2003, **15**(22), 4257–4261, doi: 10.1021/cm034291x.

7. References

37. C. E. Hoyle and C. N. Bowman: 'Thiol–Ene Click Chemistry', *Angewandte Chemie International Edition*, 2010, **49**(9), 1540–1573, doi: 10.1002/anie.200903924.
38. A. V. Bordoni, M. Verónica Lombardo, and W. Alejandro: 'Photochemical radical thiol–ene click-based methodologies for silica and transition metal oxides materials chemical modification: a mini-review', *RSC Advances*, 2016, **6**(81), 77410–77426, doi: 10.1039/C6RA10388J.
39. M. S. Kharasch, J. Read, and F. R. Mayo: 'Correspondence', *J. Chem. Technol. Biotechnol.*, 1938, **57**(32), 752–754, doi: 10.1002/jctb.5000573206.
40. F. Alves and I. Nischang: 'Tailor-made hybrid organic-inorganic porous materials based on polyhedral oligomeric silsesquioxanes (POSS) by the step-growth mechanism of thiol-ene "click" chemistry', *Chemistry (Weinheim an der Bergstrasse, Germany)*, 2013, **19**(51), 17310–17313, doi: 10.1002/chem.201303759.
41. ISO/ASTM: 'Additive manufacturing - General principles: Terminology', 2015-12-15, (52900), 2015th edn, ISO copyright office, ASTM International.
42. D. Bourell, J. Beaman, M. Leu, and D. Rosen: 'A brief history of additive manufacturing and the 2009 roadmap for additive manufacturing: Looking back and looking ahead', *Proceedings of RapidTech*, 2009, 24–25.
43. M. Attaran: 'The rise of 3-D printing: The advantages of additive manufacturing over traditional manufacturing', *Business Horizons*, 2017, **60**(5), 677–688, doi: 10.1016/j.bushor.2017.05.011.
44. ISO: 'Additive manufacturing - General principles: Part 2: Overview of process categories and', 2015-01-15, (17296 - 2), 2015th edn, ISO copyright office.
45. I. Gibson, D. Rosen, and B. Stucker: 'Additive manufacturing technologies: 3D printing, rapid prototyping and direct digital manufacturing'; 2015, New York, Heidelberg, Dodrecht, London, Springer.

46. K. V. Wong and A. Hernandez: 'A Review of Additive Manufacturing', *ISRN Mechanical Engineering*, 2012, **2012**(4), 1–10, doi: 10.5402/2012/208760.
47. J. Deckers, J. Vleugels, and J.-P. Kruth: 'Additive manufacturing of ceramics: A review', *Journal of Ceramic Science and Technology*, 2014, **5**(4), 245–260.
48. A. Zocca, P. Colombo, C. M. Gomes, J. Günster, and D. J. Green: 'Additive Manufacturing of Ceramics: Issues, Potentialities, and Opportunities', *J. Am. Ceram. Soc.*, 2015, **98**(7), 1983–2001, doi: 10.1111/jace.13700.
49. N. Travitzky, A. Bonet, B. Dermeik, T. Fey, I. Filbert - Demut, L. Schlier, T. Schlordt, and P. Greil: 'Additive Manufacturing of Ceramic - Based Materials', *Advanced Engineering Materials*, 2014, **16**(6), 729–754, doi: 10.1002/adem.201400097.
50. J. A. Lewis: 'Colloidal Processing of Ceramics', *J American Ceramic Society*, 2000, **83**(10), 2341–2359, doi: 10.1111/j.1151-2916.2000.tb01560.x.
51. B. Cappi, E. Özkol, J. Ebert, and R. Telle: 'Direct inkjet printing of Si₃N₄: Characterization of ink, green bodies and microstructure', *Journal of the European Ceramic Society*, 2008, **28**(13), 2625–2628, doi: 10.1016/j.jeurceramsoc.2008.03.004.
52. M. Mott and J. R. G. Evans: 'Solid Freeforming of Silicon Carbide by Inkjet Printing Using a Polymeric Precursor', *J American Ceramic Society*, 2001, **84**(2), 307–313, doi: 10.1111/j.1151-2916.2001.tb00655.x.
53. F. C. G. Sousa and J. R. G. Evans: 'Sintered Hydroxyapatite Latticework for Bone Substitute', *J American Ceramic Society*, 2003, **86**(3), 517–519, doi: 10.1111/j.1151-2916.2003.tb03332.x.
54. J. A. Lewis, J. E. Smay, J. Stuecker, and J. Cesarano: 'Direct Ink Writing of Three-Dimensional Ceramic Structures', *J American Ceramic Society*, 2006, **89**(12), 3599–3609, doi: 10.1111/j.1551-2916.2006.01382.x.
55. K. Cai, B. Román-Manso, J. E. Smay, J. Zhou, M. I. Osendi, M. Belmonte, and P. Miranzo: 'Geometrically Complex Silicon

7. References

- Carbide Structures Fabricated by Robocasting', *J American Ceramic Society*, 2012, **95**(8), 2660–2666, doi: 10.1111/j.1551-2916.2012.05276.x.
56. G. Pierin, C. Grotta, P. Colombo, and C. Mattevi: 'Direct Ink Writing of micrometric SiOC ceramic structures using a preceramic polymer', *Journal of the European Ceramic Society*, 2016, **36**(7), 1589–1594, doi: 10.1016/j.jeurceramsoc.2016.01.047.
57. Z. Fu, L. Schlier, N. Travitzky, and P. Greil: 'Three-dimensional printing of SiSiC lattice truss structures', *Materials Science and Engineering: A*, 2013, **560**, 851–856, doi: 10.1016/j.msea.2012.09.107.
58. A. Zocca, C. M. Gomes, A. Staude, E. Bernardo, J. Günster, and P. Colombo: 'SiOC ceramics with ordered porosity by 3D-printing of a preceramic polymer', *J. Mater. Res.*, 2013, **28**(17), 2243–2252, doi: 10.1557/jmr.2013.129.
59. J. Wilkes, Y. - C. Hagedorn, W. Meiners, and K. Wissenbach: ' Additive manufacturing of $ZrO_2 - Al_2O_3$ ceramic components by selective laser melting', *Rapid Prototyping Journal*, 2013, **19**(1), 51–57, doi: 10.1108/13552541311292736.
60. T. Friedel, N. Travitzky, F. Niebling, M. Scheffler, and P. Greil: 'Fabrication of polymer derived ceramic parts by selective laser curing', *Journal of the European Ceramic Society*, 2005, **25**(2-3), 193–197, doi: 10.1016/j.jeurceramsoc.2004.07.017.
61. T. Mühler, C. M. Gomes, J. Heinrich, and J. Günster: 'Slurry-Based Additive Manufacturing of Ceramics', *International Journal of Applied Ceramic Technology*, 2015, **12**(1), 18–25, doi: 10.1111/ijac.12113.
62. E. M. Sachs, J. S. Haggerty, M. J. Cima, and P. A. Williams: 'Three-dimensional printing techniques', US5204055A.
63. M. L. Griffith and J. W. Halloran: 'Freeform Fabrication of Ceramics via Stereolithography', *Journal of the American Ceramic Society*, 1996, **79**(10), 2601–2608, doi: 10.1111/j.1151-2916.1996.tb09022.x.

64. C. Hinczewski, S. Corbel, and T. Chartier: ‘Stereolithography for the fabrication of ceramic three - dimensional parts’ , *Rapid Prototyping Journal*, 1998, **4**(3), 104–111, doi: 10.1108/13552549810222867.
65. T. Chartier, C. Chaput, F. Doreau, and M. Loiseau: ‘Stereolithography of structural complex ceramic parts’, *Journal of Materials Science*, 2002, **37**(15), 3141–3147, doi: 10.1023/A:1016102210277.
66. A. Licciulli, C.E. Corcione, A. Greco, V. Amicarelli, and A. Maffezzoli: ‘Laser stereolithography of ZrO₂ toughened Al₂O₃’, *Journal of the European Ceramic Society*, 2004, **24**(15), 3769–3777, doi: 10.1016/j.jeurceramsoc.2003.12.024.
67. T. Chartier, C. Duterte, N. Delhote, D. Baillargeat, S. Verdeyme, C. Delage, and C. Chaput: ‘Fabrication of Millimeter Wave Components Via Ceramic Stereo- and Microstereolithography Processes’, *J American Ceramic Society*, 2008, **50**([3]), 2469–2474, doi: 10.1111/j.1551-2916.2008.02482.x.
68. T. Chartier, A. Badev, Y. Abouliatim, P. Lebaudy, and L. Lecamp: ‘Stereolithography process: Influence of the rheology of silica suspensions and of the medium on polymerization kinetics – Cured depth and width’, *Journal of the European Ceramic Society*, 2012, **32**(8), 1625–1634, doi: 10.1016/j.jeurceramsoc.2012.01.010.
69. F. Kotz, K. Arnold, W. Bauer, D. Schild, N. Keller, K. Sachsenheimer, T. M. Nargang, C. Richter, D. Helmer, and B. E. Rapp: ‘Three-dimensional printing of transparent fused silica glass’, *Nature*, 2017, **544**(7650), 337–339, doi: 10.1038/nature22061.
70. J. W. Halloran, M. L. Griffith, and T.-M. Chu: ‘Stereolithography resin for rapid prototyping of ceramics and metals’, US6117612A, 8 October 1997.
71. A. Y.-T. Wang: ‘Additive Manufacturing of Polymer-derived Ceramics with Bioactive Filler’, Master Thesis, RWTH Aachen University; Technische Universität Berlin, 2018.

7. References

72. P. F. Jacobs and D. T. Reid: 'Rapid prototyping & manufacturing: Fundamentals of stereolithography', 1st edn; 1992, Dearborn, Mich., SME.
73. S. P. Gentry and J. W. Halloran: 'Light scattering in absorbing ceramic suspensions: Effect on the width and depth of photopolymerized features', *Journal of the European Ceramic Society*, 2015, **35**(6), 1895–1904, doi: 10.1016/j.jeurceramsoc.2014.12.006.
74. J. W. Halloran: 'Ceramic Stereolithography: Additive Manufacturing for Ceramics by Photopolymerization', *Annu. Rev. Mater. Res.*, 2016, **46**(1), 19–40, doi: 10.1146/annurev-matsci-070115-031841.
75. T. A. Pham, D. - P. Kim, T. - W. Lim, S. - H. Park, D. - Y. Yang, and K. - S. Lee: 'Three - Dimensional SiCN Ceramic Microstructures via Nano - Stereolithography of Inorganic Polymer Photoresists' , *Advanced Functional Materials*, 2006, **16**(9), 1235–1241, doi: 10.1002/adfm.200600009.
76. E. Zanchetta, M. Cattaldo, G. Franchin, M. Schwentenwein, J. Homa, G. Brusatin, and P. Colombo: 'Stereolithography of SiOC Ceramic Microcomponents', *Advanced Materials*, 2016, **28**(2), 370–376, doi: 10.1002/adma.201503470.
77. Y. Fu, G. Xu, Z. Chen, C. liu, D. Wang, and C. Lao: 'Multiple metals doped polymer-derived SiOC ceramics for 3D printing', *Ceramics International*, 2018, **44**(10), 11030–11038, doi: 10.1016/j.ceramint.2018.03.075.
78. L. Brigo, J. E. M. Schmidt, A. Gandin, N. Michieli, P. Colombo, and G. Brusatin: '3D Nanofabrication of SiOC Ceramic Structures', *Adv. Sci.*, 2018, **3**, 1800937, doi: 10.1002/advs.201800937.
79. Y. de Hazan and D. Penner: 'SiC and SiOC ceramic articles produced by stereolithography of acrylate modified polycarbosilane systems', *Journal of the European Ceramic Society*, 2017, **37**, 5205–5212, doi: 10.1016/j.jeurceramsoc.2017.03.021.

80. S. Li, W. Duan, T. Zhao, W. Han, L. Wang, R. Dou, and G. Wang: ‘The fabrication of SiBCN ceramic components from preceramic polymers by digital light processing (DLP) 3D printing technology’, *Journal of the European Ceramic Society*, 2018, **38**(14), 4597–4603, doi: 10.1016/j.jeurceramsoc.2018.06.046.
81. J. Schmidt and P. Colombo: ‘Digital light processing of ceramic components from polysiloxanes’, *Journal of the European Ceramic Society*, 2018, **38**(1), 57–66, doi: 10.1016/j.jeurceramsoc.2017.07.033.
82. Z. C. Eckel, C. Zhou, J. H. Martin, A. J. Jacobsen, W. B. Carter, and T. A. Schaedler: ‘Additive manufacturing of polymer-derived ceramics’, *Science*, 2016, **351**(6268), 58–62, doi: 10.1126/science.aad2688.
83. H. Cui, R. Hensleigh, H. Chen, and X. Zheng: ‘Additive Manufacturing and size-dependent mechanical properties of three-dimensional microarchitected, high-temperature ceramic metamaterials’, *Journal of Materials Research*, 2018, **33**(3), 360–371, doi: 10.1557/jmr.2018.11.
84. S. Park, D.-H. Lee, H.-I. Ryoo, T.-W. Lim, D.-Y. Yang, and D.-P. Kim: ‘Fabrication of three-dimensional SiC ceramic microstructures with near-zero shrinkage via dual crosslinking induced stereolithography’, *Chem. Commun.*, 2009, **0**(32), 4880–4882, doi: 10.1039/B907923H.
85. P. Jana, O. Santoliquido, A. Ortona, P. Colombo, and G. D. Sorarù: ‘Polymer-derived SiCN cellular structures from replica of 3D printed lattices’, *Journal of the American Ceramic Society*, 2018, **101**(7), 2732–2738, doi: 10.1111/jace.15533.
86. U. G. K. Wegst, H. Bai, E. Saiz, A. P. Tomsia, and R. O. Ritchie: ‘Bioinspired structural materials’, *Nature materials*, 2015, **14**(1), 23, doi: 10.1038/nmat4089.
87. S. Deville: ‘Freeze - Casting of Porous Ceramics: A Review of Current Achievements and Issues’ , *Advanced Engineering Materials*, 2008, **10**(3), 155–169, doi: 10.1002/adem.200700270.

7. References

88. J. S. Wettlaufer, M. G. Worster, and H. E. Huppert: 'Natural convection during solidification of an alloy from above with application to the evolution of sea ice', *J. Fluid Mech.*, 1997, **344**, 291–316, doi: 10.1017/S0022112097006022.
89. S. Deville, E. Maire, A. Lasalle, A. Bogner, C. Gauthier, J. Leloup, and C. Guizard: 'In Situ X-Ray Radiography and Tomography Observations of the Solidification of Aqueous Alumina Particle Suspensions-Part I: Initial Instants', *J American Ceramic Society*, 2009, **92**(11), 2489–2496, doi: 10.1111/j.1551-2916.2009.03163.x.
90. Q. Fu, M. N. Rahaman, F. Dogan, and B. S. Bal: 'Freeze casting of porous hydroxyapatite scaffolds. I. Processing and general microstructure', *Journal of biomedical materials research. Part B, Applied biomaterials*, 2008, **86**(1), 125–135, doi: 10.1002/jbm.b.30997.
91. P. Colombo: 'Conventional and novel processing methods for cellular ceramics', *Philosophical Transactions of the Royal Society A: Mathematical, Physical and Engineering Sciences*, 2006, **364**(1838), 109–124, doi: 10.1098/rsta.2005.1683.
92. C. Vakifahmetoglu, D. Zeydanli, and P. Colombo: 'Porous polymer derived ceramics', *Materials Science and Engineering: R: Reports*, 2016, **106**, 1–30, doi: 10.1016/j.mser.2016.05.001.
93. M. Naviroj, P. W. Voorhees, and K. T. Faber: 'Suspension- and solution-based freeze casting for porous ceramics', *Journal of Materials Research*, 2017, **32**(17), 3372–3382, doi: 10.1557/jmr.2017.133.
94. B. - H. Yoon, C. - S. Park, H. - E. Kim, and Y. - H. Koh: 'In Situ Synthesis of Porous Silicon Carbide (SiC) Ceramics Decorated with SiC Nanowires', *Journal of the American Ceramic Society*, 2007, **90**(12), 3759–3766, doi: 10.1111/j.1551-2916.2007.02037.x.
95. B. - H. Yoon, E. - J. Lee, H. - E. Kim, and Y. - H. Koh: 'Highly Aligned Porous Silicon Carbide Ceramics by Freezing Polycarbosilane/Camphene Solution', *Journal of the American*

- Ceramic Society*, 2007, **90**(6), 1753–1759, doi: 10.1111/j.1551-2916.2007.01703.x.
96. M. Naviroj, S. M. Miller, P. Colombo, and K. T. Faber: ‘Directionally aligned macroporous SiOC via freeze casting of preceramic polymers’, *Journal of the European Ceramic Society*, 2015, **35**(8), 2225–2232, doi: 10.1016/j.jeurceramsoc.2015.02.013.
97. K. A. Jackson: ‘Constitutional supercooling surface roughening’, *Journal of Crystal Growth*, 2004, **264**(4), 519–529, doi: 10.1016/j.jcrysgro.2003.12.074.
98. N. Soltani, U. Simon, A. Bahrami, X. Wang, S. Selve, J. D. Epping, M. I. Pech-Canul, M. F. Bekheet, and A. Gurlo: ‘Macroporous polymer-derived SiO₂/SiOC monoliths freeze-cast from polysiloxane and amorphous silica derived from rice husk’, *Journal of the European Ceramic Society*, 2017, **37**(15), 4809–4820, doi: 10.1016/j.jeurceramsoc.2017.06.023.
99. H. Zhang, P. D’Angelo Nunes, M. Wilhelm, and K. Rezwan: ‘Hierarchically ordered micro/meso/macroporous polymer-derived ceramic monoliths fabricated by freeze-casting’, *Journal of the European Ceramic Society*, 2016, **36**(1), 51–58, doi: 10.1016/j.jeurceramsoc.2015.09.018.
100. H. Zhang, C. L. Fidelis, A. L. T. Serva, M. Wilhelm, and K. Rezwan: ‘Water - based freeze casting: Adjusting hydrophobic polymethylsiloxane for obtaining hierarchically ordered porous SiOC’ , *Journal of the American Ceramic Society*, 2017, **100**, 1907–1918, doi: 10.1111/jace.14782.
101. R. Obmann, S. Schörpf, C. Gorsche, R. Liska, T. Fey, and T. Konegger: ‘Porous polysilazane-derived ceramic structures generated through photopolymerization-assisted solidification templating’, *Journal of the European Ceramic Society*, 2019, **39**(4), 838–845, doi: 10.1016/j.jeurceramsoc.2018.11.045.
102. D. C. Marcano, D. V. Kosynkin, J. M. Berlin, A. Sinitskii, Z. Sun, A. Slesarev, L. B. Alemany, W. Lu, and J. M. Tour: ‘Improved synthesis of graphene oxide’, *ACS nano*, 2010, **4**(8), 4806–4814, doi: 10.1021/nn1006368.

7. References

103. F. García Moreno, M. Fromme, and J. Banhart: ‘Real-time X-ray Radioscopy on Metallic Foams Using a Compact Micro-Focus Source’, *Adv. Eng. Mater.*, 2004, **6**(6), 416–420, doi: 10.1002/adem.200405143.
104. S. Brunauer, P. H. Emmett, and E. Teller: ‘Adsorption of Gases in Multimolecular Layers’, *Journal of the American Chemical Society*, 1938, **60**(2), 309–319, doi: 10.1021/ja01269a023.
105. C. E. Hoyle, T. Y. Lee, and T. Roper: ‘Thiol-enes: Chemistry of the past with promise for the future’, *Journal of Polymer Science Part A: Polymer Chemistry*, 2004, **42**(21), 5301–5338, doi: 10.1002/pola.20366.
106. B. H. Northrop and R. N. Coffey: ‘Thiol-ene click chemistry: computational and kinetic analysis of the influence of alkene functionality’, *Journal of the American Chemical Society*, 2012, **134**(33), 13804–13817, doi: 10.1021/ja305441d.
107. J. Cordelair and P. Greil: ‘Electrical conductivity measurements as a microprobe for structure transitions in polysiloxane derived Si–O–C ceramics’, *Journal of the European Ceramic Society*, 2000, **20**(12), 1947–1957, doi: 10.1016/S0955-2219(00)00068-6.
108. A. Ovsianikov, J. Viertl, B. Chichkov, M. Oubaha, B. MacCraith, I. Sakellari, A. Giakoumaki, D. Gray, M. Vamvakaki, M. Farsari, and C. Fotakis: ‘Ultra-low shrinkage hybrid photosensitive material for two-photon polymerization microfabrication’, *ACS nano*, 2008, **2**(11), 2257–2262, doi: 10.1021/nn800451w.
109. A. Vyatskikh, S. Delalande, A. Kudo, X. Zhang, C. M. Portela, and J. R. Greer: ‘Additive manufacturing of 3D nano-architected metals’, *Nature communications*, 2018, **9**(1), 593, doi: 10.1038/s41467-018-03071-9.
110. X. Zheng, H. Lee, T. H. Weisgraber, M. Shusteff, J. DeOtte, E. B. Duoss, J. D. Kuntz, M. M. Biener, Q. Ge, J. A. Jackson, S. O. Kucheyev, N. X. Fang, and C. M. Spadaccini: ‘Ultralight, ultrastiff mechanical metamaterials’, *Science*, 2014, **344**(6190), 1373–1377, doi: 10.1126/science.1252291.

111. F. Liravi, S. Das, and C. Zhou: ‘Separation force analysis and prediction based on cohesive element model for constrained-surface Stereolithography processes’, *Computer-Aided Design*, 2015, **69**, 134–142, doi: 10.1016/j.cad.2015.05.002.
112. I. Kovalenko, M. Garan, A. Shynkarenko, P. Zelený, and J. Šafka: ‘Examining the relationship between forces during stereolithography 3D printing and geometric parameters of the model’, *MATEC Web of Conferences*, 2016, **40**, 2005.
113. N. B. Cramer, C. L. Couch, K. M. Schreck, J. A. Carioscia, J. E. Boulden, J. W. Stansbury, and C. N. Bowman: ‘Investigation of thiol-ene and thiol-ene-methacrylate based resins as dental restorative materials’, *Dental materials : official publication of the Academy of Dental Materials*, 2010, **26**(1), 21–28, doi: 10.1016/j.dental.2009.08.004.
114. S. Beigi, H. Yeganeh, and M. Atai: ‘Evaluation of fracture toughness and mechanical properties of ternary thiol-ene-methacrylate systems as resin matrix for dental restorative composites’, *Dental materials : official publication of the Academy of Dental Materials*, 2013, **29**(7), 777–787, doi: 10.1016/j.dental.2013.04.015.
115. hlocke: ‘The best of both worlds: Flexvat with raised edge vented acrylic FEP support plate: PDMS vs FEP Based 3D Printer Resin Vats’, 2017; available at <http://projectsinterestsandetcetera.com/the-best-of-both-worlds-flexvat-with-raised-edge-vented-acrylic-fep-support-plate/> (accessed 16 January 2019).
116. N. B. Cramer and C. N. Bowman: ‘Kinetics of thiol - ene and thiol - acrylate photopolymerizations with real - time fourier transform infrared’ , *Journal of Polymer Science Part A: Polymer Chemistry*, 2001, **39**(19), 3311–3319, doi: 10.1002/pola.1314.
117. H. Q. Ly, R. Taylor, R. J. Day, and F. Heatley: ‘Conversion of polycarbosilane (PCS) to SiC-based ceramic Part 1. Characterisation of PCS and curing products: Journal of

7. References

- Materials Science', *Journal of Materials Science*, 2001, **36**(16), 4037–4043, doi: 10.1023/A:1017942826657.
118. E. Ionescu: 'Polymer-Derived Ceramics', in 'Ceramics science and technology', (ed. R. Riedel and I.-W. Chen), 457–500; 2012, Hoboken, NJ, Weinheim, Wiley; Wiley-VCH.
119. R. Raj, L. Pederiva, M. NarisawaL, and G. D. Soraru: 'On the Onset of Fracture as a Silicon - Based Polymer Converts into the Ceramic Phase', *Journal of the American Ceramic Society*, 2018, **102**(3), 924–929, doi: 10.1111/jace.16089.
120. K. Tangermann-Gerk, G. Barroso, B. Weisenseel, P. Greil, T. Fey, M. Schmidt, and G. Motz: 'Laser pyrolysis of an organosilazane-based glass/ZrO₂ composite coating system', *Materials & Design*, 2016, **109**, 644–651, doi: 10.1016/j.matdes.2016.07.102.
121. G. Mera, A. Navrotsky, S. Sen, H.-J. Kleebe, and R. Riedel: 'Polymer -derived SiCN and SiOC ceramics – structure and energetics at the nanoscale', *Journal of Materials Chemistry A*, 2013, **1**(12), 3826–3836, doi: 10.1039/C2TA00727D.
122. S. Martínez-Crespiera, E. Ionescu, H.-J. Kleebe, and R. Riedel: 'Pressureless synthesis of fully dense and crack-free SiOC bulk ceramics via photo-crosslinking and pyrolysis of a polysiloxane', *Journal of the European Ceramic Society*, 2011, **31**(5), 913–919, doi: 10.1016/j.jeurceramsoc.2010.11.019.
123. J. V. Ryan, P. Colombo, J. A. Howell, and C. G. Pantano: 'Tribology-Structure Relationships in Silicon Oxycarbide Thin Films', *International Journal of Applied Ceramic Technology*, 2010, **7**(5), 675–686, doi: 10.1111/j.1744-7402.2009.02374.x.
124. M. A. El Khakani, M. Chaker, A. Jean, S. Boily, J. C. Kieffer, M. E. O'Hern, M. F. Ravet, and F. Rousseaux: 'Hardness and Young's modulus of amorphous a-SiC thin films determined by nanoindentation and bulge tests', *J. Mater. Res.*, 1994, **9**(01), 96–103, doi: 10.1557/JMR.1994.0096.

125. G. M. Renlund, S. Prochazka, and R. H. Doremus: ‘Silicon oxycarbide glasses: Part I. Preparation and chemistry’, *J. Mater. Res.*, 1991, **6**(12), 2716–2722, doi: 10.1557/JMR.1991.2716.
126. L. J. Gibson and M. F. Ashby: ‘Cellular Solids: Structure and Properties’, 2014/08, Cambridge University Press, doi: 10.1017/CBO9781139878326.
127. J. Zhang and M. F. Ashby: ‘The out-of-plane properties of honeycombs’, *International Journal of Mechanical Sciences*, 1992, **34**(6), 475–489, doi: 10.1016/0020-7403(92)90013-7.
128. G. Liu, Y. Zhao, G. Wu, and J. Lu: ‘Origami and 4D printing of elastomer-derived ceramic structures’, *Science Advances*, 2018, **4**(8), eaat0641, doi: 10.1126/sciadv.aat0641.
129. P. Ramavath, P. Biswas, N. Ravi, and R. Johnson: ‘Prediction and validation of buckling stress (σ_{crit}) of the ceramic honeycomb cell walls under quasi-static compression’, *Cogent Engineering*, 2016, **3**(1), 474, doi: 10.1080/23311916.2016.1168068.
130. R. K. Bird and T. S. Lapointe: ‘Evaluation of Ceramic Honeycomb Core Compression Behavior at Room Temperature’.
131. J. T. Muth, P. G. Dixon, L. Woish, L. J. Gibson, and J. A. Lewis: ‘Architected cellular ceramics with tailored stiffness via direct foam writing’, *Proc Natl Acad Sci USA*, 2017, **114**(8), 1832–1837, doi: 10.1073/pnas.1616769114.
132. C. Agrafiotis, I. Mavroidis, A. Konstandopoulos, B. Hoffschmidt, P. Stobbe, M. Romero, and V. Fernandezquero: ‘Evaluation of porous silicon carbide monolithic honeycombs as volumetric receivers/collectors of concentrated solar radiation’, *Solar Energy Materials and Solar Cells*, 2007, **91**(6), 474–488, doi: 10.1016/j.solmat.2006.10.021.
133. N. A. Fleck, V. S. Deshpande, and M. F. Ashby: ‘Micro-architected materials: past, present and future’, *Proceedings of the Royal Society A: Mathematical, Physical and Engineering Sciences*, 2010, **466**(2121), 2495–2516, doi: 10.1098/rspa.2010.0215.

7. References

134. H. Awaji, T. Watanabe, and Y. Nagano: ‘Compressive testing of ceramics’, *Ceramics International*, 1994, **20**(3), 159–167, doi: 10.1016/0272-8842(94)90034-5.
135. Nicoguardo: ‘Material-comparison--strength-vs-density plain’, 2015; available at https://commons.wikimedia.org/wiki/File:Material-comparison--strength-vs-density_plain.svg (accessed 16 January 2019).
136. R. Liu, J. Yuan, and C.-A. Wang: ‘A novel way to fabricate tubular porous mullite membrane supports by TBA-based freezing casting method’, *Journal of the European Ceramic Society*, 2013, **33**(15-16), 3249–3256, doi: 10.1016/j.jeurceramsoc.2013.06.005.
137. H. J. Choi, T. Y. Yang, S. Y. Yoon, B. K. Kim, and H. C. Park: ‘Porous alumina/zirconia layered composites with unidirectional pore channels processed using a tertiary-butyl alcohol-based freeze casting’, *Materials Chemistry and Physics*, 2012, **133**(1), 16–20, doi: 10.1016/j.matchemphys.2011.12.055.
138. X. Wang, G. Mera, K. Morita, and E. Ionescu: ‘Synthesis of polymer-derived graphene/silicon nitride-based nanocomposites with tunable dielectric properties’, *J. Ceram. Soc. Japan*, 2016, **124**(10), 981–988, doi: 10.2109/jcersj2.16089.
139. R. Chen, C.-A. Wang, Y. Huang, L. Ma, and W. Lin: ‘Ceramics with Special Porous Structures Fabricated by Freeze-Gelcasting: Using tert-Butyl Alcohol as a Template’, *J American Ceramic Society*, 2007, **90**(11), 3478–3484, doi: 10.1111/j.1551-2916.2007.01957.x.
140. E. Brener, H. Müller-Krumbhaar, and D. Temkin: ‘Structure formation and the morphology diagram of possible structures in two-dimensional diffusional growth’, *Phys. Rev. E*, 1996, **54**(3), 2714–2722, doi: 10.1103/PhysRevE.54.2714.
141. C. Vakifahmetoglu, D. Zeydanli, V. C. Ozalp, B. A. Borsa, and G. D. Soraru: ‘Hierarchically porous polymer derived ceramics: A promising platform for multidrug delivery systems’, *Materials & Design*, 2018, **140**, 37–44, doi: 10.1016/j.matdes.2017.11.047.

142. K. Lu: 'Porous and high surface area silicon oxycarbide-based materials—A review', *Materials Science and Engineering: R: Reports*, 2015, **97**, 23–49, doi: 10.1016/j.mser.2015.09.001.
143. L. Biasetto, R. Peña-Alonso, G. D. Sorarù, and P. Colombo: 'Etching of SiOC ceramic foams', *Advances in Applied Ceramics*, 2008, **107**(2), 106–110, doi: 10.1179/174367607X227963.
144. R. Pena-Alonso, G. D. Soraru, and R. Raj: 'Preparation of Ultrathin-Walled Carbon-Based Nanoporous Structures by Etching Pseudo-Amorphous Silicon Oxycarbide Ceramics', *J American Ceramic Society*, 2006, **89**(8), 2473–2480, doi: 10.1111/j.1551-2916.2006.01117.x.

Symbols and abbreviations

Abbreviation	Definition
3DP	3D Printing
AM	Additive Manufacturing
ATR	Attenuated Total Reflection
BET	Brunauer-Emmett-Teller
CAD	Computer-Aided Design
DSC	Differential Scanning Calorimetry
DLP	Digital Light Processing
DMD	Digital Micro-Mirror Device
DIW	Direct Ink Writing
DIP	Direct Inkjet Printing
EBAM	Electron Beam Additive Manufacturing
EBM	Electron Beam Melting
EDX	Energy-Dispersive X-ray Spectroscopy
FE-EMPA	Field Emission-Electron Probe Microanalysis
FTIR	Fourier-Transform Infrared Spectroscopy
FDM	Fused Deposition Modeling
LOM	Laminated Object Manufacturing
LCM	Lithography-based Ceramic Manufacturing
MS	Mass Spectrometry
MJ	Material Jetting
MEMS	Micro-Electro-Mechanical Systems
NMR	Nuclear Magnetic Resonance
PI	Photoinitiators
PA	Photoabsorbers
PDCs	Polymer-Derived Ceramics
PCPs	Preceramic Polymers
RI	Refractive Index

SEM	Scanning Electron Microscopy
SLM	Selective Laser Melting
SLS	Selective Laser Sintering
STA	Simultaneous Thermal Analysis
S-3DP	Slurry based 3DP
S-SLS	Slurry based SLS
SSA	Specific Surface Area
3D	Three-Dimensional
TEM	Transmission Electron Microscopy
2D	Two-Dimensional
UV-Vis	Ultraviolet–Visible
XRD	X-Ray Diffraction
XPS	X-Ray Photoelectron Spectroscopy

List of figures

Figure 1. Simplified representation of organosilicon compounds as precursors for Si based ceramics ¹⁵	3
Figure 2. Hydrosilylation reaction between Si-H and Si-vinyl groups.	5
Figure 3. Printed and sintered SiO ₂ glass structure (pretzel) with high optical transparency manufactured by SLA ⁸⁰ . Reprinted by permission from F. Kotz et al.: ‘Three-dimensional printing of transparent fused silica glass’, <i>Nature</i> , 2017, 544(7650), 337-339. Copyright 2017 Springer Nature.	20
Figure. 4 Viscosity of hydroxyapatite filled photopolymer resin with different solid loading and diluent ⁸²	22
Figure 5. Measured curing depth (C _d) of 50 vol % suspension of SiO ₂ powder (d ₅₀ = 4.64 μm) in acrylamide solutions with respect to the refractive index contrast using a 365 nm collimated light source ^{84,85} . Reprinted by permission from J. W. Halloran: ‘Ceramic Stereolithography: Additive Manufacturing for Ceramics by Photopolymerization’, Annual review of materials research, 2016, 46(1), 19-40. Copyright 2001 Annual Reviews, Inc.	23
Figure 6. Shape of the curing profile in SiO ₂ suspension with photopolymer varying its refractive index. Significant broadening of curing width is observed in the case of high energy exposure and in the resin with high RI contrast ⁸⁵ . Reprinted by permission from J. W. Halloran: ‘Ceramic Stereolithography: Additive Manufacturing for Ceramics by Photopolymerization’, Annual review of materials research, 2016, 46(1), 19-40. Copyright 2001 Annual Reviews, Inc.	24
Figure 7. Fundamental processing steps of freeze casting technique. Each processing steps is explained in detail in the text. The figure is redraw from ⁸⁷	30
Figure 8. SEM images of porous PDCs produced by freeze casting PMS using different solvents, which determines the pore morphology (a) cyclohexane (b) camphene (c) TBA ⁹⁶ . Reprinted by permission from M. Naviroj et al.: ‘Directionally aligned macroporous SiOC via freeze casting of preceramic polymers’, Journal of the European Ceramic Society, 2015, 35(8), 2225-2232. Copyright 2015 Elsevier.	35

Figure 9. General processing routes applied in this thesis, including photocuring experiments (chapter 3), stereolithography (chapter 4) and freeze casting (chapter 5).....	45
Figure 10. UV-Vis absorption spectra of H62C (black), H62C blended with DMPA (blue) and H62C mixed with BAPO (red).....	54
Figure 11. Structural formulae of Durazane 1800 and SMP10.....	56
Figure 12. ATR-FTIR spectra of polysiloxanes H62C and SPR212, polycarbosilane SMP10 and polycarbosilazane Durazane 1800 employed in this work. Absorption bands, which determine the class of preceramic polymers, are marked as red, while the alkene side groups are marked in blue.	57
Figure 13. ATR-FTIR spectra of preceramic resins before curing (black) and after curing (red): (A) polysiloxane H62C, (B) polysiloxane SPR212, (C) polycarbosilane SMP10 and (D) polycarbosilazane Dura18. The thiol-ene click polymerization is confirmed by the strong reduction of the absorption bands of the vinyl groups that are displayed in the inset.....	58
Figure 14. UV-vis absorption spectrum of SMP10 displaying the absorption starting below 550 nm. Inset shows the optical images of employed preceramic polymers.....	59
Figure 15. High penetration depth of incident light in H62C, SPR212 and Dura18-2T resins allows for the fabrication of bulk thermoset specimens with thickness of about 10 mm while SMP10-2T resin demonstrates significantly reduced curing depth due to its intrinsic yellowish color.....	60
Figure 16. Gel formation in SPR212, Dura1800 and H62C resins dissolved in different organic solvents (from left to right, acetone, tert-butanol, tetrahydrofuran and cyclohexane) with a weight ratio of 1:2 (PCPs to solvents).....	62
Figure 17. (a) Results of the in-situ differential scanning calorimetric characterization (UV-DSC) of preceramic resins with dithiol. (b) Magnified UV-DSC plots demonstrate the lower reaction rate of SMP10 than other preceramic polymers (SPR212, H62C and Dura1800).....	63
Figure 18. The conversion of thiol-ene click reaction of preceramic polymers with dithiol obtained by integration of the heat flow curves and subsequent normalization.....	66

Figure 19. Results of the in-situ differential scanning calorimetric characterization (UV-DSC) of H62C-4T and H62C-2T resins, demonstrate the significantly reduced heat flow maximum due to tetrathiol.	67
Figure 20. Schematic of the simplified thiol-ene click chemistry approach towards polymer-derived ceramics based on photoinduced cross-linking of vinyl-containing Si-based preceramic polymers with 1,6-hexanedihol via an anti-Markovnikov addition followed by the pyrolysis at 1100 °C in N ₂ /Ar. Reprinted by permission from X. Wang et al.: ‘Additive manufacturing of ceramics from preceramic polymers: A versatile stereolithographic approach assisted by thiol-ene click chemistry’, <i>Additive Manufacturing</i> , 2019, 27, 80-90. Copyright 2019 Elsevier.	72
Figure 21. Additive manufacturing of ceramics from preceramic polymers: schematic representation of thiol-ene click chemistry-based stereolithography. (A) The preceramic photopolymerizable (B) Photopolymerization of preceramic resins in a benchtop DLP (C) Ceramic part after pyrolysis. Reprinted by permission from X. Wang et al.: ‘Additive manufacturing of ceramics from preceramic polymers: A versatile stereolithographic approach assisted by thiol-ene click chemistry’, <i>Additive Manufacturing</i> , 2019, 27, 80-90. Copyright 2019 Elsevier.	72
Figure 22. Set up of the LittleRP2 DLP 3D printer with mounted projector, which is modified to allow short distance focusing.	76
Figure 23. Printing failures of a preceramic polymer resin in the Form 2 SLA printer due to unsuccessful release of printed parts from the bottom of the resin tank.	78
Figure 24. FEP Teflon film based 3D Printer Resin Vat with Raised Edge Vented Support Plate ¹¹⁵	79
Figure 25. 3D-printed SPR212 cylinder utilizing the FEP film-based VAT design. The significant observed over-curing is due to the absence of photoabsorbers in the resin.	79
Figure 26. Dynamic viscosity of intrinsic preceramic polymers utilized in this thesis.	81
Figure 27. Set up to determine the photoinitiator contents.	85

Figure 28. Results of photopolymerization tests for determining the optimal amount of photoinitiator for SPR212.	85
Figure 29. Set up for the curing depth measurements.	87
Figure 30. Measured curing depth versus exposure time for preceramic polymer-2T resins mixed with different amounts of photoinitiator BAPO and photoabsorber Sudan Orange G.	90
Figure 31. Calculated attenuation length D_p of preceramic polymer-2T resins compared to the attenuation length of hexanediol diacrylate (HDDA) filled with ceramic particles, PI represents photoinitiator, PA represents photoabsorber. The data for SiO_2 in HDDA is taken from ⁸⁵ , while the data for Al_2O_3 in HDDA is taken from ⁸⁴	91
Figure 32. Representative examples of thermoset parts fabricated from three different polymer classes: (A) Kelvin cell structure printed with polysiloxane SPR212, (B) cog wheel printed with polycarbosilane SMP10 and (C) turbine structure printed with polycarbosilane Durazane1800. Reprinted by permission from X. Wang et al.: ‘Additive manufacturing of ceramics from preceramic polymers: A versatile stereolithographic approach assisted by thiol-ene click chemistry’, <i>Additive Manufacturing</i> , 2019, 27, 80-90. Copyright 2019 Elsevier.	94
Figure 33. A representative printed cross-linked thermoset of SPR212 and the resultant glassy ceramic formed upon pyrolysis at 1100 °C under N_2 atmosphere, demonstrating a roughly 30 % linear shrinkage. Reprinted by permission from X. Wang et al.: ‘Additive manufacturing of ceramics from preceramic polymers: A versatile stereolithographic approach assisted by thiol-ene click chemistry’, <i>Additive Manufacturing</i> , 2019, 27, 80-90. Copyright 2019 Elsevier.	96
Figure 34. Examples of ceramic components free from macrosized voids and defects fabricated by pyrolyzing the cross-linked thermosets (shown in Fig. 4): (A-D) Images of components and (E-H) the corresponding radiography images of the (A,E) SiOC Kelvin cell structure; (B,F) SiOC turbine impeller; (C,G) SiCN(O) cog wheel and (D,H) SiCN(O) turbine. Reprinted by permission from X. Wang et al.: ‘Additive manufacturing of ceramics from preceramic polymers: A versatile stereolithographic approach assisted by thiol-ene click chemistry’, <i>Additive Manufacturing</i> , 2019, 27, 80-90. Copyright 2019 Elsevier.	98

Figure 35. STA characterization of the polymer-to-ceramic transformation of the cross-linked thermosets fabricated from SPR212, SMP10 and Durazane 1800: (A) selected MS data for SPR212 indicating the release of SO_2 ($m/z= 64$), CH_3SH ($m/z= 48$), C_4H_8 ($m/z= 56$) and H_2S ($m/z= 34$) due to the decomposition of thioether linkages during the major mass loss region and (B) TG curves indicating the overall weight loss. Reprinted by permission from X. Wang et al.: ‘Additive manufacturing of ceramics from preceramic polymers: A versatile stereolithographic approach assisted by thiol-ene click chemistry’, *Additive Manufacturing*, 2019, 27, 80-90. Copyright 2019 Elsevier. 99

Figure 36. Characterization of additively-manufactured polymer-derived ceramic materials: (A) ATR-FTIR data; (B) X-ray photoelectron spectra of SiOC (red), SiC(O) (green) and SiCN(O) (blue) synthesized at 1100°C from SPR212, SMP10 and Durazane 1800, respectively. Analysis of SPR212-derived SiOC ceramic pyrolyzed at 1100 °C; (C) TEM image, with selected area electron diffraction (SAED) pattern shown in inset indicating a homogeneous amorphous structure; (D) solid state ^{29}Si NMR spectra, revealing mixed bonding between Si, O and C. Reprinted by permission from X. Wang et al.: ‘Additive manufacturing of ceramics from preceramic polymers: A versatile stereolithographic approach assisted by thiol-ene click chemistry’, *Additive Manufacturing*, 2019, 27, 80-90. Copyright 2019 Elsevier. 101

Figure 37. Morphology and microstructure of additively manufactured SPR212-derived SiOC: (A and E) tomographic images of the diamond lattice (A) and Kelvin cell (E) structures. The delicate design is perfectly replicated without any detectable flaws. (B-D, F-H) corresponding SEM images at higher magnification showing the step-like surfaces as well as the crack-free struts. Reprinted by permission from X. Wang et al.: ‘Additive manufacturing of ceramics from preceramic polymers: A versatile stereolithographic approach assisted by thiol-ene click chemistry’, *Additive Manufacturing*, 2019, 27, 80-90. Copyright 2019 Elsevier. 103

Figure 38. Results of nanoindentation tests performed on 2D honeycombs of additively-manufactured SPR212-derived SiOC. (A) A polished SiOC honeycomb imbedded in epoxy resin. Inset shows the AFM image of one indent. (B) Load-Hold-Unload curve of one indent. Elastic modulus is determined via the elastic unloading process. (C, D)

Reduced modulus and hardness as a function of the penetration depth. 200 measurement results are shown here. Reprinted by permission from X. Wang et al.: ‘Additive manufacturing of ceramics from preceramic polymers: A versatile stereolithographic approach assisted by thiol-ene click chemistry’, *Additive Manufacturing*, 2019, 27, 80-90. Copyright 2019 Elsevier.104

Figure 39. Left: Schematic representation of 2D honeycomb with a cellular density of 0.61 g/cm³ of additively-manufactured SPR212-derived SiOC carrying loads on the faces normal to X3. Right: Measured stress-strain curves of fabricated SiOC honeycombs. Symbol “*” represents the first major failure of ceramic honeycomb. Reprinted by permission from X. Wang et al.: ‘Additive manufacturing of ceramics from preceramic polymers: A versatile stereolithographic approach assisted by thiol-ene click chemistry’, *Additive Manufacturing*, 2019, 27, 80-90. Copyright 2019 Elsevier.106

Figure 40. Image of the metal face sheet showcased apparent hexagonal scratches and ceramic residual after compression test due to the imprinting of SiOC ceramic into steel.....108

Figure 41. Strength-density Ashby chart for designing light strong structures. In this chart, our additively-manufactured SiOC honeycombs are compared to other ceramic (i.e. SiOC, Al₂O₃, SiC) honeycombs as well as to other natural and technical materials. Figure and material properties are generated by Nicoguardo using JavaScript and D3.js¹³⁵, except the data points of different ceramic honeycombs, which were inserted manually from the corresponding references. Reprinted by permission from X. Wang et al.: ‘Additive manufacturing of ceramics from preceramic polymers: A versatile stereolithographic approach assisted by thiol-ene click chemistry’, *Additive Manufacturing*, 2019, 27, 80-90. Copyright 2019 Elsevier.110

Figure 42. Schematic of cryo thiol-ene click chemistry assisted freeze casting of preceramic polymers.114

Figure 43. Self-made freeze casting set up with (a) controlled freeze rate and (b) rapid freezing.117

Figure 44. Optical images of a) H62C/DMPA/TBA (HG0) solution and b) H62C/GO/DMPA/TBA (HG2) suspension with corresponding UV-Vis absorption spectra shown in c).....	119
Figure 45. Optical image demonstrating cryo photopolymerizaion of frozen HG0 (white) and HG2 (black) samples.....	120
Figure 46. Left: FTIR spectra of (a) liquid polysiloxane H62C, (b) freeze cast H62C monolith after cryo UV polymerization and vacuum drying and (c) H62C-derived SiOC after pyrolysis under N ₂ atmosphere. The decreasing intensity of Si-vinyl absorption bands is shown in inset. Right: Optical image of freeze cast H62C foam (white) and H62C/GO foam (brown) after freeze drying.....	121
Figure 47. Optical (left) and SEM (middle and right) images of (a) SiOC monoliths (sample HG0 and (b, c) SiOC/GO shells (samples HG1 and HG2) displaying aligned pores in the specimens.....	124
Figure 48. X-Ray Computed Tomography (μ CT) images demonstrate the two-phase composition of HG2 samples.	124
Figure 49. (A-D) SEM images in BSE mode of the sample HG2. (E-H) FE-EMPA spectral maps of the Si, O, C and S from the part shown in D (which are slightly rotated clockwise).	125
Figure 50. TEM (a-d) images in the dark-field (b) and bright-filed (c, d) mode and selected area electron diffraction patterns shown as insets in c and.....	127
Figure 51. XRD diffraction patterns of HG0, HG1 and HG2 samples. The inset displays a tiny reflection in HG2 attributed to the graphite (002) (PDF 041-1487).....	128
Figure 52. The microstructure samples without (HG0) and with GO (HG2) after each processing step documented by radiography images. The images in (d) are a cross-sectional view of samples in (c).....	130
Figure 53. In situ radiography images captured during the vacuum drying of frozen samples with (HG2) and without GO (HG0). Red arrows indicate the interface where the cross-linking of the polysiloxane H62C is insufficient.	131

Figure 54. (a) Two dimensional schematic illustration of GO containing samples after each freeze casting step. Red and worm-like polymer chain represents the original preceramic polymer, while solid red areas represent the cross-linked interconnected region. TBA crystals are shown as prisms in green. (b) FTIR spectra of the internal (a) and external (b) segments of the freeze cast and dried HG2 samples, while the internal part still exhibits clear Si-vinyl absorption band.	133
Figure 55. Optical image of freeze cast specimens derived from H62C dissolved in a 10 mg/ml GO/TBA suspension confirming that the cross-linking is solely restricted to the external part of the sample.	134
Figure 56. Optical images of (a) freeze dried and (b) pyrolyzed specimens demonstrating almost perfect cylindrical form. In (b) different shrinkage degree is observed while the cylinder geometry was not distorted during the pyrolysis.	138
Figure 57. SEM micrographs of ceramic foams derived from TBA30 and TBA20 samples. These images are taken from cross-sections perpendicular to the freezing direction, at distances of 2 mm (left images) and 8 mm (right images) away from the bottom of the sample.	141
Figure 58. The transparent polymer solution allows the clear observation of the solidification process, here shown exemplarily for sample TBA30.	142
Figure 59. SEM micrographs of ceramic foams derived from Cam30 specimen. These images are taken from cross-sections perpendicular to the freezing direction, at distances of 2 mm (left images) and 6 mm (right images) away from the bottom of the sample.	144
Figure 60. SEM micrographs of TBA30-15 and 40 derived ceramic foams with SiO ₂ filler. The images are taken from cross-sections perpendicular to the freezing direction, 2 and 8 mm away from the bottom of the sample.	145
Figure 61. (a) Nitrogen adsorption-desorption isotherms and (b) pore size distribution in micro- and mesopore range for the TBA30-derived samples. For details see Table 23.	147
Figure 62. (a) HR-TEM image and (b) EDX spectrum of TBA-30 derived SiOC sample etched with HF for 72 hours. Inset in (a) shows the selected	

area electron diffraction (SAED) pattern. Insets in (b) are the TEM images and corresponding element distribution of C, Si and O. 149

Figure 63. (a) Nitrogen adsorption-desorption isotherm and (b) pore size distribution in micro- and mesopore range for the TBA30-40 derived samples with SiO₂ filler. For details see Table 23. 150

Figure 64. TEM images of HF-etched TBA30 (a) and TBA30-40 derived ceramic foams. The latter demonstrates the hierarchical porosity. 150

List of tables

Table 1. AM process categories and representative examples according to the ISO/ASTM 52900 ⁵²	10
Table 2. Material choice for AM technologies.	13
Table 3. Main strategies used for the stereolithography of polymer derived ceramics.	26
Table 4. Overview of freeze cast polymer-derived ceramics.	38
Table 5. Materials applied in this work.	40
Table 6 Specifications of silica powders.	41
Table 7. Formulations overview of preceramic polymer based resins. For the preparation of organogels 1-3, S1 are acetone, TBA, THF and cyclohexane, while S2 are THF, cyclohexane. Numbers in the table represent weight ratios of the components. For example, thermoset 1 resin is prepared by mixing H62C, 2T, DMPA in a weight ratio of 100:10:1.....	46
Table 8. Specifications of UV illuminator.	54
Table 9. Typical vibration frequencies of preceramic polymer utilized in this thesis.	55
Table 10. Photocuring of preceramic polymer-dithiol solutions. Dura1800 was only dissolvable in THF and cyclohexane, because tert-butanol and acetone react with the polysilazane.	61
Table 11. Measured reaction heat and calculated reaction enthalpy and conversion efficiency of thiol-ene click reaction between dithiol and preceramic polymers.	64
Table 12. Viscosity of employed preceramic polymer at shear rate of 25 1/s.....	82
Table 13. The weight ratio of polymer to dithiol calculated according to Equation 4.....	83

Table 14. Resin compositions for the curing depth measurements. Note the weight percent of BAPO and Sudan G is an approximation, for exact compositions please see Table 7.....	86
Table 15. Resin formulations for the application in LittleRP2 DLP printer.	92
Table 16. Printing parameters set by creation workshop.	93
Table 17. Elemental composition of ceramics pyrolyzed at 1100 °C in flowing nitrogen.....	100
Table 18. Detailed information of honeycombs utilized for compression tests and the obtained compressive strength and cell modulus of SiOC honeycombs.	106
Table 19. Compositions applied for freeze casting.	118
Table 20. Chemical composition of the HG2 sample analyzed by FE-EMPA. Positions numbered from 1 to 6 are selected uniformly at low resolution throughout the whole sample at macroscale, whereas position No. 7 corresponds to local inhomogeneity seen as dark areas in Figure 49 C, D.....	126
Table 21. Composition of samples studied in this chapter.....	137
Table 22. Characteristics of freeze cast, vacuum dried and pyrolyzed specimens studied in this chapter.	139
Table 23. Specific surface area and micro- and mesopore volume for HF-etched samples studied in this work.....	148

Schriftenreihe **Advanced Ceramic Materials**

Hrsg.: Prof. Dr. Aleksander Gurlo

ISSN 2569-8303 (print)

ISSN 2569-8338 (online)

1: Colmenares, Maria: Ordered mesoporous silica COK-12: mesoscale tailoring, upscaling, continuous synthesis and application in the oxidative coupling of methane. - 2018. - xx, 180 S.

ISBN **978-3-7983-2988-1** (print) EUR **12,00**

ISBN **978-3-7983-2989-8** (online)

DOI 10.14279/depositonce-6744

2: van Duren, Stephan: Development of in situ methods for process monitoring and control and characterization of Cu-Zn-Sn-S based thin films. - 2019. - xix, 183 S.

ISBN **978-3-7983-3064-1** (print) EUR **12,00**

ISBN **978-3-7983-3065-8** (online)

DOI 10.14279/depositonce-7732



Photoinduced Thiol-Ene Click Chemistry Assisted Additive Manufacturing and Freeze Casting of Polymer-Derived Ceramics

Polymer-derived ceramics possess great advantages in the view of cellular ceramic processing compared to traditional powder-based technologies, as the polymeric nature of ceramic precursors allows the utilization of various shaping approaches. Amongst them, Additive Manufacturing and Freeze Casting are two novel shaping methods, which are capable of producing three-dimensional complex architectures and foams with well-controlled pore morphology, respectively.

In this thesis, photoinduced thiol-ene polymerization of vinyl containing preceramic polymers with thiol monomers is systematically investigated, both from the energetic view and from the kinetic view. Subsequently, a novel stereolithographic approach is developed and applied to the additive manufacturing of complex-shaped polymer-derived ceramics. In addition, photo-polymerization-assisted freeze casting is successfully developed to freeze cast liquid preceramic polymer and yields porous ceramics with well-controlled pore morphology.

ISBN 978-3-7983-3088-7 (print)

ISBN 978-3-7983-3089-4 (online)



ISBN 978-3-7983-3088-7



<http://verlag.tu-berlin.de>